

# Strain gradient crystal plasticity based on dislocation densities

**Citation for published version (APA):**

Evers, L. P. (2003). *Strain gradient crystal plasticity based on dislocation densities*. [Phd Thesis 1 (Research TU/e / Graduation TU/e), Mechanical Engineering]. Technische Universiteit Eindhoven.  
<https://doi.org/10.6100/IR567950>

**DOI:**

[10.6100/IR567950](https://doi.org/10.6100/IR567950)

**Document status and date:**

Published: 01/01/2003

**Document Version:**

Publisher's PDF, also known as Version of Record (includes final page, issue and volume numbers)

**Please check the document version of this publication:**

- A submitted manuscript is the version of the article upon submission and before peer-review. There can be important differences between the submitted version and the official published version of record. People interested in the research are advised to contact the author for the final version of the publication, or visit the DOI to the publisher's website.
- The final author version and the galley proof are versions of the publication after peer review.
- The final published version features the final layout of the paper including the volume, issue and page numbers.

[Link to publication](#)

**General rights**

Copyright and moral rights for the publications made accessible in the public portal are retained by the authors and/or other copyright owners and it is a condition of accessing publications that users recognise and abide by the legal requirements associated with these rights.

- Users may download and print one copy of any publication from the public portal for the purpose of private study or research.
- You may not further distribute the material or use it for any profit-making activity or commercial gain
- You may freely distribute the URL identifying the publication in the public portal.

If the publication is distributed under the terms of Article 25fa of the Dutch Copyright Act, indicated by the "Taverne" license above, please follow below link for the End User Agreement:

[www.tue.nl/taverne](http://www.tue.nl/taverne)

**Take down policy**

If you believe that this document breaches copyright please contact us at:

[openaccess@tue.nl](mailto:openaccess@tue.nl)

providing details and we will investigate your claim.

**Strain Gradient Crystal Plasticity  
based on Dislocation Densities**

This research was carried out under project number ME.97028 in the framework of the Strategic Research Programme of the Netherlands Institute for Metals Research (NIMR).

CIP-DATA LIBRARY TECHNISCHE UNIVERSITEIT EINDHOVEN

Evers, Laurens P.

Strain Gradient Crystal Plasticity based on Dislocation Densities / by Laurens P.

Evers. – Eindhoven : Technische Universiteit Eindhoven, 2003

Proefschrift. – ISBN 90-386-2685-1

NUR 929

Trefwoorden: FCC metalen / rekgradiënt / constitutief gedrag / kristalplasticiteit / dislocatiedichtheden / korrelgrenzen / versteviging / lengteschaaleffecten / eindige-elementenmethode / Hall-Petch effect

Subject headings: FCC metals / strain gradient / constitutive behaviour / crystal plasticity / dislocation densities / grain boundaries / strengthening / length scale effects / finite element method / Hall-Petch effect

Copyright ©2003 by L.P. Evers. All rights reserved.

This thesis was prepared with the  $\text{\LaTeX}$  2 $\epsilon$  documentation system.

Reproduction: Universiteitsdrukkerij TU Eindhoven, Eindhoven, The Netherlands.

# Strain Gradient Crystal Plasticity based on Dislocation Densities

PROEFSCHRIFT

ter verkrijging van de graad van doctor  
aan de Technische Universiteit Eindhoven,  
op gezag van de Rector Magnificus, prof.dr. R.A. van Santen,  
voor een commissie aangewezen door het College voor Promoties  
in het openbaar te verdedigen  
op maandag 20 oktober 2003 om 16.00 uur

door

LAURENS PETRONELLA EVERS

geboren te St. Odiliënberg

Dit proefschrift is goedgekeurd door de promotoren:

prof.dr.ir. M.G.D. Geers

en

prof.dr.ir. F.P.T. Baaijens

Copromotor:

dr.ir. W.A.M. Brekelmans

# Contents

---

<b>Summary</b>	<b>vii</b>
<b>Notation</b>	<b>ix</b>
<b>1 Introduction</b>	<b>1</b>
1.1 Physics of crystal plasticity . . . . .	1
1.2 Objective, strategy and outline . . . . .	2
<b>2 Polycrystal model</b>	<b>5</b>
2.1 Introduction . . . . .	5
2.2 Crystal plasticity framework: single crystal approach . . . . .	9
2.2.1 Kinematics . . . . .	9
2.2.2 Constitutive model . . . . .	10
2.2.3 Time integration . . . . .	12
2.3 Intragranular decomposition: bi-crystal approach . . . . .	14
2.3.1 Modified Taylor approach . . . . .	14
2.3.2 Time integration . . . . .	16
2.4 Enhanced hardening . . . . .	16
2.4.1 GND density . . . . .	17
2.5 Numerical results . . . . .	19
2.5.1 Stress-strain behaviour . . . . .	22
2.5.2 Hall-Petch parameters . . . . .	23
2.6 Conclusions . . . . .	25
<b>3 Single crystal model: application to constrained simple shear</b>	<b>27</b>
3.1 Introduction . . . . .	27
3.2 Constitutive framework . . . . .	31
3.2.1 Fundamentals . . . . .	31
3.2.2 Dislocation interactions . . . . .	34
3.2.3 Dislocation density evolutions . . . . .	38

---

3.3	Finite element implementation . . . . .	40
3.4	Application . . . . .	43
3.5	Conclusions . . . . .	48
<b>4</b>	<b>Single crystal model: application to plane stress tension</b>	<b>51</b>
4.1	Introduction . . . . .	51
4.2	Crystal plasticity model . . . . .	54
4.2.1	Constitutive framework . . . . .	54
4.2.2	Dislocation interactions . . . . .	56
4.2.3	Dislocation densities . . . . .	58
4.3	Numerical implementation . . . . .	60
4.3.1	Variational formulation . . . . .	60
4.3.2	Iterative updates and tangents . . . . .	61
4.3.3	Finite element formulation . . . . .	64
4.4	Simulations . . . . .	67
4.5	Conclusions . . . . .	74
<b>5</b>	<b>Discussion and conclusions</b>	<b>77</b>
<b>A</b>	<b>Overview single crystal model</b>	<b>79</b>
	<b>Bibliography</b>	<b>81</b>
	<b>Samenvatting</b>	<b>87</b>
	<b>Dankwoord / Acknowledgements</b>	<b>91</b>
	<b>Curriculum Vitae</b>	<b>93</b>

# Summary

---

The identification of the mechanical behaviour of metals is generally based on presupposed homogeneous deformation and stress fields, while possibly available information with respect to the actual heterogeneous deformation at the scale of the microstructure is hardly used. This severely limits the capability of predicting the constitutive behaviour in the cases that the product dimensions are of the same order as the length scale of the microstructure, i.e. the size of the grains. Correspondingly, scale dependent phenomena such as grain size dependence, or the material's behaviour under an applied heterogeneous load at a global scale, can only be understood, modelled and predicted if the microstructure is considered while the response becomes inherently strain gradient dependent. It is therefore the objective of this research to develop a crystal plasticity formulation that includes these characteristics. Hereby, the bridge from the microstructure and the strain gradients to the mechanical response is the consequence of geometrically necessary dislocations (GND's), which originate from microstructural incompatibilities and cause short- and long-range effects on the constitutive behaviour.

On the polycrystal scale, a crystal plasticity model has been developed, which considers each grain as a single crystal core, surrounded by a collection of bi-crystals representing the grain boundaries. Here, the lattice orientations of the neighbouring grains is incorporated in the outer part of the bi-crystals. The transition of the behaviour of all individual grains (considered in the particular material point) at the microscale to a macroscopic response, is taken into account by an adapted Taylor averaging procedure. When enforcing deformation compatibility and stress equilibrium at the bi-crystal interfaces, the deformation inside the grain becomes heterogeneous (the core and the inner part of the bi-crystals will deform differently), the amount of which depends on the size of the grain. This heterogeneity gives rise to the generation of GND's in order to maintain compatibility of the crystallographic lattice. These GND's act as obstacles to the motion of the gliding dislocations which carry the plastic deformation, also referred to as statistically-stored dislocations (SSD's). An enhanced slip resistance is formulated which incorporates this additional hardening effect. Accordingly, decreasing the grain size increases the flow stress response, a dependence which is also observed experimentally and which is called the



Hall-Petch effect. Simulations under uniaxial loading conditions on a collection of grains with an adaptable grain size result in the numerical prediction of empirically-found grain size dependent stress-strain curves.

With respect to the model above, several restrictions have been introduced, of which some can be overcome at the polycrystal scale, yet others require the consideration of heterogeneities within the grains at a single crystal level. In a finite element context, this involves the subdivision of each grain into sufficient finite elements. Such a framework has been developed next, in which a number of aspects have been improved. First, in the polycrystal approach, the GND densities only follow from plastic deformation incompatibilities in an indirect fashion, whereas in the single crystal framework, a direct geometrical coupling is made between different crystallographic slip gradients and corresponding edge and screw GND densities. Because the determination of all (edge) SSD densities explicitly follows from an appropriate evolution equation, the ambiguous choice of adding the SSD and GND strengths or their effective densities does not have to be made any more. Furthermore, the GND's do not only influence the mechanical response in a short-range sense, i.e. through the local slip resistance, but also the geometrical characteristics of the GND's at a larger length scale are regarded, considering their dislocation sign and the GND density gradients. This long-range influence is included through the consideration of a GND related back-stress contribution, opposite to the resolved shear stress. Besides, at the grain boundaries, more adequate micromechanical constraints (obstruction of crystallographic slip) can be enforced than could previously be prescribed at the bi-crystal interfaces, whereas the additional incorporation of grain boundary dislocation (GBD) densities, accounting for the initial lattice mismatch, provides for a grain size dependent yield point, both in accordance with experimental observations. Finally, a second ambiguous choice, concerning the volume fraction of the bi-crystals with respect to the crystal core, is circumvented using the single crystal approach. The latter approach actually provides the opportunity to assess how that volume fraction should be suitably selected.

The developed crystal plasticity approach has been used to simulate the simple shear behaviour of a fictitious single crystal –having two slip systems– under plane strain conditions. Here, the crystallographic slip in the normal direction is obstructed at the boundary interfaces, initiating a deformation heterogeneity which is related to the strip thickness. A size dependent flow stress is accordingly encountered, which, together with the slip and GND density profiles across the strip, are in qualitative agreement with results found in the literature. The model has also been applied to simulate the constitutive behaviour of a polycrystal (consisting of a limited number of grains) under plane stress tension, where the specimen size has also been varied, resulting in varying intragranular heterogeneities. Next to the flow stress, also the (initial) yield stress depends on the grain size.

# Notation

---

In the following definitions, a Cartesian coordinate system with unit vector base  $\{\mathbf{e}_1, \mathbf{e}_2, \mathbf{e}_3\}$  applies and following the Einstein summation convention, repeated indices are summed from 1 to 3.

## Quantities

scalar	$\alpha, a, A$
vector	$\mathbf{a} = a_i \mathbf{e}_i$
second order tensor	$\boldsymbol{\alpha} = \alpha_{ij} \mathbf{e}_i \mathbf{e}_j, \mathbf{A} = A_{ij} \mathbf{e}_i \mathbf{e}_j$
higher ( $n$ th) order tensor	${}^n\mathbf{A} = A_{ij\dots n} \mathbf{e}_i \mathbf{e}_j \dots \mathbf{e}_n$
column	$\underline{a}$
matrix	$\underline{A}$

## Operations

multiplication	$c = ab, \mathbf{c} = \mathbf{a}\mathbf{b}, \mathbf{C} = \mathbf{a}\mathbf{B}$
dyadic product	$\mathbf{C} = \mathbf{a}\mathbf{b} = a_i b_j \mathbf{e}_i \mathbf{e}_j$
cross product	$\mathbf{c} = \mathbf{a} \times \mathbf{b}$
inner product	$c = \mathbf{a} \cdot \mathbf{b} = a_i b_i, \mathbf{C} = \mathbf{A} \cdot \mathbf{B} = A_{ij} B_{jk} \mathbf{e}_i \mathbf{e}_k$
double inner product	$\mathbf{C} = {}^4\mathbf{A} : \mathbf{B} = A_{ijkl} B_{lk} \mathbf{e}_i \mathbf{e}_j, c = \mathbf{A} : \mathbf{B} = A_{ij} B_{ji}$
conjugate / transpose	$\mathbf{C}^T = C_{ji} \mathbf{e}_i \mathbf{e}_j$
inverse	$\mathbf{A}^{-1}$
determinant	$\det(\mathbf{A}) = (\mathbf{A} \cdot \mathbf{e}_1) \cdot (\mathbf{A} \cdot \mathbf{e}_2) \times (\mathbf{A} \cdot \mathbf{e}_3)$

trace	$\text{tr}(\mathbf{A}) = \mathbf{A} : \mathbf{e}_i \mathbf{e}_i = A_{ii}$
deviatoric part	$\mathbf{A}_d = \mathbf{A} - \frac{1}{3} \text{tr}(\mathbf{A}) \mathbf{e}_i \mathbf{e}_i$
gradient operator	$\nabla = \mathbf{e}_i \frac{\partial}{\partial x_i}$
tensor derivative	$\frac{d\mathbf{A}}{d\mathbf{B}} = \frac{dA_{ij}}{dB_{lk}} \mathbf{e}_i \mathbf{e}_j \mathbf{e}_k \mathbf{e}_l$
absolute value	$ a $
euclidean norm	$\ \mathbf{a}\  = \sqrt{\mathbf{a} \cdot \mathbf{a}}$
time derivative	$\dot{a}$

### Crystallographic notation

crystallographic direction, family	$[uvw], \langle uvw \rangle$
crystallographic plane, family	$(hkl), \{hkl\}$
slip system, family	$(hkl)[uvw], \{hkl\}\langle uvw \rangle$

## CHAPTER ONE

# Introduction

---

**Abstract** / The basic principles behind the general crystal plasticity modelling are explained, as well as the motivation for incorporating different types of dislocation densities. An overview of the main characteristics and differences of the two developed strain gradient crystal plasticity approaches is given.

### 1.1 Physics of crystal plasticity

Crystallographic materials, such as metals, are characterised by a specific periodic arrangement of their atoms. This thesis focuses on the so-called “face-centered cubic” (FCC) arrangement, a structure which is common for widely used metals as aluminium and copper. In the constitutive modelling, the plastic deformation is typically based on the physical process of crystallographic slip, which is favourable along the most close-packed directions on the most close-packed crystallographic slip planes. Based on the specific atom arrangement, these directions and planes are set unambiguously, i.e. for FCC metals this leads to 3 dedicated slip directions on each of the 4 slip planes, resulting in 12 so-called “slip systems”. Next to the plastic deformation, it is assumed that the (small) elastic deformation can be accommodated by stretching the crystallographic lattice.

As the intrinsic strength of a perfect crystal is theoretically two to four orders of magnitude higher than the actually observed strength, this discrepancy can only be resolved by the introduction of the concept of dislocations (Orowan, 1934). Orowan reasoned that the actual mechanism of crystallographic slip must be the movement of dislocations. Under an applied stress, the lattice deforms elastically until the stretched bonds near a dislocation break down and new bonds are formed. During this repeating process, a part of the crystal slips one interatomic distance with respect to the other part, typically in the direc-

tion and over a distance of one Burger's vector. Instead of the ideal strength associated with the movement of an entire slip plane, the dislocations enable only sections of the slip plane to shear, resulting in the observed decimated strengths necessary for plastic deformation.

Next to their role of accommodating the plastic deformation in crystalline materials, the work hardening behaviour of metals can also be attributed to the dislocations, namely by means of their multiplication with ongoing plastic deformation and their mutual interactions that impede the motion of gliding dislocations (i.e. strengthening by obstacle formation). The evolution mechanism can be split into two parts, i.e. the accumulation of the statistically-stored dislocations (SSD's) and the formation of geometrically-necessary dislocations (GND's) (Ashby, 1970). The SSD's accumulate by a statistical trapping process during plastic slip and are therefore randomly oriented, i.e. not having any deformational effects. On the other hand, once the applied load, or the material structure itself, involves any gradient of plastic deformation, a certain amount of GND's are required to preserve lattice compatibility and to accomplish the required lattice rotation. Because of their inherent geometrical nature, the GND densities can often be determined explicitly, together with their orientation (dislocation sign). Conventional crystal plasticity theories, however, do not take into account these effects. This results in the fact that their strengthening mechanisms are inherently incapable of predicting scale dependent behaviour, i.e. different mechanical responses due to varying plastic strain *gradients*.

## 1.2 Objective, strategy and outline

This thesis presents the development of both a polycrystal and a single crystal strain gradient crystal plasticity model that is capable of predicting length scale dependences, based on the hypothesis

*Predicting the scale dependent behaviour in a physically realistic manner can be accomplished by taking into account the GND densities and their constitutive influence in the crystal plasticity framework, along with the introduction of several appropriate physical length scales.*

Especially, the attention is focused on prediction of the Hall-Petch relation (Hall, 1951; Petch, 1953; Armstrong et al., 1962). This relation describes the flow stress increase once the metal's grain size decreases, which is a well-known consequence of material induced plastic inhomogeneities, caused by the fact that grain boundaries –next to dislocation interactions– can also act as obstacles to crystallographic slip.

In the next chapter, a polycrystal approach is presented, i.e. an approach which considers a collection of grains that is assumed to be present in a single material point. The effects of grain boundaries are taken into account by bi-crystal volume elements, each having

the crystallographic lattice orientation of the adjacent crystal, whereas single crystal volume elements represent the grain cores. The GND densities can then be determined by implementation of the restrictions at the grain boundaries through deformation compatibility and stress equilibrium requirements at the bi-crystal interfaces representing those boundaries. The plastic deformation incompatibilities between the crystal core and the bi-crystal boundaries are exploited as a measure for the required GND densities to preserve lattice continuity. However, several ambiguous choices have to be made using the presented polycrystal approach, concerning the proper dimensional ratio between the crystal core and the grain boundary region and concerning the correct incorporation of the additional GND density strength in the phenomenological slip resistance description at hand.

Therefore, in Chapter 3 and 4, an assembly of grains is considered and for each individual grain, a detailed single crystal approach is developed, with an internally inhomogeneous distribution of relevant quantities. In the context of a finite element elaboration, each grain is subdivided into an appropriate number of finite elements in order to be able to describe the intragranular inhomogeneities. The GND densities, which are now *directly* related to the gradients of crystallographic slip, are considered as additional nodal degrees of freedom in the finite element formulation, offering several advantages. First, the associated additional boundary conditions provide the opportunity to obstruct the crystallographic slip at the grain boundaries in a way which is substantially more appropriate with respect to reality than the bi-crystal obstructions. Furthermore, a certain distribution of initial grain boundary dislocation (GBD) densities can be introduced, related to the different lattice orientations of neighbouring grains. A simplified procedure for the determination of these GBD density fields is also presented. Next to the slip resistance as caused by the (short-range) interactions of all SSD's and GND's, any heterogeneity in the GND density field also causes a long-range influence on crystallographic slip, namely through a resulting back-stress contribution. This second influence of the GND densities is caused by the fact that at a length scale of several orders of magnitude larger than the individual dislocation size, in contrast to the SSD densities, the net effect of the GND densities does not vanish.

In Chapter 3, the entire framework is discussed in detail, after which it is applied to simulate the size dependent behaviour of a single crystal strip under plane strain shear, which is micromechanically clamped at the shear loaded edges. Next, in Chapter 4, the numerical implementation of the developed strain gradient crystal plasticity framework is outlined, which is succeeded by the modelling of the grain size dependent mechanical behaviour of a polycrystal strip under plane stress tension. Finally, in Chapter 5, the ambiguous choice of identifying the grain boundary region while using the polycrystal approach is reconsidered with the aid of single crystal simulations.



## CHAPTER TWO

# Polycrystal model<sup>1</sup>

---

**Abstract** / A strain gradient dependent crystal plasticity approach is used to model the constitutive behaviour of polycrystal FCC metals under large plastic deformation. Material points are considered as aggregates of grains, subdivided into several fictitious grain fractions: a single crystal volume element stands for the grain interior whereas grain boundaries are represented by bi-crystal volume elements, each having the crystallographic lattice orientations of its adjacent crystals. A relaxed Taylor-like interaction law is used for the transition from the local to the global scale. It is relaxed with respect to the bi-crystals, providing compatibility and stress equilibrium at their internal interface. During loading, the bi-crystal boundaries deform dissimilar to the associated grain interior. Arising from this heterogeneity, a geometrically necessary dislocation (GND) density can be computed, which is required to restore compatibility of the crystallographic lattice. This effect provides a physically based method to account for the additional hardening as introduced by the GND's, the magnitude of which is related to the grain size. Hence, a scale-dependent response is obtained, for which the numerical simulations predict a mechanical behaviour corresponding to the Hall-Petch effect. Compared to a full-scale finite element model reported in the literature, the present polycrystalline crystal plasticity model is of equal quality yet much more efficient from a computational point of view for simulating uniaxial tension experiments with various grain sizes.

## 2.1 Introduction

It is well known that the grain size has a dominant influence on the mechanical behaviour of polycrystalline metals and alloys. This dependence is not taken into account by approaches as proposed by Taylor (1938). In the past, many applications of Taylor-type models (e.g. Asaro and Needleman, 1985) have been used for describing the behaviour and texture evolution of FCC polycrystals during large plastic deformation. Additionally, Bronkhorst et al. (1992) showed that the Taylor model provides an acceptable

---

<sup>1</sup>This chapter is reproduced from Evers et al. (2002).



description of the behaviour of single-phase FCC polycrystals under pure slip deformation. However, in this model, a homogeneous deformation field across grain boundaries and within grains is assumed, neglecting differences in structure from grain to grain and within grains. Nevertheless, the continuity across grain boundaries could also be upheld when the deformation inside a grain was inhomogeneous, in other words if the crystal boundary region deformed dissimilar from the crystal interior (Kochendörfer, 1941). This hypothesis initiated the suggestion by Nabarro (1950) and Boas (1950) that the flow stress might depend on the grain size. In fact, it is this hypothesis which constitutes the basis of the presented micromechanical model.

Hall (1951) and Petch (1953) first examined the grain size dependence and found an empirical relationship between the crystal size  $d$  and the yield stress, which was extended by Armstrong et al. (1962) to include the entire flow stress region  $\sigma(\varepsilon)$  by expressing the parameters  $\sigma_0$  and  $k$  to be dependent on the strain level  $\varepsilon$  in a relation known as the (extended) “Hall-Petch relation”

$$\sigma(\varepsilon) = \sigma_0(\varepsilon) + k(\varepsilon)d^{-n}. \quad (2.1)$$

In literature, values for the exponent  $n$  in the range of 0.3 to 1 show the best resemblance with experimental findings, whereas  $n = \frac{1}{2}$  is the most reported value. The Hall-Petch slope  $k$  characterizes the transfer of slip through the grain boundaries. For a more detailed discussion of the flow stress dependence on the grain size, see Hansen (1982) and Narutani and Takamura (1991), and references therein.

Three different models can be distinguished (Gavriljuk et al., 1999) which explain the strengthening effect of smaller grains. First, the “dislocation pile-up models” state that the propagation of plastic deformation is obstructed at the crystal boundaries by stress concentrations as caused by the pile-up of dislocations, which on their term activate dislocation sources in neighbouring grains (Hall, 1951; Petch, 1953; Cottrell, 1958; Nakanishi and Suzuki, 1974; Suzuki and Nakanishi, 1975). These models focus on the restricted dislocation *movement* across grain boundaries, which affect the flow stress in Eq. (2.1) through  $d^{-\frac{1}{2}}$ . The main objection against this explanation is that in metals with a BCC crystal structure, no pile-ups are observed while the Hall-Petch relation is nevertheless retrieved. Second, the “dislocation interaction models” (or “work hardening models”) (Ashby, 1970; Hirth, 1972; Conrad, 1963; Dai and Parks, 1997; Dai, 1997; Arsenlis and Parks, 2000) emphasize the increased *concentration* of dislocations by affirming that the dislocation density accumulated in a grain at a certain strain is higher once the grain size decreases, which is inherent to the increased inhomogeneous deformation (i.e. strain gradients) within the grain and the accompanying decreasing mean free path of the dislocations. These models predict values for the exponent  $n$  in the total range mentioned. Finally, the “grain boundary source model” (Li and Chou, 1970) emphasizes on the capacity of grain boundaries to emit dislocations under loading, which does not require a stress concentration created by a pile-up. However, up till now, no clear experimental evidence has been able to support the exclusive validity of either of these models.

The dislocation interaction approach has been extended by Ashby (1970). Hardening, i.e. resistance to dislocation motion, is caused by secondary dislocations piercing the slip planes, which multiply during plastic deformation and increase the slip resistance. In that work, a distinction is made between statistically-stored dislocations (SSD's), accumulating during a uniform deformation, and geometrically necessary dislocations (GND's), which are required to preserve lattice compatibility in case of unevenly distributed plastic slip (non-uniform plastic deformation, such as in the presence of lattice curvature). As suggested by Kocks (1970) and sustained by Thompson et al. (1973), geometrically necessary dislocations are largely concentrated in the grain boundary regions where the lattice mismatch is most pronounced. Supporting this, Kazmi and Murr (1979) highlighted the formation of high dislocation densities in the vicinity of grain boundaries by means of transmission electron microscopy.

Several strain gradient models have been developed in order to numerically capture scale size effects (e.g. Aifantis, 1987; Fleck et al., 1994; Fleck and Hutchinson, 1997; Gao et al., 1999; Huang et al., 2000; Shu and Fleck, 1999; Dai and Parks, 1997; Dai, 1997; Shi et al., 2000). Such approaches incorporate a length scale in the analytical plasticity formulation, thereby enabling the prediction of e.g. particle size effects and indenter size effects. The underlying physics is sometimes related to the SSD and GND generation (Gao et al., 1999). However, limitations are met with respect to two-dimensional idealizations of double slip and the consideration of global strain gradients instead of intragranular strain gradients, respectively absent and present in a macroscopically uniform deformation mode. In the present chapter, a scale-dependent theory of plastic strain gradient induced production of GND's is elaborated, based on the work of Arsenlis and Parks (2000), in the context of which intragranular strain gradients can be accounted for.

In the presented model (see also Evers et al., 2001), each crystallographic orientation in a material point is associated with a grain. This grain is considered to have a material volume fraction assigned to its core, whereas the remaining volume fraction is covered by its boundary volume elements. The heterogeneous deformation within a crystal, typically occurring between the crystal core and the grain boundaries, initiates the generation (either through nucleation or dislocation motion) of geometrically necessary dislocations to maintain lattice compatibility. These GND's cause in their turn the slip resistance near the grain boundaries to increase, as experimentally shown by Worthington and Smith (1964). This extra hardening is merely assigned to the boundary volume elements. Despite of the fact that in this way the dislocations are practically "stored" (piled up) near the boundaries, this model mainly lies in the range of the "dislocation interaction models".

Note that the grain diameter is a model parameter used to determine the measure of inhomogeneity. No explicit flow stress relation depending on the grain diameter (according to e.g. Eq. (2.1)) is included in the model (cf. Thompson et al., 1973). Furthermore, the approach of Meyers and Ashworth (1982) and its extension by Fu et al. (2001) also relied on

a subdivision of grains into an interior section and a surrounding grain boundary region. The grain subdivision is based on the increased hardening rate near the grain boundaries (experimentally verified by Gray III et al. (1999)), an observation which is expected to be the result of the compatibility requirements near those boundaries. Subsequently, Fu et al. took this effect into account through different evolution coefficients of the dislocation densities in the core and near the boundaries. Moreover, again, a flow stress relation was required in which the diameter dependence entered explicitly (in this case through geometrical considerations). In the approach presented in this contribution, on the other hand, the constitutive material parameters are kept equal in the core and in the grain boundary layer (the bi-crystals) and the increased hardening term in the grain boundary section only arises to the extent in which it is physically motivated, i.e. only when there is -and in proportion to- a deformation incompatibility.

The constitutive crystal plasticity framework is based on the work of Bronkhorst et al. (1992) and Kalidindi et al. (1992). However, in such local continuum constitutive models, no explicit attention is paid to the presence of GND's and no absolute length scale enters the formulations. Therefore, they implicitly assume that the accumulation of SSD's is the only driving force behind the work hardening, which is related to the history of the crystallographic plastic shear strains.

As mentioned before, Taylor-type models assume deformation uniformity within grains and across grain boundaries, violating the stress equilibrium condition at the interfaces. Alternatively, their counterpart, the Sachs-type models, assume the stress to be uniform, neglecting kinematical compatibility. In the case of intermediate models, the consideration of intergranular processes accounts for both the consistency conditions of grain boundary compatibility and traction equilibrium to be satisfied. This makes intermediate models, such as for example the self-consistent models, more rational. Self-consistent approaches, however, involve severe assumptions in order to simplify the formulations and to reduce the computation time (Molinari et al., 1997). The present contribution contains an alternative intermediate model, which is based on a relaxed form of the Taylor assumption. Unlike the classical assumption, here, one grain consists of *several* fractions (i.e. representative volume elements). The crystal interior is modelled by one single crystal volume element, whereas several bi-crystal volume elements represent the grain boundaries. The Taylor assumption is now applied to the deformation of the single crystal core and the *average* deformation of each bi-crystal component. Additionally, at the interface within the bi-crystals, the consistency conditions of deformation compatibility and stress equilibrium are imposed. In this way, the above-mentioned intragranular deformation heterogeneity arises, which is here concentrated between the core and the bi-crystals of each grain.

The approach of using a bi-crystal in combination with Taylor's assumption originates from the work of Ahzi et al. (1990), where a two-phase composite inclusion was used as a representative volume element of crystalline lamella and its associated amorphous

layer in two-phase semi-crystalline polymers (see also Van Dommelen et al., 2003). The extension of this approach for the modelling of grain boundaries of FCC metals by choosing the composite inclusion to be a bi-crystal, having the lattice orientations of the two neighbouring crystals, was first performed by Lee et al. (1999). However, in their contribution, only the crystal interfaces are taken into account, leaving the crystal interiors unconsidered. Furthermore, Delannay et al. (1999) refers to a similar approach of bi-crystal modelling by means of the “Lamel model”. An empirical examination of the presence of GND’s near the grain boundaries of an aluminium bi-crystal, measured through lattice curvatures, can be found in Sun et al. (2000).

First, the general crystal plasticity constitutive framework and its time integration are outlined in Section 2.2. Next, in Section 2.3, the subdivision of a grain into a core and several bi-crystal boundaries is discussed, along with the complementary time integration procedure. In Section 2.4, the deformation incompatibility between the core and the boundaries is considered, which induces the production and accumulation of GND’s. This extra dislocation density obstructs the dislocation motion and hence introduces enhanced hardening. Further, in Section 2.5, the computational results of uniaxial tensile tests are compared to experimental results obtained by Hansen (1979) and to numerical results obtained by Arsenlis and Parks (2000), both describing Hall-Petch-like behaviour. Arsenlis and Parks considered a collection of grains, where each grain is discretized in finite elements. Hereby, the strain gradients arise from the deformation heterogeneity between the different finite elements, i.e. between elements near the core and elements near the boundary. From those strain gradients, the enhanced hardening arises and the corresponding slip resistance can be determined after consideration of the GND densities. Finally, concluding remarks are made in Section 2.6.

## 2.2 Crystal plasticity framework: single crystal approach

### 2.2.1 Kinematics

The kinematics commonly used in the field of crystal plasticity may be traced back to the works of Lee (1969), Rice (1971), Hill and Rice (1972), and Asaro and Rice (1977). The basic feature is the distinction between two physical mechanisms, represented by the multiplicative decomposition of the deformation gradient tensor

$$F = F_e \cdot F_p. \quad (2.2)$$

The elastic part  $F_e$  comprises the small lattice deformation and possibly large rigid body rotation. The plastic part  $F_p$  corresponds to the isochoric and stress-free intermediate configuration, in which the crystallographic lattice is unaltered and unrotated with respect to the reference configuration (Mandel, 1974), as illustrated in Fig. 2.1. It is assumed that this part results solely from continuous plastic shearing (dislocation motion)

on well-defined slip systems. For FCC metals, 12 favourable (octahedral) systems can be characterized by the Miller indices  $\{111\}\langle 110\rangle$ , where each system  $\alpha$  ( $\alpha = 1, 2, \dots, 12$ ) is represented in the reference configuration by the two time-independent orthonormal vectors  $\mathbf{m}_0^\alpha$  and  $\mathbf{n}_0^\alpha$ , the slip direction and slip plane normal, respectively. Now, the evolution of the plastic deformation can by definition be expressed as the superposition of all crystallographic slip rates  $\dot{\gamma}^\alpha$  (Rice, 1971)

$$\dot{\mathbf{F}}_p = \mathbf{L}_p \cdot \mathbf{F}_p, \quad \mathbf{L}_p = \sum_{\alpha} \dot{\gamma}^\alpha \mathbf{P}_0^\alpha, \quad \mathbf{P}_0^\alpha \equiv \mathbf{m}_0^\alpha \mathbf{n}_0^\alpha, \quad (2.3)$$

where  $\mathbf{L}_p$  is the plastic velocity gradient tensor and  $\mathbf{P}_0^\alpha$  is known as the non-symmetric Schmid tensor.

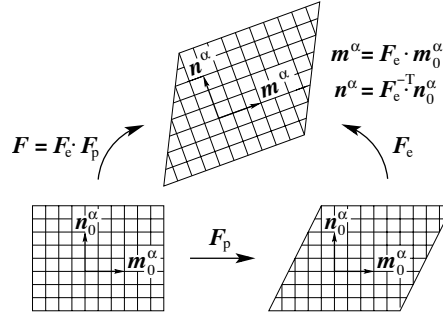


Figure 2.1 / Multiplicative decomposition of the deformation gradient tensor.

## 2.2.2 Constitutive model

The second Piola-Kirchhoff stress measure defined with respect to the relaxed configuration

$$\boldsymbol{\tau} \equiv \det(\mathbf{F}_e) \mathbf{F}_e^{-1} \cdot \boldsymbol{\sigma} \cdot \mathbf{F}_e^{-T}, \quad (2.4)$$

with  $\boldsymbol{\sigma}$  the Cauchy stress tensor, is taken to be related to its work conjugated elastic Green strain measure  $\mathbf{E}_e$  through

$$\boldsymbol{\tau} = {}^4\mathbf{C} : \mathbf{E}_e, \quad \mathbf{E}_e \equiv \frac{1}{2} (\mathbf{C}_e - \mathbf{I}), \quad \mathbf{C}_e \equiv \mathbf{F}_e^T \cdot \mathbf{F}_e, \quad (2.5)$$

where  $\mathbf{C}_e$  is the elastic right Cauchy-Green tensor and  $\mathbf{I}$  is the second-order unit tensor. The fourth-order isotropic elasticity tensor  ${}^4\mathbf{C}$  is defined by Young's modulus  $E$  and Poisson's ratio  $\nu$

$${}^4\mathbf{C} = \frac{\nu E}{(1+\nu)(1-2\nu)} \left( \mathbf{I}\mathbf{I} + \frac{1-2\nu}{\nu} {}^4\mathbf{I} \right), \quad (2.6)$$

where  ${}^4\mathbf{I}$  is the symmetric fourth-order unit tensor.

To arrive at an elasto-viscoplastic material model, the plastic shearing rate  $\dot{\gamma}^\alpha$  is expressed as a power law function of the slip system resolved shear stress  $\tau^\alpha$  and deformation resistance  $s^\alpha$  according to the flow rule (Hutchinson, 1976; Peirce et al., 1982)

$$\dot{\gamma}^\alpha = \dot{\gamma}_0 \left\{ \frac{|\tau^\alpha|}{s^\alpha} \right\}^{\frac{1}{m}} \text{sign}(\tau^\alpha), \quad (2.7)$$

where  $\dot{\gamma}_0$  and  $m$  are material parameters representing the reference plastic strain rate and the rate sensitivity exponent, respectively. The ‘‘Schmid stress’’  $\tau^\alpha$  is defined such that  $\sum_\alpha \tau^\alpha \dot{\gamma}^\alpha$  is precisely the rate of plastic work per unit volume in the relaxed configuration (Asaro and Rice, 1977; Bronkhorst et al., 1992)

$$\tau^\alpha \equiv \mathbf{C}_e \cdot \boldsymbol{\tau} : \mathbf{P}_0^\alpha. \quad (2.8)$$

For metallic materials, the elastic strains are usually negligibly small. For this situation, the resolved shear stress  $\tau^\alpha$  in Eq. (2.8) may be approximated by

$$\tau^\alpha \doteq \boldsymbol{\tau} : \mathbf{P}_0^\alpha. \quad (2.9)$$

The slip resistance  $s^\alpha$  in Eq. (2.7) is taken to evolve according to the expression (Asaro, 1983; Kalidindi et al., 1992)

$$\dot{s}^\alpha = \sum_\beta h^{\alpha\beta} |\dot{\gamma}^\beta|, \quad s^\alpha(t=0) = \tau_0, \quad (2.10)$$

where  $\tau_0$  is the initial slip resistance, which is considered to be equal for each slip system. The hardening moduli  $h^{\alpha\beta}$  give the rate of strain hardening on slip system  $\alpha$  due to slip on slip system  $\beta$ . For now, this occurrence of self and latent hardening is phenomenologically described by

$$h^{\alpha\beta} = q^{\alpha\beta} h^\beta \quad (\text{no sum on } \beta), \quad (2.11)$$

where  $q^{\alpha\beta}$  equals unity for coplanar slip systems and the scalar value  $q$  for non-coplanar systems. This choice has been motivated by experimental observations performed by Kocks (1970). Finally, the following specific form for the single-slip hardening rate,  $h^\beta$  in Eq. (2.11) is adopted, which was originally motivated by the work of Brown et al. (1989)

$$h^\beta = h_0 \left( 1 - \frac{s^\beta}{s_\infty} \right)^a, \quad (2.12)$$

with the slip system hardening parameters  $h_0$ ,  $a$  and  $s_\infty$ .

### 2.2.3 Time integration

For each single or bi-crystal volume element of each grain, each having a unique lattice orientation(s), the constitutive response as well as the history-dependent variables differ from those of other volume elements with a different orientation, undergoing the same deformation. Therefore, the proposed computational procedure is performed per volume element. First, in this section, the single crystal elements are considered. Next, in Section 2.3.2, the complementary time integration procedure for bi-crystal components is given.

Such as typical in implicit finite element codes, for each time increment, an estimated displacement field is used to calculate the stress and to update the state variables in each integration point. This process is repeated for a number of iterations until equilibrium of the global forces is realized for the particular time increment. Consequently, at each new time step ( $t_{n+1} = t_n + \Delta t$ , in the remainder of this chapter, associated variables are denoted with the subscript  $n + 1$ ), the plastic deformation and the slip restrictions at the previous time ( $t_n$ , variables with subscript  $n$ ) are known state variables. Furthermore, the time-independent material parameters and slip system orientations of the grain under consideration are known.

The implicit integration procedure (Eqs. (2.13)–(2.21)) is based on the contributions of Bronkhorst et al. (1992) and Kalidindi et al. (1992) and starts with the time integration of Eq. (2.3)

$$\mathbf{F}_{\mathbf{p}_{n+1}} = \exp(\Delta t \mathbf{L}_{\mathbf{p}_{n+1}}) \cdot \mathbf{F}_{\mathbf{p}_n}, \quad (2.13)$$

which can be approximated by

$$\mathbf{F}_{\mathbf{p}_{n+1}} \doteq (\mathbf{I} + \Delta t \mathbf{L}_{\mathbf{p}_{n+1}}) \cdot \mathbf{F}_{\mathbf{p}_n}. \quad (2.14)$$

Correspondingly, the first-order estimation of the inverse of  $\mathbf{F}_{\mathbf{p}_{n+1}}$  can be written as

$$\mathbf{F}_{\mathbf{p}_{n+1}}^{-1} \doteq \mathbf{F}_{\mathbf{p}_n}^{-1} \cdot (\mathbf{I} - \Delta t \mathbf{L}_{\mathbf{p}_{n+1}}). \quad (2.15)$$

To compute the stress at the end of the time step,  $\mathbf{F}_{\mathbf{e}_{n+1}}$ , determined by

$$\mathbf{F}_{\mathbf{e}_{n+1}} = \mathbf{F}_{n+1} \cdot \mathbf{F}_{\mathbf{p}_{n+1}}^{-1}, \quad (2.16)$$

is substituted into Eq. (2.5), which after employing Eq. (2.15) leads to

$$\boldsymbol{\tau}_{n+1} = {}^4\mathbf{C} : \left\{ \frac{1}{2} (\mathbf{A} - \mathbf{I}) - \frac{1}{2} \Delta t \left( \mathbf{A} \cdot \mathbf{L}_{\mathbf{p}_{n+1}} + \mathbf{L}_{\mathbf{p}_{n+1}}^T \cdot \mathbf{A} \right) \right\}, \quad (2.17)$$

with

$$\mathbf{A} \equiv \mathbf{F}_{\mathbf{p}_n}^{-T} \cdot \mathbf{F}_{n+1}^T \cdot \mathbf{F}_{n+1} \cdot \mathbf{F}_{\mathbf{p}_n}^{-1}. \quad (2.18)$$

When the plastic velocity gradient tensor is written in the crystallographic form of Eq. (2.3), Eq. (2.17) ends up like

$$\boldsymbol{\tau}_{n+1} = \boldsymbol{\tau}^{\text{tr}} - \sum_{\alpha} \Delta t \dot{\gamma}_{n+1}^{\alpha} (\boldsymbol{\tau}_{n+1}, s_{n+1}^{\alpha}) \mathbf{B}^{\alpha}, \quad (2.19)$$

with the trial stress (elastic prediction)

$$\boldsymbol{\tau}^{\text{tr}} \equiv {}^4\mathbf{C} : \left\{ \frac{1}{2} (\mathbf{A} - \mathbf{I}) \right\} \quad (2.20)$$

and

$$\mathbf{B}^{\alpha} \equiv {}^4\mathbf{C} : \left\{ \frac{1}{2} (\mathbf{A} \cdot \mathbf{P}_0^{\alpha} + \mathbf{P}_0^{\alpha\text{T}} \cdot \mathbf{A}) \right\}. \quad (2.21)$$

Using this approach, the introduced variables ( $\mathbf{A}$ ,  $\boldsymbol{\tau}^{\text{tr}}$  and  $\mathbf{B}^{\alpha}$ ) are known at time  $t_{n+1}$ , leaving only the stress  $\boldsymbol{\tau}_{n+1}$ , slip rates  $\dot{\gamma}_{n+1}^{\alpha}$  and slip resistances  $s_{n+1}^{\alpha}$  to be computed.

The slip rates are computed using Eq. (2.7) and substituting the implicit time integration of Eq. (2.10) into this equation leads to

$$\dot{\gamma}_{n+1}^{\alpha} = \dot{\gamma}_0 \left\{ \frac{|\tau_{n+1}^{\alpha}|}{s_n^{\alpha} + \Delta t \sum_{\beta} h^{\alpha\beta} |\dot{\gamma}_{n+1}^{\beta}|} \right\}^{\frac{1}{m}} \text{sign}(\tau_{n+1}^{\alpha}). \quad (2.22)$$

Of all slip systems  $\alpha$  and at time  $t_{n+1}$  (for the sake of clarity, the incremental indices  $n+1$  will be omitted in the remainder of this section), the slip rates and stress components in Eq. (2.22) are placed in the columns  $\dot{\gamma}$  and  $\boldsymbol{\tau}$ , whereas the right-hand side will be referred to as  $\Gamma(\dot{\gamma}, \boldsymbol{\tau})$ . The column  $\boldsymbol{\tau}$  contains the 6 independent components of the stress measure  $\boldsymbol{\tau}$ , resulting in the Schmid stresses  $\tau^{\alpha}$  after employing Eq. (2.8). At a given stress state, the 12 slip rates in  $\dot{\gamma}$  are solved by Newton-Raphson iterations

$$\Phi(\dot{\gamma}, \boldsymbol{\tau}) = \dot{\gamma} - \Gamma(\dot{\gamma}, \boldsymbol{\tau}) = \underline{0}. \quad (2.23)$$

To actually determine the stress column  $\boldsymbol{\tau}$ , Eq. (2.19) is also solved using a Newton-Raphson iteration procedure. With respect hereto, a distinct formulation of the derivatives of the slip rates with respect to the stress components of  $\boldsymbol{\tau}$  ( $\frac{d\dot{\gamma}}{d\boldsymbol{\tau}}$ ) is required to construct a consistent tangent. For this purpose, the ansatz is that Eq. (2.23) must remain satisfied for all variations of  $\boldsymbol{\tau}$

$$\frac{d\Phi}{d\boldsymbol{\tau}} = \underline{0}, \quad (2.24)$$

with  $\underline{0}$  the zero matrix ( $12 \times 6$ ). This can be expanded to

$$\frac{d\Phi}{d\boldsymbol{\tau}} = \left( \frac{\partial \Phi}{\partial \boldsymbol{\tau}} + \frac{\partial \Phi}{\partial \dot{\gamma}} \frac{d\dot{\gamma}}{d\boldsymbol{\tau}} \right) = \underline{0}. \quad (2.25)$$



The derivatives  $\frac{d\dot{\gamma}}{d\tau}$  are released through rearrangement of this linear equation

$$\frac{d\dot{\gamma}}{d\tau} = - \left( \frac{\partial \Phi}{\partial \dot{\gamma}} \right)^{-1} \frac{\partial \Phi}{\partial \tau}. \quad (2.26)$$

Now, the system can be solved for both the slip rates  $\dot{\gamma}$  and the slip system resistances. Recapitulating, this iteration procedure (for solving the slip rates and resistances) is performed for each stress state, i.e. during each iteration of the Newton-Raphson procedure of the overall system of equations.

## 2.3 Intragranular decomposition: bi-crystal approach

### 2.3.1 Modified Taylor approach

As an interaction strategy for relating the mechanical behaviour of the microstructure to macroscopically imposed deformation conditions, following Taylor's model, the stress at each macroscopic continuum material point is determined by the averaged response of the microstructural constituents comprising that material point.

However, the classical Taylor assumption enforces the deformation of each individual grain in a material point to be uniform and equal to the macroscopic deformation, disregarding any interactions between grains or inside grains. In reality though, the intragranular deformation in general is heterogeneous, and at the grain boundaries, equilibrium of mechanical forces must hold (Becker and Panchanadeeswaran, 1995). Therefore, in the presented intermediate model, these discrepancies are partially amended by relaxing the Taylor approach.

Each grain is fictitiously subdivided into a core and several grain boundary fractions, represented by a single crystal and bi-crystals, respectively. This subdivision is shown two-dimensionally in Fig. 2.2. The crystal lattice orientation of the bi-crystal fragment situated next to the core (interior-side part "i") initially resembles that of the core, whereas the exterior-side part "e" of the bi-crystal has the same initial crystallographic orientation as its neighbouring crystal.

At the end, for each grain "k", the Cauchy stress  $\sigma^k$  is computed by volume-averaging the stresses of each of the constituents, i.e. the stress in the single crystal core  $\sigma^{k,c}$  and the stresses in the  $N_b^k$  bi-crystals  $\sigma^{k,b}$

$$\sigma^k = \vartheta \sigma^{k,c} + (1 - \vartheta) \frac{1}{N_b^k} \sum_{b=1}^{N_b^k} \sigma^{k,b}, \quad (2.27)$$

where  $\vartheta$  ( $0 \leq \vartheta \leq 1$ ) is the volume fraction of the crystal core (cf. Eq. (2.35) in Section 2.4). In this fashion, the contribution of each bi-crystal of grain k is weighted equally. Finally,

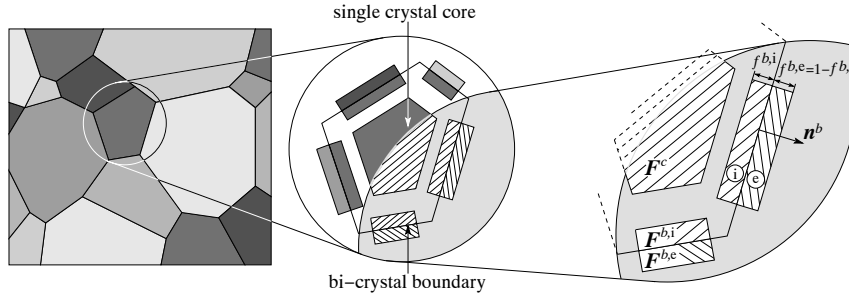


**Figure 2.2** / From a polycrystal assembly, each crystal is decomposed into constituent parts, representing its core and its boundaries.

in parallelism to Asaro and Needleman (1985), for the determination of the macroscopic stress, all grains are assumed to be equally sized.

$$\bar{\sigma} = \frac{1}{N_k} \sum_{k=1}^{N_k} \sigma^k, \quad (2.28)$$

where  $N_k$  is the number of grains with an independent crystallographic orientation considered in the material point under investigation. In the following, the attention is focussed on the entire crystal, including the core and the associated bi-crystals (the superscript “ $k$ ” is omitted as from now).

Considered more thoroughly, the deformation of the grain interior is still imposed to be uniform and equal to the macroscopic deformation gradient  $\bar{F}$ , in accordance to the classical Taylor assumption

$$F^c = \bar{F}. \quad (2.29)$$

On the other hand, only the *average* of the two individually uniform deformation gradients of the bi-crystal fragments,  $F^{b,i}$  and  $F^{b,e}$ , is enforced to equal the macroscopic deformation gradient

$$f_0^{b,i} F^{b,i} + f_0^{b,e} F^{b,e} = \bar{F}, \quad f_0^{b,i} + f_0^{b,e} = 1, \quad (2.30)$$

where  $f_0^{b,i}$  and  $f_0^{b,e}$  are the initial volume fractions of the interior and exterior sections of the bi-crystal element “ $b$ ”, respectively.

For the calculation of the stress in the crystal core  $\sigma^c$ , the relations of Sections 2.2.2 and 2.2.3 are to be used. For the computation of the two bi-crystal stresses,  $\sigma^{b,i}$  and  $\sigma^{b,e}$ , additional restrictions have to be formulated. In the plane of the interface between the two crystals in the bi-crystal, state variables are enforced to be uniformly distributed, i.e. only variations of quantities perpendicular to the interface are of interest. First, at the

bi-crystal interface, the condition of kinematical compatibility must hold, only admitting variations between the deformation gradients  $\mathbf{F}^{b,i}$  and  $\mathbf{F}^{b,e}$  in the direction of the initial outward interface normal  $\mathbf{n}_0^b$ , cf. Fig. 2.2. After consideration of Eq. (2.30), the deformation gradients can be written according to

$$\begin{aligned}\mathbf{F}^{b,i} &= \bar{\mathbf{F}} + f_0^{b,e} \mathbf{a} \mathbf{n}_0^b \\ \mathbf{F}^{b,e} &= \bar{\mathbf{F}} - f_0^{b,i} \mathbf{a} \mathbf{n}_0^b,\end{aligned}\tag{2.31}$$

with  $\mathbf{a}$  an a priori unknown vector. Second, in addition to compatibility, stress equilibrium at the interface in the deformed state is enforced through the condition

$$(\boldsymbol{\sigma}^{b,i} - \boldsymbol{\sigma}^{b,e}) \cdot \mathbf{n}^b = \mathbf{0}, \quad \mathbf{n}^b = \frac{\bar{\mathbf{F}}^{-T} \cdot \mathbf{n}_0^b}{\|\bar{\mathbf{F}}^{-T} \cdot \mathbf{n}_0^b\|}.\tag{2.32}$$

Note that this equation includes the instantaneous interface orientation  $\mathbf{n}^b$ , whereas in Eq. (2.31), the initial orientation  $\mathbf{n}_0^b$  is used.

### 2.3.2 Time integration

Regarding the time integration, besides solving the Piola-Kirchhoff stresses in both bi-crystal fragments using the approach given in Sections 2.2.2 and 2.2.3, the internal deformation gradient variation  $\mathbf{a}_{n+1}$  has to be determined simultaneously. The set of equations is therefore naturally completed by the traction equilibrium condition (2.32). The entire system of coupled equations is then solved using the Newton-Raphson iterative procedure. Finally, the bi-crystal stress (at time  $t_{n+1}$ ), as required in Eq. (2.27), is taken equal to the (uniform) stress of the interior-side part,  $\boldsymbol{\sigma}^{b,i}$ .

## 2.4 Enhanced hardening

The potential existence of heterogeneous intragranular deformations is the point of departure for this section. Within each grain, the deformation incompatibility between the core and the interior bi-crystal parts, sections with initially equal lattice orientations, requires the generation of geometrically necessary dislocations (GND's). First, the densities of GND's between the core and each bi-crystal component are determined. Next, in addition to the "conventional" slip resistance  $s^\alpha$  in Eq. (2.10), an extra term is introduced, based on the GND densities.

The evolution of the statistically-stored dislocations (SSD's) has no geometric consequences and is recognised as the motive behind the conventional slip system strength  $s^\alpha$ . From now on this strength will be denoted as  $s_{\text{SSD}}^\alpha$ , while the extra term related to the GND's will henceforth be denoted as  $s_{\text{GND}}^\alpha$ .

### 2.4.1 GND density

In this section, the GND densities between the core of a particular grain and one of its bi-crystal boundary elements are scrutinized. The same approach applies to the remaining bi-crystals as well as the other grains in the material point. A measure for the plastic deformation incompatibility is given by Nye's dislocation tensor (cf. Nye, 1953; Mura, 1987), which is defined as the curl of  $F_p$  (Dai, 1997)

$$\Lambda \equiv - \left( \nabla_0 \times F_p^T \right)^T. \quad (2.33)$$

Physically, this tensor can be interpreted as a measure for the closure failure (cumulative Burger's vector) of the contour enclosing an infinitesimal surface when the inner product of Nye's tensor with the surface unit normal vector is integrated over that surface. That closure failure is caused by the type and quantity of dislocations piercing the enclosed surface.

As due to the in-plane homogeneity of the bi-crystal interfaces only variations in the direction perpendicular to that interface are considered, in this particular case, Nye's tensor can be written as a function of the interface normal  $n_0^b$  and the gradient of  $F_p$  between the core and the bi-crystal (cf. Fig. 2.3)

$$\Lambda = - \left( n_0^b \times \frac{\Delta F_p^T}{l} \right)^T, \quad \Delta F_p = F_p^{b,i} - F_p^c, \quad (2.34)$$

with  $l$  a length parameter representing the width of the intercrystal dislocation dominated transition zone.

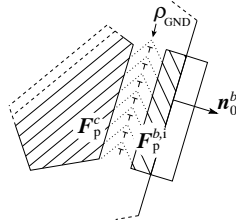


**Figure 2.3** / Between the single crystal core and each bi-crystal boundary, GND densities ( $\rho_{\text{GND}}$ ) are necessary to maintain the crystallographic lattice compatible.

The parameter  $l$  is geometrically related to the core volume fraction  $\vartheta$  of Eq. (2.27) and to the grain diameter  $d$ . Suppose each grain is, for the moment, represented by a sphere with diameter  $d$ . The centre of the sphere is occupied by the core volume fraction  $\vartheta$ .

According to Eq. (2.27), the volume of the shell surrounding the core is attributed to the bi-crystals. The thickness of that shell represents the grain boundary region

$$l = \left(1 - \sqrt[3]{\vartheta}\right) \frac{d}{2}. \quad (2.35)$$

Note that this relation also holds for cubical grain representations.

It is assumed that this region stores the geometrically necessary dislocations, i.e. the variation of  $F_p$  is accommodated in this region only. At a constant  $\vartheta$ ,  $l$  varies proportional to the grain size. The GND's are then stored in an increased volume for larger grains, which will lower the free energy of the grain. Other choices in this respect are varying  $\vartheta$  as a function of  $d$  while keeping  $l$  fixed or a more sophisticated ansatz incorporating the deformation history. However, there are no clear physical arguments to support these choices. Furthermore, it turns out that these alternative choices do not show a Hall-Petch-like behaviour as well as the adverted approach with a constant core fraction.

Once Nye's tensor has been computed, the related dislocation densities are determined by representing Nye's tensor as the cumulative contribution of all 18 (12 edge and 6 screw, cf. Kubin et al. (1992)) types of GND densities  $\rho_{\text{GND}}^\xi$  ( $\xi = 1, 2, \dots, 18$ ) following the approach of Arsenlis and Parks (1999)

$$\Lambda_0 = \sum_{\xi} \rho_{\text{GND}}^\xi \mathbf{b}_0^\xi \mathbf{t}_0^\xi, \quad (2.36)$$

where  $\mathbf{b}_0^\xi$  and  $\mathbf{t}_0^\xi$  are the (initial) Burger's and tangent vector of each dislocation type  $\xi$ , respectively. Because of the fact that Nye's tensor only has 9 independent components, various combinations of dislocation densities may compose the incompatibility of plastic deformation between the core and the boundary. Without knowledge of the crystallographic dislocation density evolution or additional constraints, it is impossible to determine the exact dislocation structure. Two procedures have been proposed by Arsenlis and Parks (1999) to find a lower bound of GND densities accommodating a given Nye tensor. The approach of minimizing the sum of the squares of the dislocation densities is favoured over the minimization of the total dislocation line length.

The motion of gliding dislocations on a slip plane is obstructed by forest dislocations piercing that slip plane. The GND's contribute to this crystalline strengthening by creating additional pile-ups and by augmenting the forest dislocation density. The strengths and densities of those obstacles depend on the dislocation densities in all directions and their mutual interactions. Through a set of interaction coefficients  $A^{\alpha\xi}$  and the dislocation density magnitude  $|\rho_{\text{GND}}^\xi|$ , the *effective* density of point obstacles to mobile dislocation motion on slip system  $\alpha$  can be determined, as proposed by Franciosi and Zaoui (1982) (as the dislocation profile on the slip systems is unknown,

the interaction coefficients are solely based on the dislocation Burger's vectors). The enhanced slip system strength  $s_{\text{GND}}^\alpha$  is related to the square root of that effective density following Ashby (1970)

$$s_{\text{GND}}^\alpha = c\mu b \sqrt{\sum_{\xi} A^{\alpha\xi} |\rho_{\text{GND}}^\xi|}, \quad (2.37)$$

where  $c$  is a constant,  $\mu$  is the shear modulus and  $b$  is the length of the Burger's vector.

Information on the densities of SSD's is only implicitly available through the slip system strength  $s_{\text{SSD}}^\alpha$ . Hence, individual densities of SSD's, for the 18 dislocation types, is not possible. This makes a direct addition of the densities of SSD's and GND's in an explicit fashion quite ambiguous. Alternatively, the overall slip strength  $s^\alpha$  is taken as a coupling between the corresponding contributions of both dislocation types

$$s^\alpha = \left( (s_{\text{SSD}}^\alpha)^p + (s_{\text{GND}}^\alpha)^p \right)^{\frac{1}{p}}, \quad (2.38)$$

where  $p = 1$  represents a straightforward addition of both strengths and  $p = 2$  implies summing the attributive dislocation densities in an *effective* way. In this chapter, both choices are reviewed.

## 2.5 Numerical results

The presented model, including enhanced work hardening by GND's, has been implemented in order to simulate the stress-strain behaviour of a FCC polycrystal composition during uniaxial tension for different grain sizes. The grain size dependence of the flow stress, also known as the Hall-Petch effect (cf. Eq. (2.1)), in this context is treated as the result of the increase of GND densities for maintaining lattice compatibility with decreasing grain sizes (Ashby, 1970). Consequently, small grained polycrystalline materials exhibit more resistance to an applied deformation than larger grained ones.

The computations are compared to numerical and experimental results found in literature. First, the constitutive response is confronted with detailed finite element computations on polycrystalline copper by Arsenlis and Parks (2000). The finite element mesh used by Arsenlis and Parks, consisting of 27 randomly-oriented cubic grains, is transformed into a morphologically similar material point representation, using 27 single crystals, having similar lattice orientations and being arranged in the same spatial directions, with 54 bi-crystals. This representation is (partly) depicted in Fig. 2.4. In both simulations, uniaxial tension is applied in the  $z$ -direction. The strain rate is fixed at  $0.001 \text{ s}^{-1}$ .

For copper, many contradictory experimental results exist, in which quite often the Hall-Petch relation fails as a result of the intersection of stress-strain curves of fine grained copper with the stress-strain curves of coarse grained copper. This effect is often attributed to texture developments. Therefore, the experimental findings of Hansen (1979)

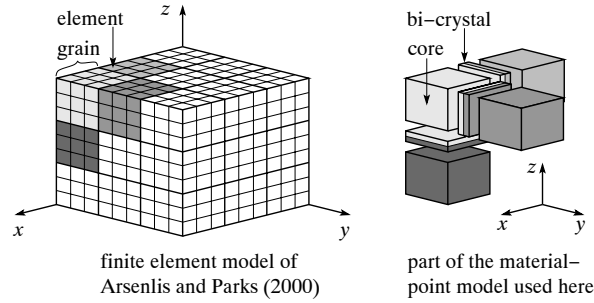


**Figure 2.4** / The finite element mesh of the polycrystal composition under consideration is transformed into a similar material point representation, consisting of 27 single crystals and 54 bi-crystals.

have been chosen for comparison with the simulations. In that work, parallel stress-strain curves are determined, which is achieved by preparing large-grained specimens by reducing the amount of deformation prior to recrystallization. Moreover, the ratio between the specimen diameter and the grain size was taken to be larger than 15 to minimize the effect of surface grains. Hansen performed tensile tests on polycrystalline copper strips with average in-plane grain diameters of 14, 33 and 220  $\mu\text{m}$ .

In the simulation, the diameter ( $d$  in Eq. (2.1)) is varied similar to the experiments (14, 33 and 220  $\mu\text{m}$ ), whereas the crystallographic orientations are left identical. The core volume fraction is set constant to  $\vartheta = 0.5$  (Evers et al., 2000). The initial internal bi-crystal fractions are taken according to  $f_0^{b,i} = f_0^{b,e} = 0.5$  for each bi-crystal “ $b$ ”. The constitutive parameters are given in Table 2.1.

The dislocation interaction coefficients of the matrix  $A^{\alpha\xi}$  depend on the interaction types between dislocations on different slip systems, as documented by Franciosi and Zaoui (1982). They classify those interactions according to whether the dislocations belong to the same slip system (self hardening, interaction coefficient  $a_0$ ), belong to coplanar slip systems or form Hirth locks (interaction coefficient  $a_1$ ), form glissile junctions (interaction coefficient  $a_2$ ) or Lomer-Cottrell locks (interaction coefficient  $a_3$ ), with  $a_0 \leq a_1 \leq a_2 \leq a_3$ . Finally, the initial density of GND’s is taken to be zero on all slip systems and in all bi-crystals of the material point.

In the numerical procedure, the stresses in the single crystal interiors and in each half of all bi-crystals are computed independently. Successively, the stress of each of the 27 grain compositions ( $\sigma^k$ ) is determined by evaluation of Eq. (2.27), and conventional Taylor averaging of all compositions by Eq. (2.28) (since, in this example, all grains are equally sized) yields the macroscopic stress in the material point,  $\bar{\sigma}$ , which is evaluated next.

**Table 2.1** / Constitutive parameters of copper (Dai, 1997; Arsenlis and Parks, 2000); the parameter  $c$  is determined in this analysis; the coefficients  $a_0$ ,  $a_1$ ,  $a_2$  and  $a_3$  are entries in the dislocation interaction matrix  $A^{\alpha\xi}$ , which is documented by Franciosi and Zaoui (1982) and quantified for copper by Cuitiño and Ortiz (1992).

Parameter		Magnitude	Used in Eq.
Young's modulus	$E$	144	GPa (2.6)
Poisson's ratio	$\nu$	0.33	– (2.6)
Reference plastic strain rate	$\dot{\gamma}_0$	0.001	$s^{-1}$ (2.7) (2.22)
Strain rate sensitivity	$m$	0.012	– (2.7) (2.22)
Initial slip resistance	$\tau_0$	8	MPa (2.10)
Latent hardening ratio	$q$	1.4	– (2.11) (in $q^{\alpha\beta}$ )
Hardening parameter	$h_0$	250	MPa (2.12)
Saturation value	$s_\infty$	190	MPa (2.12)
Hardening rate exponent	$a$	2.5	– (2.12)
Adjustable parameter	$c$	0.3 <sup>a</sup> and 0.7 <sup>b</sup>	– (2.37)
Shear modulus	$\mu$	41.5	GPa (2.37)
Burger's vector length	$b$	0.25	nm (2.37)
GND interaction coefficient	$a_0$	0.06	– (2.37) (in $A^{\alpha\xi}$ )
GND interaction coefficient	$a_1/a_0$	5.7	– (2.37) (in $A^{\alpha\xi}$ )
GND interaction coefficient	$a_2/a_0$	10.2	– (2.37) (in $A^{\alpha\xi}$ )
GND interaction coefficient	$a_3/a_0$	16.6	– (2.37) (in $A^{\alpha\xi}$ )

<sup>a</sup>combined with  $p = 1$  in Eq. (2.38)

<sup>b</sup>combined with  $p = 2$  in Eq. (2.38)

In the evaluation, two options are examined. First, the contributions of the SSD and GND densities are combined by linear addition of their corresponding slip system strengths,  $s_{SSD}^\alpha$  and  $s_{GND}^\alpha$  in Eq. (2.38), respectively. Second, following the finite element simulations of Arsenlis and Parks, the choice of *effectively* adding SSD and GND *densities* is regarded, which is reflected by setting  $p = 2$  in Eq. (2.38). This can be stated when conferring the relation between strength and dislocation density in Eq. (2.37), which is also implicitly assumed for the case of SSD's, where the relation at issue actually originates from. Correspondence to the experiments (Hansen, 1979) could be achieved by the adjustment of a single parameter ( $c$  in Eq. (2.37)) in either case of dislocation strength or density addition.



### 2.5.1 Stress-strain behaviour

The simulated and experimentally determined uniaxial stress-strain curves are given in Fig. 2.5a and 2.5b. In both figures, no considerable grain size effect is predicted at the onset of yielding, which is not in line with experimental findings in general. This observation is attributed to the numerical assumption that no initial GND densities are present in the material, which contradicts with reality, as during the processing of the polycrystalline material, certain amounts of GND densities are introduced (i.e. next to the GND's comprising the grain boundaries themselves). Furthermore, from the figures, it can be concluded that both the detailed simulations of Arsenlis and Parks and the simulations encompassing the summation of the dislocation densities show an almost perfect agreement with the experimentally observed grain size dependent behaviour, whereas the simulations encompassing the dislocation strength addition show a small deviation for the large grained specimen. Nevertheless, the intragranular inhomogeneities between the core and the bi-crystals as effectuated by the adapted Taylor assumption bring about a similar effect as the inhomogeneity between the finite elements of the two regions in the case of the discretized grains when, for both cases, the enhanced hardening approach is applied. Therefore, the presented advanced polycrystal model appears to be an adequate alternative for the fully discretized finite element simulations for applications where the (macroscopic) length scale at issue is large with respect to the size of the individual grains (i.e. when such a polycrystal approach is valid).

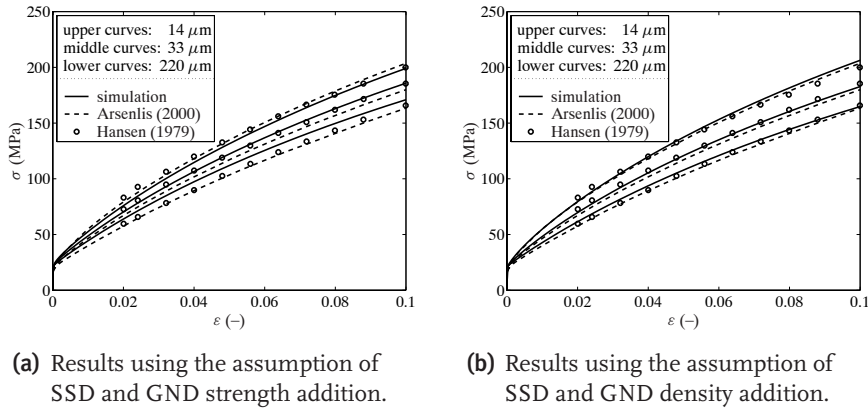


**Figure 2.5** / Uniaxial stress versus uniaxial strain for average grain diameters of 14, 33 and 220  $\mu\text{m}$ , represented by the upper, middle and lower curves (of each type), respectively. The dashed lines represent results from finite element calculations (Arsenlis and Parks, 2000) and the bullets are experimental results (Hansen, 1979).

### 2.5.2 Hall-Petch parameters

The magnitude of  $\sigma_0(\varepsilon)$  in the Hall-Petch equation (2.1) can be recovered by performing an additional simulation. In that simulation, by excluding  $s_{\text{GND}}^\alpha$  from Eq. (2.38), virtually, grains of infinite dimension are modelled and  $\sigma_0(\varepsilon)$  is determined.

The two remaining Hall-Petch parameters, i.e. the Hall-Petch slope  $k$  and the exponent  $n$  (cf. Eq. (2.1)) are determined in such a way that the total accumulated difference between the simulated stress-strain curves and the curves following from the Hall-Petch relation is minimized in a least squares sense. For this, it is assumed that  $n$  is a constant and that  $k$  may vary as a function of the strain  $\varepsilon$ . This strain domain is discretized, using  $N$  supporting values  $\varepsilon^i (i = 1, 2, \dots, N)$ , and at each point  $\varepsilon^i$ , the difference between the stress  $\sigma_{\text{HP}}^i$  according to Eq. (2.1) and the simulated uniaxial stress  $\sigma^i$ , is computed.

$$\min_{\{n, k^i\}} \left\{ \sum_{j=1}^3 \sum_{i=1}^N \frac{(\sigma_{\text{HP}}^i(d^j) - \sigma^i(d^j))^2}{(\sigma^i(d^j))^2} \right\}^{\frac{1}{2}}. \quad (2.39)$$

Accordingly,  $N$  values of the Hall-Petch slope  $k^i$  as well as the constant  $n$ , which together with  $\sigma_0^i$  and the fixed diameters  $d^j$  (14, 33 and 220  $\mu\text{m}$ ) basically determine  $\sigma_{\text{HP}}^i(d^j)$ , are simultaneously quantified through the minimization.

For the cases of dislocation strength addition versus dislocation density addition, the resulting  $n$  reads 0.50 and 0.94, respectively. These values originate from the way in which the geometric effects are incorporated into the slip system resistance (and, correspondingly, the flow stress), i.e. the incorporation of  $s_{\text{GND}}^\alpha$  in  $s^\alpha$  according to Eq. (2.38). The reason behind this is the intrinsic diameter dependence of  $s_{\text{GND}}^\alpha$  through Eqs. (2.34)–(2.37). Through these –one could say physically based– equations, the influence of the diameter on the constitutive behaviour is retrieved. Furthermore, Arsenlis and Parks determined  $n$  to be in the range of 0.88 to 0.93 in their simulations incorporating dislocation density addition.

In Figs. 2.6a and 2.6b, for the assumptions of SSD and GND strength addition and density addition, respectively, the agreement of the Hall-Petch relation using the corresponding computed Hall-Petch parameters with the simulated stress-strain curves is shown. In both cases, the Hall-Petch relation is perfectly suited to describe the grain size dependent response.

For comparison, the Hall-Petch parameters based on the experimental results by Hansen also have been computed. After minimization of expression (2.39), the Hall-Petch exponent is determined to be 0.80. Based hereon, the stress-strain curves are constructed for all diameters such as they are predicted by the Hall-Petch relation. These curves are compared to the experimental data in Fig. 2.7.

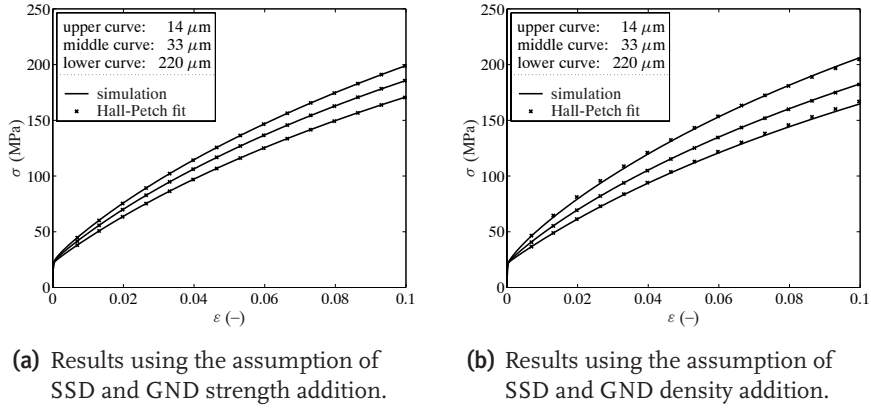


**Figure 2.6** / Simulated stress-strain curves of all diameters (solid lines) and the Hall-Petch fits (cf. the marks) to that data, where the Hall-Petch parameters  $n$  and  $k(\varepsilon)$  are determined through minimization of (2.39).

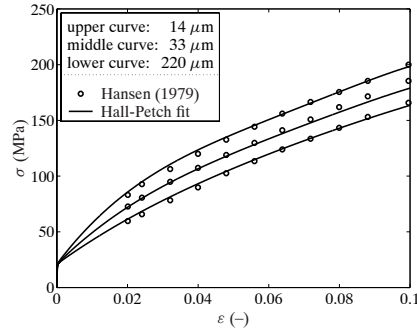


**Figure 2.7** / Comparison of the experimental data of Hansen (cf. the marks) to the curves which are computed by applying the computed parameters  $n$  and  $k(\varepsilon)$  to the Hall-Petch relation for all diameters (solid lines).

From the present analysis, it can be concluded that the determination of the actual Hall-Petch exponent  $n$  is very sensitive to minor changes in the material response. This also explains why various values of the exponent can be found in literature for the same material, but possibly with minor changes in their processing history. The best correspondence with the particular experimental findings of Hansen is achieved using the assumption of summing the SSD and GND *densities* ( $p = 2$  in Eq. (2.38), cf. Fig. 2.5).

## 2.6 Conclusions

A local plastic strain gradient-dependent crystal plasticity model has been developed, describing the grain size dependent behaviour of a polycrystal material (i.e. an aggregate of grains is considered attributed to a material point). Intragranular incompatible deformations, which arise as a result of the consideration of grain boundaries (represented by bi-crystals), are used to determine the amount of additional –geometrically necessary– dislocations. The density of these dislocations determines the amount of enhanced hardening through the formation of additional obstacles, obstructing the propagation of slip.

As the intragranular heterogeneous deformation is intrinsically related to the grain size, so is the magnitude of the enhanced hardening term. Furthermore, the conventional slip system hardening by the statistically-stored dislocations is described by a system of phenomenological equations, covering the effects of both self and latent hardening. Both SSD and GND slip resistances are combined in two different ways, one in which they are simply summed and one in which, implicitly, their accompanying forest dislocation densities are added.

Both approaches of the presented local polycrystal material model have been compared to full-scale finite element simulations considering the addition of dislocation densities and, moreover, to experimentally determined tensile curves dealing with several (average) grain sizes. For these simulations, an analogous representation of the finite element mesh with respect to crystallographic and morphological orientations has been applied in the polycrystal material point representation. The resulting grain size dependent tensile curves, as computed by the enhanced Taylor approach at hand, agree well with the finite element computations and with the experimental data. The agreement is almost perfect for the case of dislocation density addition and good for the case of dislocation strength addition. Therefore, the polycrystalline crystal plasticity model is found to be a worthy substitute for the full-scale finite element model from a computational point of view.

It has been shown that the applied model is well suited to describe the grain size effect in a physically interpretable manner (i.e. without explicitly introducing grain size dependence in a flow stress relation). Moreover, additionally, the morphological texture can be incorporated through the orientation of the grain boundaries and their mutual weight (Evers et al., 2000). Therefore, it is believed to be one of the most sophisticated models available nowadays at the polycrystal level.

The present model focused on the elaboration of a polycrystalline model that includes a physically based dependence on the grain size. In order to make well founded choices concerning the combination of several dislocation types, a crystal plasticity formulation which is completely based on dislocation densities should yet be developed. This gives also the opportunity to consider substructuring inside the grains, which is believed to dominate strain hardening at intermediate strains.



## CHAPTER THREE

# Single crystal model application to constrained simple shear<sup>1</sup>

---

**Abstract /** A strain gradient dependent crystal plasticity approach is presented to model the constitutive behaviour of polycrystal FCC metals under large plastic deformation. In order to be capable of predicting scale dependence, the heterogeneous deformation-induced evolution and distribution of geometrically-necessary dislocations (GND's) are incorporated into the phenomenological continuum theory of crystal plasticity. Consequently, the resulting boundary value problem accommodates, additional to the ordinary stress equilibrium condition, a condition which sets the additional nodal degrees of freedom –the edge and screw GND densities– proportional (in a weak sense) to the gradients of crystalline slip. Next to this direct coupling between microstructural dislocation evolutions and macroscopic gradients of plastic slip, another characteristic of the presented crystal plasticity model is the incorporation of the GND-effect, which leads to an essentially different constitutive behaviour than the statistically-stored dislocation (SSD) densities. The GND's, by their geometrical nature of locally similar signs, are expected to influence the plastic flow through a non-local back-stress measure, counteracting the resolved shear stress on the slip systems in the undeformed situation and providing a kinematic hardening contribution. Furthermore, the interactions between both SSD and GND densities are subject to the formation of slip system obstacle densities and accompanying hardening, accountable for slip resistance. As an example problem and without loss of generality, the model is applied to predict the formation of boundary layers and the accompanying size effect of a constrained strip under simple shear deformation, for symmetric double slip conditions.

### 3.1 Introduction

This chapter focuses on the constitutive behaviour of FCC metals under large deformation, with an explicit emphasis on a physically based incorporation of plastic strain gra-

---

<sup>1</sup>This chapter is reproduced from Evers et al. (2003a).

dient effects. Generally speaking, gradients of plastic deformation on the scale of the microstructure may arise due to any externally applied gradients of plastic slip, associated with a macroscopically imposed non-uniform deformation field. But even if the macroscopically imposed deformation field is uniform in the context of the classical continuum theory, due to the presence of grain boundaries (Becker and Panchanadeeswaran, 1995), microscopically heterogeneous deformation structures may arise. In both cases, one could speak of a non-uniform deformation at a small length scale characterising the heterogeneity of the material. For plastic deformations, this is the length scale associated with dislocation structures (Needleman and Gil Sevillano, 2003), causing the plastic flow to be size dependent, with an increasing hardening for decreasing grain or specimen sizes. Additionally, a possible mechanism for the occurrence of heterogeneous deformation is the formation of dislocation structures at large strains, which is beyond the scope of this work.

The non-uniform plastic deformations give rise to the development of so-called geometrically-necessary dislocation (GND) densities (Ashby, 1970), which are required to preserve crystallographic lattice compatibility. The more general concept of dislocations constitutes the underlying basis for the phenomenological description of single crystal plasticity, where the plastic deformation, carried by crystallographic slip on the distinct slip planes, is inherently caused by the flow of so-called statistically-stored dislocations (SSD's). Of the total dislocation density, the GND density is defined as the minimum density that is required to accommodate a given strain gradient, and the SSD density is just the remainder (see also Gao and Huang, 2003). However, the GND density can equally well be considered as the local surplus of a certain sign (i.e. positive or negative) of the total dislocation density.

Herewith, one of the two characteristics of GND's is indicated, namely they do not directly contribute to plastic straining in the way the SSD's do, but they originate as a result of spatial plastic strain variations (cases of non-zero net Burger's vector). Their second characteristic is the fact that, as a consequence of their task of accommodating lattice curvatures, within a length scale substantially larger than their spacing, they have equal orientations, which is denominated as having equal dislocation signs. Whereas the SSD's do not contribute to any spatial inhomogeneities at that length scale, their signs per definition cancel out at the continuum level and therefore are not taken into consideration.

In practice, it is impossible to identify an individual dislocation as being geometrically necessary or not, and to detect the switching of specific SSD's to GND's and vice versa. Moreover, each dislocation locally accommodates a plastic strain gradient and leads to a local lattice curvature, but the SSD and GND measures –their *densities*– are really based on the properties of a population of dislocations within a certain volume. Therefore, of all dislocations present in the material, one can define the density of both groups by their characteristics as described above and use these quantities as input parameters in

the SSD and GND density based crystal plasticity model at issue, together with their specific distinct influences on the constitutive behaviour. In such a way, the discrete atomic structure of metals is described by a continuum theory in a *homogenised* fashion without disregarding the governing physical processes at the atomic scale.

Several strain gradient models have been developed in order to capture scale size effects (e.g. Aifantis, 1987; Fleck et al., 1994; Fleck and Hutchinson, 1997; Shu and Fleck, 1999; Gao et al., 1999; Huang et al., 2000). Such approaches introduce an intrinsic material length scale in an analytical plasticity formulation, thereby enabling the prediction of e.g. particle size effects (Ashby, 1970), indenter size effects (Nix and Gao, 1998; Gao et al., 1999) and size effects under micro-torsion (Fleck et al., 1994). The underlying physics is sometimes more directly related to the generation and distribution of dislocations (Groma, 1997; Gao et al., 1999) or to the plastic or elastic incompatibilities (Dai and Parks, 1997; Dai, 1997; Steinmann, 1996; Sluys and Estrin, 2000; Acharya, 2001; Bassani, 2001; Gurtin, 2002). However, approximations and limitations are often met as two-dimensional idealisations of double slip, the consideration of global strain gradients instead of intragranular strain gradients, and the evaluation of global incompatibility measures (the curl of the elastic or plastic deformation gradient tensor) instead of slip system related ones (e.g. Acharya and Beaudoin, 2000; Acharya, 2001; Evers et al., 2002). Moreover, the GND's –or at least their influences– are superimposed on the hardening or slip resistance, disregarding their distinct physical contribution compared to SSD's. On the other hand, discrete dislocation predictions are increasingly capable of simulating scale dependent behaviour (Shu et al., 2001; Bassani et al., 2001; Bittencourt et al., 2003). The numerical benchmark analyses of simulating a constrained strip under simple shear for the case of double slip (Shu et al., 2001; Bittencourt et al., 2003), as well as similar simulations performed by Svendsen (2003), are here used to compare the present SSD and GND density based crystal plasticity model to existing theories.

Conventional homogeneous constitutive models, such as published by Bronkhorst et al. (1992) and Kalidindi et al. (1992), fail to accurately predict scale dependent behaviour. In such local continuum crystal plasticity models, no explicit attention is paid to the presence of strain gradients and no absolute length scale enters the formulations. The presence, motions, and interactions of dislocations are not explicitly recognised. Their effects are often modelled indirectly by a phenomenological flow rule and hardening evolution, for which it is implicitly assumed that the accumulation of SSD's is the (only) driving force, leaving any long-range effects unconsidered. Notwithstanding, also in such conventional local plasticity theories strain gradients arise, however, these are not considered to induce a GND population, which is the required additional assumption that leads to a size effect. In this chapter, a phenomenological theory of plastic flow (adopted from Evers et al., 2002) is extended by introducing the strain gradient related production of GND's, in order to be able to predict size dependent behaviour under global as well as intragranular strain gradients.



During the process of plastic deformation, dislocations have to overcome both short-range and long-range obstacles (Kocks et al., 1975). For FCC metals, the primary short-range barriers are other dislocations which intersect the slip plane and impede the motion of gliding dislocations. The evolution of SSD's during crystallographic slip increases the number of short-range interactions and accordingly results in isotropic hardening of the metal. Furthermore, the absolute GND densities equally well contribute to this short-range effect. The resistance to crystallographic slip due to short-range obstacles can be overcome by thermal activation, whereas effect of the long-range obstacles is essentially independent of the temperature, and can be overcome with the aid of the applied resolved shear stress (Nemat-Nasser et al., 1998). It is recognised in this work that the GND's are responsible for the long-range contribution. They originate from any macroscopically inhomogeneous plastic deformation after removal of external loads, a scale dependent effect which was first quantified by Nye (1953). A non-uniform GND distribution brings about additional residual stresses, entering the formulations through so-called back-stress contributions, counteracting the local resolved shear stress and therefore obstructing the crystallographic slip in an essentially different fashion (long-range effects provide a kinematic hardening). This fully complies with the statement of Mughrabi (2001) that a simple superposition of the GND density on the SSD density does not suffice for an accurate modelling of scale dependent behaviour. The above outlines the main differences of the presented framework compared to the modelling of length scale effects in crystal plasticity by e.g. Dai (1997), Shu and Fleck (1999), and Acharya and Beaudoin (2000). Moreover, Steinmann (1996), Gurtin (2002), and Cermelli and Gurtin (2002) also make a discrepancy of dislocation contributions to different types of hardening, based on thermodynamical considerations.

The SSD densities are governed by a differential equation, covering both the generation and annihilation of SSD's on each slip system. Annihilation events take place when dislocations of opposite sign meet if the distance between them is smaller than a certain critical value, i.e. the annihilation length (Essmann and Mughrabi, 1979). Furthermore, the strength differences of the various dislocation junctions are also taken into account (Franciosi and Zaoui, 1982). It has been shown by Tabourot et al. (1997) that the evolution law at hand, in combination with the applied hardening by short-range interactions, adequately describes the first three hardening stages of copper. On the other hand, the GND evolution is coupled –in a finite element context– to the incompatibility of the plastic deformation by an expression which relates the nodal GND densities to the appropriate gradients of crystalline slip. With knowledge of the crystalline orientation in relation to the plastic strain gradients, the type of dislocation (edge or screw) needed to maintain lattice continuity is also determined. The framework is suitable for incorporating any number or type (edge or screw) of dislocations, depending on the number of existing slip systems.

As all of the relations in the resulting framework are based on physical considerations, the corresponding material parameters have a physical meaning. The intrinsic material length scale is the most fundamental quantity characterising plastic deformation in a crystalline material, i.e. the length of the Burger's vector. One could argue that, for polycrystals, the grain size is equally well a basic –or secondary– length scale, yet the present model is intended to be used on a subgrain level, where all grains are individually discretised, and the grain boundaries are modelled as described above. This allows for the occurrence of strain gradients, the development of which depends on the grain size, the grain boundary interactions, and the lattice misfit. Therefore, that secondary length scale does not explicitly enter the model, yet it enters the simulations. In the test problem of this contribution, the height of the constrained strip serves as the secondary length scale.

The chapter is organized as follows. First, the constitutive crystal plasticity framework is presented in Section 3.2.1. In that framework, an extended slip law is introduced to enable the account for short- and long-range effects. These effects, i.e. the slip system strength and the back-stress contributions, both being input variables for the extended slip law, are determined in Section 3.2.2. This also involves a newly developed derivation of the particular back-stress relations, which is considered in more detail. Subsequently, the relations for determining the necessary (edge) SSD's and (edge and screw) GND's are presented in Section 3.2.3. Next, the finite element formulation of the entire framework is outlined in Section 3.3. Until that point, all formulations are suitable for FCC metals with 12 slip systems in a 3D setting. Finally, in Section 3.4, the FEM implementation is applied to simulate the mechanical behaviour of a constrained strip under plane strain simple shear, an example problem for which the model is reduced to a two slip system configuration. For this particular example, comparison with published results is possible.

## 3.2 Constitutive framework

### 3.2.1 Fundamentals

The kinematics adopted in this chapter is commonly used in the field of crystal plasticity. The basic feature is the distinction between two physical mechanisms, represented by the multiplicative decomposition of the deformation gradient tensor into an elastic and a plastic part (Lee, 1969)

$$F = F_e \cdot F_p, \quad (3.1)$$

where  $F_e$  comprises the small lattice deformation and a possibly large rigid body rotation of the intermediate configuration (Mandel, 1974), which is applied to arrive at the deformed configuration. The intermediate (or relaxed) configuration results from the

isochoric and externally stress-free deformation of the reference configuration by  $F_p$ . It is assumed that the latter part results solely from continuous plastic shearing (driven and obstructed by dislocations) on well-defined slip planes in well-defined slip directions. For FCC metals, 12 favourable (octahedral) systems can be characterised by the Miller indices  $\{111\}\langle 110\rangle$ , where each system  $\alpha$  ( $\alpha = 1, 2, \dots, 12$ ) is represented in the reference configuration by the two time-independent orthonormal vectors  $m_0^\alpha$  and  $n_0^\alpha$ , the slip direction and slip plane normal, respectively. Now, the evolution of the macroscopic plastic deformation can –by definition– be expressed as the superposition of all crystallographic slip rates  $\dot{\gamma}^\alpha$  (Rice, 1971)

$$\dot{F}_p = L_p \cdot F_p, \quad L_p = \sum_{\alpha} \dot{\gamma}^\alpha P_0^\alpha, \quad P_0^\alpha \equiv m_0^\alpha n_0^\alpha, \quad (3.2)$$

where  $L_p$  is the plastic velocity gradient tensor and  $P_0^\alpha$  is known as the non-symmetric Schmid tensor.

With respect to the intermediate configuration, the elastic second Piola-Kirchhoff stress measure  $\tau \equiv \det(F_e) F_e^{-1} \cdot \sigma \cdot F_e^{-T}$  is taken to be related to its work conjugated elastic Green strain measure  $E_e$  through

$$\tau = {}^4C : E_e, \quad E_e \equiv \frac{1}{2} (C_e - I), \quad C_e \equiv F_e^T \cdot F_e, \quad (3.3)$$

where  $\sigma$  is the Cauchy stress tensor,  $C_e$  is the elastic right Cauchy-Green tensor and  $I$  is the second-order unit tensor. The fourth-order isotropic elasticity tensor  ${}^4C$  is defined by Young's modulus  $E$  and Poisson's ratio  $\nu$ . For further details regarding the constitutive setting, the reader is referred to Evers et al. (2002).

The fundamental connection between the single crystal basis and the underlying dislocation density development is realized by relating the plastic shearing rate  $\dot{\gamma}^\alpha$  of each slip system to the corresponding ‘‘effective’’ shear stress  $\tau_{\text{eff}}^\alpha$  and the actual deformation resistance  $s^\alpha$  through a viscoplastic power law (Hutchinson, 1976; Peirce et al., 1982) which has been reformulated in consideration of the contribution by Nemat-Nasser et al. (1998)

$$\dot{\gamma}^\alpha = \dot{\gamma}_0 \left( \frac{|\tau_{\text{eff}}^\alpha|}{s^\alpha} \right)^{\frac{1}{m}} \exp \left\{ -\frac{\Delta G^\alpha}{kT} \right\} \text{sign}(\tau_{\text{eff}}^\alpha), \quad (3.4)$$

where  $\dot{\gamma}_0$  and  $m$  are material parameters representing the reference plastic strain rate and the rate sensitivity exponent of the original power law function, respectively. Employing small values of  $m$  implies an almost purely plastic behaviour, where  $\dot{\gamma}^\alpha$  remains negligible unless  $\tau_{\text{eff}}^\alpha$  is close to  $s^\alpha$ . The extension of the powerlaw by the exponential multiplier, varying in the range of 0 to 1, characterises the thermally-induced dislocation motion. Moreover, it is expected to effectuate an improved description of low temperature

behaviour (Harder, 1999). In that exponential multiplier,  $k$  is Boltzmann's constant and  $T$  is the absolute temperature. The activation energy  $\Delta G^\alpha$  is given by (see also Kocks et al., 1975; Kocks, 2001)

$$\Delta G^\alpha = G_0 \left( 1 - \frac{|\tau_{\text{eff}}^\alpha|}{s^\alpha} \right). \quad (3.5)$$

Here, the threshold shear stress, required by a dislocation to pass a barrier without any assistance from thermal activation, is represented by the slip system strength  $s^\alpha$ . Furthermore,  $G_0$  is the total free energy needed to overcome the barrier without the aid of external work, here regarded to be a constant. The accompanying shape of the energy-barrier profile for this process can also be included in this formulation but remains unconsidered here.

The resolved effective stress  $\tau_{\text{eff}}^\alpha$  is regarded to be the driving force behind the movement of dislocations on slip system  $\alpha$ . It is defined as the difference between the resolved shear stress  $\tau^\alpha$  (also known as ‘‘Schmid stress’’) and the resolved back-stress  $\tau_b^\alpha$

$$\tau_{\text{eff}}^\alpha = \tau^\alpha - \tau_b^\alpha, \quad (3.6)$$

which are taken as the projections of the macroscopic stress tensor  $\boldsymbol{\tau}$  (Asaro and Rice, 1977; Bronkhorst et al., 1992) and the back-stress tensor  $\boldsymbol{\tau}_b$  (Harder, 1999) on slip system  $\alpha$ , respectively

$$\tau^\alpha \equiv \boldsymbol{\tau} : \boldsymbol{P}_0^\alpha \quad (3.7)$$

$$\tau_b^\alpha \equiv \boldsymbol{\tau}_b : \boldsymbol{P}_0^\alpha. \quad (3.8)$$

The above leaves the slip system strengths and the back-stress tensor unspecified. As already mentioned in the introduction, the back-stress  $\tau_b^\alpha$  (i.e.  $\boldsymbol{\tau}_b$ ) should include the influence of long-range stresses that are caused by GND density variations, whereas the remaining variables, the slip resistances  $s^\alpha$ , are a measure for the impeding of dislocation movement by the formation of short-range interactions between all dislocations, i.e. both SSD's and GND's. The most obvious difference with respect to e.g. the model of Harder, is the consideration of geometrically induced GND densities in the back-stress formulation, instead of using a phenomenological evolution law. It is believed that it is essential to properly incorporate the geometric characteristics and effects of the GND's in the back-stress relations, as motivated by the experimentally observed strain gradient dependence. Note that these geometrical considerations are not applicable to the SSD's, as their density implies both positive and negative dislocations, with a length scale of variation considerably smaller and therefore having no net impact on a resulting stress. The precise determination of these variables as a function of the dislocation densities is discussed in the next subsection.

For a certain deformation state, the macroscopic stress depends on that state modulo the plastic part (Eqs. (3.1) and (3.3)). This plastic part is coupled to the slip rates through Eq. (3.2), where the slip rates are again coupled to the macroscopic stress through Eqs. (3.4), (3.6) and (3.8), as well as to the GND density variations through  $\tau_0^\alpha$ , and to the SSD and GND densities through  $s^\alpha$  (Section 3.2.2). As discussed in Section 3.2.3, the GND densities are coupled to the crystallographic slip distribution, and the SSD density rates are coupled to the slip rates and the absolute SSD densities. Therefore, the evolution of stress, strain, and deformation state with the deformation history are strongly coupled. This entire framework is solved implicitly (combined with time integrations of the rate formulations in Eqs. (3.4) and (3.17) by use of the trapezoidal scheme), partly on the integration point level and partly on the finite element (subgrain) level, as will be outlined in Section 3.3.

### 3.2.2 Dislocation interactions

In this subsection, it is assumed that the SSD and GND densities, as well as the spatial distribution of the latter, are known. The precise determination is addressed in Section 3.2.3. Moreover, it is implicitly assumed that all SSD densities are of the edge-type, whereas for the GND densities, both edge- and screw-types are evaluated. No dislocations of a mixed-type are considered. This implies that for an FCC metal, 12 edge SSD densities are taken into account, next to 12 edge and 6 screw GND densities (Kubin et al., 1992). Each screw dislocation is permitted to move on either of the two slip planes in which it can reside. More generally, the total GND distribution may be considered to be composed of two populations. The screw densities represent the fraction of the population that may cross-slip, while the edge densities represent the fraction of the population that cannot cross-slip (Arsenlis and Parks, 2002). A complete listing of the different dislocation densities, including their type, orientation, and corresponding slip system, is given in Table 3.1.

Dislocations travel in the slip direction  $m_0^\alpha$  in order to carry the crystallographic slip. Furthermore, if the dislocation line direction is parallel to  $p_0^\alpha$  (where  $p_0^\alpha = m_0^\alpha \times n_0^\alpha$ ), the dislocation is called pure edge, and if it is parallel to  $m_0^\alpha$ , the dislocation is pure screw. In both cases, the Burger's vector is directed parallel to  $m_0^\alpha$ , where the case whether or not this is in the same or in the opposite direction defines the sign of that dislocation to be positive or negative, respectively. This corresponds to the Burger's circuit around the dislocation in the deformed situation to be drawn in the direction clockwise along the dislocation line direction, and the Burger's vector closing this circuit directed from the starting point to the end point.

**Table 3.1** / List of indices and vectors for dislocation densities and slip systems used in the simulation of FCC metals; the Schmid and Boas notation is discussed in Franciosi and Zaoui (1982);  $b$  is the length of the Burger's vector  $\mathbf{b}$ .

Dislocation density $\xi$	Slip sys- type	Slip sys- tem $\alpha$	$m$ or $\frac{\mathbf{b}}{b}$	$\mathbf{n}$	Schmid & Boas
1	edge	1	$\frac{1}{\sqrt{2}}[\bar{1}10]$	$\frac{1}{\sqrt{3}}(111)$	B5
2	edge	2	$\frac{1}{\sqrt{2}}[10\bar{1}]$	$\frac{1}{\sqrt{3}}(111)$	-B4
3	edge	3	$\frac{1}{\sqrt{2}}[0\bar{1}1]$	$\frac{1}{\sqrt{3}}(111)$	B2
4	edge	4	$\frac{1}{\sqrt{2}}[\bar{1}\bar{1}0]$	$\frac{1}{\sqrt{3}}(1\bar{1}\bar{1})$	A6
5	edge	5	$\frac{1}{\sqrt{2}}[101]$	$\frac{1}{\sqrt{3}}(1\bar{1}\bar{1})$	-A3
6	edge	6	$\frac{1}{\sqrt{2}}[01\bar{1}]$	$\frac{1}{\sqrt{3}}(1\bar{1}\bar{1})$	A2
7	edge	7	$\frac{1}{\sqrt{2}}[110]$	$\frac{1}{\sqrt{3}}(\bar{1}\bar{1}\bar{1})$	-D6
8	edge	8	$\frac{1}{\sqrt{2}}[\bar{1}01]$	$\frac{1}{\sqrt{3}}(\bar{1}\bar{1}\bar{1})$	-D4
9	edge	9	$\frac{1}{\sqrt{2}}[0\bar{1}\bar{1}]$	$\frac{1}{\sqrt{3}}(\bar{1}\bar{1}\bar{1})$	D1
10	edge	10	$\frac{1}{\sqrt{2}}[1\bar{1}0]$	$\frac{1}{\sqrt{3}}(\bar{1}\bar{1}\bar{1})$	-C5
11	edge	11	$\frac{1}{\sqrt{2}}[\bar{1}0\bar{1}]$	$\frac{1}{\sqrt{3}}(\bar{1}\bar{1}\bar{1})$	-C3
12	edge	12	$\frac{1}{\sqrt{2}}[011]$	$\frac{1}{\sqrt{3}}(\bar{1}\bar{1}\bar{1})$	C1
13	screw	-	$\frac{1}{\sqrt{2}}[110]$	$\frac{1}{\sqrt{3}}(1\bar{1}\bar{1})$ or $\frac{1}{\sqrt{3}}(\bar{1}\bar{1}\bar{1})$	-A6 or -D6
14	screw	-	$\frac{1}{\sqrt{2}}[101]$	$\frac{1}{\sqrt{3}}(1\bar{1}\bar{1})$ or $\frac{1}{\sqrt{3}}(\bar{1}\bar{1}\bar{1})$	-A3 or C3
15	screw	-	$\frac{1}{\sqrt{2}}[011]$	$\frac{1}{\sqrt{3}}(\bar{1}\bar{1}\bar{1})$ or $\frac{1}{\sqrt{3}}(\bar{1}\bar{1}\bar{1})$	-D1 or C1
16	screw	-	$\frac{1}{\sqrt{2}}[\bar{1}10]$	$\frac{1}{\sqrt{3}}(111)$ or $\frac{1}{\sqrt{3}}(\bar{1}\bar{1}\bar{1})$	B5 or C5
17	screw	-	$\frac{1}{\sqrt{2}}[10\bar{1}]$	$\frac{1}{\sqrt{3}}(111)$ or $\frac{1}{\sqrt{3}}(\bar{1}\bar{1}\bar{1})$	-B4 or D4
18	screw	-	$\frac{1}{\sqrt{2}}[0\bar{1}1]$	$\frac{1}{\sqrt{3}}(111)$ or $\frac{1}{\sqrt{3}}(1\bar{1}\bar{1})$	B2 or -A2

### Short-range effect

In contrast to many “conventional” crystal plasticity models, which relate the slip resistance to the history of plastic shear on all slip systems in a quite phenomenological fashion, here, the movement of mobile dislocations on slip system  $\alpha$  is impeded by point obstacles, the strength and density of which are determined by the type and number of short-range interactions that might occur between dislocations of coplanar or intersecting slip systems. Both the SSD and GND dislocations (on all slip systems) are considered to participate in this process of mutual interactions, and for the determination of the effective density of obstacles through a set of interaction coefficients, both their (absolute) densities are added. The classification of the experimentally determined entries of the interaction matrix  $A^{\alpha\xi}$  was performed by Franciosi and Zaoui (1982), who distinguish between dislocations belonging to the same slip system (interaction coefficient  $a_0$ ), fail to form junctions (interaction coefficient  $a_1$ ), form Hirth Locks (interaction coefficient  $a_1$ ),

co-planar junctions (interaction coefficient  $a_1$ ), glissile junctions (interaction coefficient  $a_2$ ), or sessile Lomer-Cottrell locks (interaction coefficient  $a_3$ ), with  $a_0 \leq a_1 \leq a_2 \leq a_3$ . The slip system strength  $s^\alpha$  is proportional to the square root of the effective obstacle density following Ashby (1970)

$$s^\alpha = c\mu b \sqrt{\sum_{\xi} A^{\alpha\xi} \left| \rho_{\text{SSD}}^{\xi} \right| + \sum_{\xi} A^{\alpha\xi} \left| \rho_{\text{GND}}^{\xi} \right|}, \quad (3.9)$$

where  $c$  is a constant ranging from 0.05 to 2.6 for different materials (Lavrentev, 1980),  $\mu$  is the shear modulus and  $b$  is the length of the Burger's vector. Furthermore,  $\rho_{\text{SSD}}^{\xi}$  and  $\rho_{\text{GND}}^{\xi}$  stand for the SSD density ( $\xi = 1, 2, \dots, 12$  for FCC metals) and GND density ( $\xi = 1, 2, \dots, 18$  for FCC metals), respectively. As the dislocation profiles on the slip systems are unknown, the interaction coefficients are solely based on the dislocation Burger's vectors. This especially holds for the 6 screw-type GND densities, whose slip plane is ambiguous (cf. Table 3.1).

### Long-range effect

As mentioned already in the introduction, the contribution of the GND's to the constitutive response of FCC metals is related to the spatial lattice curvature distribution and coherent stress concentrations, obstructing crystallographic slip in a way which is substantially different from the influence (cf. Section 3.2.2) of the short-range barriers to dislocation movement as induced by the densities of all dislocations (SSD's and GND's). The effect of the heterogeneity in the distribution of GND's in Eqs. (3.4–3.6) is taken into account through the back-stress tensor in Eq. (3.8), which is determined next. Together with the GND densities (cf. Section 3.2.3), the back-stress tensor is defined in the reference configuration.

First, the attention is focused on a slip system  $\alpha$  and its set of orthonormal vectors  $(\mathbf{m}_0^\alpha, \mathbf{n}_0^\alpha, \mathbf{p}_0^\alpha)$ , which serves as a base coordinate system and where the evaluation point for determining the back-stress is situated in the origin. The required stress formulas have been derived by Cottrell (1961) and are based on linearly elastic representations of edge and screw dislocations in a fictitious continuum. An individual positive edge ( $i$ ) or screw dislocation ( $j$ ) at position  $x_0$  causes a shear stress on each slip system  $\alpha$  in the evaluation point equal to

$$(\tau_e^\alpha)^i = -\frac{\mu b}{2\pi(1-\nu)} \frac{x_0^\alpha (x_0^{\alpha^2} - y_0^{\alpha^2})}{(x_0^{\alpha^2} + y_0^{\alpha^2})^2} \quad (3.10)$$

$$(\tau_s^\alpha)^j = \frac{\mu b}{2\pi} \frac{z_0^\alpha}{(z_0^{\alpha^2} + y_0^{\alpha^2})}, \quad (3.11)$$

where  $x_0^\alpha = \mathbf{m}_0^\alpha \cdot \mathbf{x}_0$ ,  $y_0^\alpha = \mathbf{n}_0^\alpha \cdot \mathbf{x}_0$ , and  $z_0^\alpha = \mathbf{p}_0^\alpha \cdot \mathbf{x}_0$ , respectively. It is assumed here and in the following, that the remote dislocations are situated on a slip system with the same lattice orientation as the slip system  $\alpha$  under consideration and, therefore, a lattice rotation between the base coordinate system and the remote dislocation orientation is disregarded. This assumption might seem contradictory to the entire motivation of the GND's as being present to account for such rotations, however the current reasoning is performed in the (imaginary) undistorted reference configuration. Both stresses decrease with increasing distance from the evaluation point and become infinite as that distance approaches zero (which is in fact never the case in reality, because a crystal is a discrete atomic structure, not a continuum).

For the understanding of the entire back-stress concept on slip system  $\alpha$ , first, consider the case of a uniform lattice curvature with respect to the undeformed configuration. In that case, the GND's are also uniformly distributed (cf. Section 3.2.3) and, consequently, the resulting long-range shear stress in a single material point as caused by the uniform field of GND's around that point completely cancels out. It is therefore not the GND *density* that contributes to a resulting long-range shear stress, but its *spatial variation* (in the reference configuration).

To quantify this dependence, a population of individual GND's within a circular region of radius  $R$  around a material point is considered to participate in the resulting long-range shear stress on slip system  $\alpha$ . The number of dislocations and their distribution within that region depends on the local dislocation density, which is approximated to be spatially linear. Herewith, it is deemed ambiguous to consider linear dislocation density variations in the dislocation line directions (i.e.  $\mathbf{p}_0^\alpha$  and  $\mathbf{m}_0^\alpha$  for edge and screw dislocations, respectively), whereas any linear variations in the normal direction  $\mathbf{n}_0^\alpha$  appear to vanish. After multiplying Eqs. (3.10) and (3.11) with this local dislocation density approximation, straightforward analytical integration over the circular area then leads to the following resulting long-range shear stress relations for (non-uniform) edge and screw dislocation density fields, respectively

$$\tau_e^\alpha = -\frac{\mu b R^2}{8(1-\nu)} \sum_{\xi} d_e^{\alpha\xi} \left( \nabla_0 \rho_{\text{GND}}^\xi \cdot \mathbf{m}_0^\alpha \right) \quad (3.12)$$

$$\tau_s^\alpha = \frac{\mu b R^2}{4} \sum_{\xi} d_s^{\alpha\xi} \left( \nabla_0 \rho_{\text{GND}}^\xi \cdot \mathbf{p}_0^\alpha \right), \quad (3.13)$$

where  $d_e^{\alpha\xi}$  and  $d_s^{\alpha\xi}$  equal  $-1$ ,  $0$ , or  $1$ , according to the way the dislocation type  $\xi$  spatially relates to the slip system  $\alpha$  (cf. Table 3.1)

$$d_e^{\alpha\xi} = \begin{cases} 1 & \text{for } \alpha = \xi = 1, 2, \dots, 12 \\ 0 & \text{for all other cases} \end{cases} \quad (3.14)$$

$$d_s^{\alpha\xi} = \begin{cases} -1 & \text{for } d_s^{(4,13)}, d_s^{(6,18)}, d_s^{(8,17)}, d_s^{(9,15)}, d_s^{(10,16)}, d_s^{(11,14)} \\ 1 & \text{for } d_s^{(1,16)}, d_s^{(2,17)}, d_s^{(3,18)}, d_s^{(5,14)}, d_s^{(7,13)}, d_s^{(12,15)} \\ 0 & \text{for all other cases.} \end{cases} \quad (3.15)$$



The only parameter which remains to be chosen is the radius of the evaluation area,  $R$ , which is considered to be a material parameter. Note that for both Eqs. (3.12) and (3.13), changing the sign of the dislocation density gradient changes the sign of the resulting stress, corresponding to either counteracting crystallographic slip or promoting. Moreover, only the resulting shear stresses are taken into consideration, apart from any normal stresses. Besides, the mutual influences of all remaining edge or screw GND's in the dislocation field are disregarded, and so are any influences of the SSD's and the dislocations on other slip systems than  $\alpha$ .

In order to account for the macroscopic cross-effect of a shear stress acting on one system to all other slip systems, the scalar values of  $\tau_e^\alpha$  and  $\tau_s^\alpha$  are exploited to compose a global back-stress tensor (Harder, 1999)

$$\tau_b = \sum_{\alpha} -(\tau_e^\alpha + \tau_s^\alpha) \left( \mathbf{P}_0^\alpha + \mathbf{P}_0^{\alpha T} \right), \quad (3.16)$$

where the minus sign is included due to the fact that, here, the resulting shear stresses of the edge and screw dislocation fields are converted to a back-stress measure, cf. Eq. (3.6). The resulting shear stresses may develop independently on all slip systems, yet, the resulting resolved back-stresses after projecting through Eq. (3.8) turn out to be dependent, i.e. the effect of a shear stress on slip system  $\alpha$  has the largest effect (one-to-one) on that same slip system and has a smaller effect on the other slip systems.

When considering again the essential starting point of this dislocation density based crystal plasticity model, i.e. Eq. (3.4), it can be concluded that both the slip resistance and the effective stress can be determined from the SSD and GND density fields. The next subsection gives an outline of the evaluation of these fields.

### 3.2.3 Dislocation density evolutions

#### SSD density

The determination of the slip system strength according to Eq. (3.9) requires the SSD density distribution as one of the input variables. As already pointed out in the introduction of the previous subsection, it is assumed that for modelling the main physical processes, the evaluation of solely *edge* SSD's suffices, the densities of which are therefore indexed by slip system indicating  $\alpha$ 's instead of the  $\xi$ 's in Eq. (3.9). For these edge SSD densities, a commonly used evolution equation is proposed

$$\dot{\rho}_{\text{SSD}}^\xi = \frac{1}{b} \left( \frac{1}{d_e^{\alpha\xi} L_\alpha} - 2y_c \rho_{\text{SSD}}^\xi \right) d_e^{\alpha\xi} |\dot{\gamma}^\alpha|, \quad \rho_{\text{SSD}}^\xi(t=0) = \rho_{\text{SSD}0}, \quad (3.17)$$

which is a generalisation of the relation originally proposed by Essmann and Mughrabi (1979). This equation is derived from the balance between accumulation and annihilation rates of dislocation densities, up to the point of saturation taking place (i.e. the point

where the average distances between the dislocations are of the same order of magnitude as the annihilation length). Note that the sign of the slip rate has no influence on the sign of the SSD density, which is considered to remain always positive.

For the annihilation rate (second term in the right-hand side of Eq. 3.17), thermal recovery is neglected because of the moderate temperature range for which this framework is fit. Instead, the annihilation is described by the dynamic recovery term in Eq. (3.17). It is assumed to be controlled by a constant  $\gamma_c$ . This material parameter represents the critical annihilation length, i.e. the average distance beneath which two dislocations of opposite sign cancel each other out spontaneously by decomposition into invisible debris (Essmann and Mughrabi, 1979). Furthermore, only annihilation between statistically-stored dislocations is considered.

The accumulation rate (first term in the right-hand side of Eq. 3.17) is linked to the average dislocation segment length of mobile dislocations (SSD's) on system  $\alpha$ ,  $L^\alpha$ , which is determined by the microstructure, i.e. the current dislocation state, through (Tabourot et al., 1997; Arsenlis and Parks, 2002)

$$L^\alpha = \frac{K}{\sqrt{\sum_{\xi} H^{\alpha\xi} |\rho_{\text{SSD}}^\xi| + \sum_{\xi} H^{\alpha\xi} |\rho_{\text{GND}}^\xi|}}. \quad (3.18)$$

Here,  $K$  is a constant and the coefficients  $H^{\alpha\xi}$  indicate the mutual immobilisation between dislocations of different slip systems. The same convention as for the coefficients  $A^{\alpha\xi}$  in Eq. (3.9) applies here, which is based on the type of interactions anticipated between the gliding SSD densities and the forest SSD and GND densities. Nevertheless, the *values* of the coefficients  $H^{\alpha\xi}$  are independent of the *values* in the strength interaction matrix  $A^{\alpha\xi}$ . In this fashion, when the forest dislocation density increases, more sections of the mobile dislocation loops may get trapped and the average length of a dislocation segment decreases.

### GND density

In order to obtain a closed set of constitutive relations, the geometrically-necessary edge and screw dislocation densities remain to be determined. These are directly and geometrically coupled to the gradients of plastic slip and are computed in the *undeformed* situation

$$\rho_{\text{GND}}^\xi = \rho_{\text{GND}_0}^\xi - \frac{1}{b} \sum_{\alpha} d_e^{\alpha\xi} (\nabla_0 \gamma^\alpha \cdot \mathbf{m}_0^\alpha) + \frac{1}{b} \sum_{\alpha} d_s^{\alpha\xi} (\nabla_0 \gamma^\alpha \cdot \mathbf{p}_0^\alpha), \quad (3.19)$$

based on the observations by Nye (1953), Kröner (1962), Ashby (1970) and the extension to three dimensions by Arsenlis and Parks (2002). In agreement with the model of Ashby, any gradient of slip in the direction normal to the glide plane ( $\mathbf{n}_0^\alpha$ ) does not result

in the formation of GND's, i.e. those gradients do not affect the lattice. The initial GND density  $\rho_{\text{GND}_0}^\xi$  will be used in future work to specify initial grain boundary dislocation (GBD) densities, without disturbing the initial plastic strain field. Here, the coefficients  $d_e^{\xi\alpha}$  and  $d_s^{\xi\alpha}$  are again given by Eqs. (3.14) and (3.15), again indicating the relations between slip systems  $\alpha$  and dislocation densities  $\xi$ , related to the specifications in Table 3.1. Each of the 6 screw dislocation densities is determined by addition of the appropriate slip gradients on *both* the glide planes in which they can reside. This is in analogy with the assumption in Section 3.2.2 that the screw dislocations are free to cross slip and their corresponding slip plane remains an ambiguous choice.

It is clear that the formulation above leads to a dislocation density with a certain polarity, depending on the direction of the plastic gradients in relation to the crystallographic orientation, all independent of the mechanism that actually *caused* the strain gradient.

### 3.3 Finite element implementation

In this section, the incorporation of the presented theoretical framework into a finite element formulation is discussed, in order to systematically compute an approximate solution of the entire set of strongly non-linear and coupled equations, for arbitrary geometries and boundary conditions. As can be seen in Eq. (3.19), the spatial variation of crystallographic slip throughout the domain is required in order to determine the GND densities. Moreover, the evolution of the crystallographic slip field is again governed by the spatial gradients of the GND densities through Eqs. (3.4), (3.6), (3.8), (3.16), (3.12), and (3.13). When, next to the deformation gradient, the GND density field is known, all relevant quantities can be determined. The GND densities are therefore chosen to be additional nodal degrees of freedom, accompanied by just as many additional state equations as given by Eq. (3.19).

In order to be able to use  $C^0$ -continuous finite elements, the differentiability requirements on the GND densities over the element boundaries have to be relaxed, as usually done for the primary nodal degrees of freedom, i.e. the displacements. Accordingly, a similar –geometrically non-linear– approach as commonly used to solve the stress equilibrium condition is adopted, which is described next.

The first Piola-Kirchhoff stress tensor  $\mathbf{T} \equiv \det(\mathbf{F}_e) \boldsymbol{\sigma} \cdot \mathbf{F}^{-\text{T}}$  is used for specifying stress equilibrium in the *undeformed* situation

$$\nabla_0 \cdot \mathbf{T}^{\text{T}} = \mathbf{0}. \quad (3.20)$$

Besides, Eq. (3.19) is generalised to

$$\rho_{\text{GND}}^\xi = \rho_{\text{GND}_0}^\xi + \mathbf{d}_0^{\xi\alpha} \cdot \nabla_0 \gamma^\alpha \quad \forall \xi, \quad (3.21)$$

in which Einstein's summation convention is used and where the indices  $d_e^{\alpha\xi}$  and  $d_s^{\alpha\xi}$ , the vectors  $\mathbf{m}_0^\alpha$  and  $\mathbf{p}_0^\alpha$ , the factor  $\frac{1}{b}$ , and the corresponding signs are all properly stored in the vectors  $\mathbf{d}_0^{\xi\alpha}$ .

In order to obtain a variational form of the governing equations given above, they are multiplied by weighting functions  $w_u$  and  $w_\rho^\xi$ , respectively, and integrated over the volume  $V_0$  of the body in its reference (undeformed) configuration. Next, the divergence theorem is applied and a Newton-Raphson iterative procedure is introduced, which provides for the iterative corrections ( $\delta T$ ,  $\delta \rho_{\text{GND}}^\xi$ , and  $\delta \gamma^\alpha$ ) to be expressed by linearised functions of the solution estimates ( $T_*$ ,  $\rho_{\text{GND},*}^\xi$ , and  $\gamma_*^\alpha$ ) of the previous iteration

$$\int_{V_0} (\nabla_0 w_u)^T : \delta T^T dV_0 = \int_{S_0} w_u \cdot t_* dS_0 - \int_{V_0} (\nabla_0 w_u)^T : T_*^T dV_0 \quad (3.22)$$

$$\begin{aligned} \int_{V_0} \left[ w_\rho^\xi \delta \rho_{\text{GND}}^\xi + (\nabla_0 w_\rho^\xi) \cdot d_0^{\xi\alpha} \delta \gamma^\alpha \right] dV_0 &= \int_{S_0} w_\rho^\xi \Gamma_{n_*}^\xi dS_0 - \dots \\ \int_{V_0} \left[ w_\rho^\xi (\rho_{\text{GND},*}^\xi - \rho_{\text{GND}_0}^\xi) + (\nabla_0 w_\rho^\xi) \cdot d_0^{\xi\alpha} \gamma_*^\alpha \right] dV_0 &\quad \forall \xi, \end{aligned} \quad (3.23)$$

where  $t_*$  is the current traction with respect to the free surface  $S_0$  and  $\Gamma_{n_*}^\xi$  is a measure for the crystallographic slip in the outward normal direction of  $S_0$ . Either these additional boundary conditions have to be specified, or the displacements and dislocation density values at  $S_0$  have to be assigned, corresponding to Neumann (natural) or Dirichlet (essential) boundary conditions, respectively.

The volume  $V_0$  of the body is now subdivided in finite elements, where the unknown fields of the nodal variables and the weighting functions within each element ( $e$ ) are approximated by their (global) nodal values multiplied by interpolation functions (stored in  $\underline{N}_u^e$  and  $\underline{N}_\rho^e$ ), following the standard Galerkin approach. The contributions of all elements (having initial volume  $V_0^e$  and boundary surface  $S_0^e$ ) are added and, taking into account that both equations must be satisfied for all admissible weighting functions, this results in a system of equations constituting the discrete force balance, completed by the discretised GND density evolution conditions

$$\sum_e \int_{V_0^e} \underline{B}_u^{eT} \delta \underline{T}_*^e dV_0^e = \sum_e \int_{S_0^e} \underline{N}_u^{eT} t_*^e dS_0^e - \sum_e \int_{V_0^e} \underline{B}_u^{eT} T_*^e dV_0^e \quad (3.24)$$

$$\begin{aligned} \sum_e \int_{V_0^e} \left[ \underline{N}_\rho^{eT} \underline{N}_\rho^e \delta \rho_{\text{GND}}^e + \underline{B}_\rho^{eT} \underline{D}^e \delta \gamma^e \right] dV_0^e &= \sum_e \int_{S_0^e} \underline{N}_\rho^{eT} \Gamma_{n_*}^e dS_0^e - \dots \\ \sum_e \int_{V_0^e} \left[ \underline{N}_\rho^{eT} \underline{N}_\rho^e (\rho_{\text{GND},*}^e - \rho_{\text{GND}_0}^e) + \underline{B}_\rho^{eT} \underline{D}^e \gamma_*^e \right] dV_0^e, \end{aligned} \quad (3.25)$$

where  $\underline{B}_u^e$  and  $\underline{B}_\rho^e$  contain the spatial derivatives of  $\underline{N}_u^e$  and  $\underline{N}_\rho^e$  in the reference configuration, respectively. Furthermore, the components and indices of  $d_0^{\xi\alpha}$  are stored per element in  $\underline{D}^e$  and the boundary terms  $t_*^e$  and  $\Gamma_{n_*}^e$  only have to be specified on element boundaries  $S_0^e$  coinciding with the surface of the body  $S_0$ .

In the system above, two quantities have not been evaluated yet, i.e. the first Piola-Kirchhoff stress tensor and the crystallographic slips. However, based on the iterative (nodal) values for the displacements  $\underline{u}_*$  and the dislocation densities  $\underline{\rho}_{\text{GND}_*}$ , their estimations  $\underline{T}_*$  and  $\underline{\gamma}_{\text{GND}_*}^e$  in the right-hand side can be computed in a straightforward manner using the constitutive relations presented in Section 3.2, whereas the iterative corrections in the left-hand side,  $\delta \underline{T}^e$  and  $\delta \underline{\gamma}^e$ , can be determined by means of consistent linearisation of that same constitutive framework

$$\delta \underline{T}^e = \underline{C}_1^e \underline{B}_u^e \delta \underline{u} + (\underline{C}_2^e \underline{N}_\rho^e + \underline{C}_3^e \underline{B}_\rho^e) \delta \underline{\rho}_{\text{GND}} \quad (3.26)$$

$$\delta \underline{\gamma}^e = \underline{C}_4^e \underline{B}_u^e \delta \underline{u} + (\underline{C}_5^e \underline{N}_\rho^e + \underline{C}_6^e \underline{B}_\rho^e) \delta \underline{\rho}_{\text{GND}}, \quad (3.27)$$

where  $\delta \underline{u}$  and  $\delta \underline{\rho}_{\text{GND}}$  are the iterative corrections for the nodal displacement and GND density values. The required time integration processes of  $\dot{\gamma}^\alpha$  in Eq. (3.4) and  $\dot{\rho}_{\text{SSD}}^\alpha$  in Eq. (3.17) can be chosen arbitrarily between fully explicit and fully implicit schemes, without disturbing the linearisation.

The entire set of discretised iterative equations to be implemented in a finite element frame can now be summarised by the following matrix representation

$$\begin{bmatrix} \underline{K}_{uu} & \underline{K}_{u\rho} \\ \underline{K}_{\rho u} & \underline{K}_{\rho\rho} \end{bmatrix} \begin{bmatrix} \delta \underline{u} \\ \delta \underline{\rho}_{\text{GND}} \end{bmatrix} = \begin{bmatrix} \underline{r}_u \\ \underline{r}_\rho \end{bmatrix}, \quad (3.28)$$

where

$$\underline{K}_{uu} = \sum_e \int_{V_0^e} \underline{B}_u^{eT} \underline{C}_1^e \underline{B}_u^e dV_0^e \quad (3.29)$$

$$\underline{K}_{u\rho} = \sum_e \int_{V_0^e} \underline{B}_u^{eT} (\underline{C}_2^e \underline{N}_\rho^e + \underline{C}_3^e \underline{B}_\rho^e) dV_0^e \quad (3.30)$$

$$\underline{K}_{\rho u} = \sum_e \int_{V_0^e} \underline{B}_\rho^{eT} \underline{D}^e \underline{C}_4^e \underline{B}_u^e dV_0^e \quad (3.31)$$

$$\underline{K}_{\rho\rho} = \sum_e \int_{V_0^e} \left[ \underline{N}_\rho^{eT} \underline{N}_\rho^e + \underline{B}_\rho^{eT} \underline{D}^e (\underline{C}_5^e \underline{N}_\rho^e + \underline{C}_6^e \underline{B}_\rho^e) \right] dV_0^e. \quad (3.32)$$

The columns  $\underline{r}_u$  and  $\underline{r}_\rho$  are equal to the right-hand sides of Eqs. (3.24) and (3.25), respectively. This system is solved by iteratively updating the nodal estimations  $\underline{u}_*$  and  $\underline{\rho}_{\text{GND}_*}$  with corrections  $\delta \underline{u}$  and  $\delta \underline{\rho}_{\text{GND}}$ , a process which is repeated until an appropriate convergence criterion is satisfied, i.e. until the right-hand side becomes sufficiently small. Note that only the first-order derivatives of the primary unknown quantities  $\underline{u}$  and  $\underline{\rho}_{\text{GND}}$  appear in the final set of equations, which indicates that their fields are only required to be piece-wise differentiable, indeed justifying the use of  $C^0$ -continuous finite elements.

### 3.4 Application

The FEM formulation as described in Section 3.3 has been implemented for plane strain conditions. For this elaboration, the full three dimensional formulation of the FCC constitutive behaviour presented in Section 3.2 remains unaltered. However, in order to further decrease the computation time and to compare the present model with non-local continuum and discrete dislocation approaches as can be found in the literature (Shu et al., 2001; Svendsen, 2003; Bittencourt et al., 2003), the application in this section is restricted to double slip and self-hardening. Following the discrete dislocation simulations by Shu et al., only edge dislocations are considered in this case. Additionally, in conformity with these contributions, the numerical analysis concerns the simple (isothermal) shear of a single crystal strip of thickness  $H$ . The plastic deformation (i.e. dislocation motion or crystallographic slip) is constrained at the upper and lower boundaries, as graphically represented in Fig. 3.1.

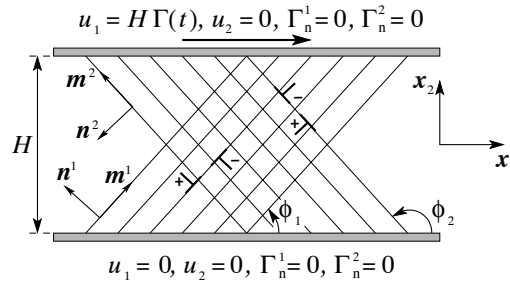


**Figure 3.1** / Geometry and boundary conditions for the simple shear deformation of a constrained strip of thickness  $H$  having two slip systems (with orientations  $\phi_1$  and  $\phi_2$  with respect to the  $x_1$ -direction); on each slip system, the corresponding edge dislocation signs are depicted.

This boundary-value problem is believed to represent the plastic constraints which are found at the grain boundaries of a polycrystal, exhibiting the key features associated with the accumulation of GND's, i.e. size effects and long-range stresses (Van der Giessen and Needleman, 2003). Furthermore, whereas the simple shear loading conditions classically admit the possibility of a homogeneous deformation field, in this particular case, due to the obstruction of plastic deformation near the walls, plastic strain gradients can develop, an effect which is locally quite similar to the case of (quasi-)homogeneous deformation of a polycrystal. Accordingly, in general, the resulting plastic flow is not uniform, as boundary layers develop in which the slip is reduced (i.e. the dislocation motion is hindered). As the thickness of the boundary layers remains more or less the same for a certain material, a size effect is expected for various strip heights  $H$ . In those boundary layers, a GND

density profile develops as a result of slip gradients, which are triggered by the micro-clamping of plastic shear in the direction normal to the walls. This boundary condition is effectuated by setting the generalised slip contribution in the interface direction,  $\Gamma_n^\xi$  in Eq. (3.23), equal to zero for both  $\xi = 1$  and  $\xi = 2$ , providing an evident physical interpretation of the non-local boundary conditions (cf. Section 3.3). Moreover, it is qualitatively similar to the obstruction of any dislocation motion through impenetrable walls at the top and bottom surface of the strip, a boundary condition which is also applied in the discrete dislocation simulations of Shu et al. (2001). The ensemble of boundary conditions is given by

$$\begin{aligned} u_1 = 0, \quad u_2 = 0, \quad \Gamma_n^1 = 0, \quad \Gamma_n^2 = 0 \quad \text{along } x_2 = 0 \\ u_1 = H \dot{\Gamma} t, \quad u_2 = 0, \quad \Gamma_n^1 = 0, \quad \Gamma_n^2 = 0 \quad \text{along } x_2 = H, \end{aligned} \quad (3.33)$$

where  $\dot{\Gamma}$  is the prescribed shear rate, taken to be  $0.001 \text{ s}^{-1}$  for this particular problem, and  $t$  is time.

Next to the plane strain conditions (no variations in the  $x_3$ -direction), the strip is supposed to be infinitely extended in the  $x_1$ -direction, modelled by means of periodic boundary conditions for both displacements and GND densities. Resultingly, in order to arrive at a sufficiently accurate description of any variations in the  $x_2$ -direction, a  $1 \times 80$  finite element mesh is used for all heights considered, with square linear elements and full integration. The mesh size has been validated not to influence the numerical results in a pathological fashion.

Simulations are performed for double slip with slip system orientations  $\phi_1 = 60^\circ$  and  $\phi_2 = 120^\circ$ , as well as for strip heights  $H$  equal to  $10^{-4.5} \text{ m}$ ,  $10^{-4.0} \text{ m}$ ,  $10^{-3} \text{ m}$ , and  $10^{-2.5} \text{ m}$  (equivalent to 0.22 mm, 0.46 mm, 1.0 mm, and 2.2 mm, respectively). Furthermore, the initial GND densities  $\rho_{\text{GND}_0}^\xi$  in Eq. (3.19) are taken to be zero and the temperature in Eq. (3.4) equals 300 K. Because of the inherent differences of the present framework with respect to non-local and discrete dislocation theories, distinct material parameters have to be adopted. As the results will be only compared in a qualitative perspective, instead of aluminium (Shu et al., 2001), the parameters in Table 3.2 are a double slip and self-hardening generalisation of the parameters best describing the constitutive response of FCC copper (12 slip systems).

First, the shear profile along the dimensionless  $x_2$ -direction is considered for a strip height equal to  $H = 0.46 \text{ mm}$  in Fig. 3.2a. In order to gain a representative picture of the actual development of the boundary layer during the deformation, the profiles are normalised with the corresponding applied macroscopic total shear ( $\Gamma = \dot{\Gamma} t$ ). Initially, the boundary layer width clearly increases with ongoing deformation, until it practically stabilises near  $\Gamma = 0.01$ , approaching a parabolically shaped shear pattern, insensitive to a further increase of  $\Gamma$ . Such a thickening of the boundary layer during deformation is consistent with the results of Shu et al. (2001) and Svendsen (2003), but is not pre-

**Table 3.2** / Constitutive parameters of copper, generalised for double slip; partly adopted from (Evers et al., 2002) or fitted on the data in that work, and partly taken from elsewhere (cf. the footed references); the coefficients  $a_0$  and  $h_0$  are entries on the diagonals of  $A^{\alpha\xi}$  and  $H^{\alpha\xi}$ , respectively.

Parameter		Magnitude		Used in Eq.
Young's modulus	$E$	144	GPa	(3.3)
Poisson's ratio	$\nu$	0.33	–	(3.3) (3.10) (3.12)
Reference plastic strain rate	$\dot{\gamma}_0$	0.001	$\text{s}^{-1}$	(3.4)
Rate sensitivity exponent <sup>a</sup>	$m$	0.05	–	(3.4)
Boltzmann's constant	$k$	$1.38 \times 10^{-23}$	$\text{J K}^{-1}$	(3.4)
Reference activation energy <sup>b</sup>	$G_0$	$4.54 \times 10^{-20}$	J	(3.5)
Strength parameter	$c$	0.3	–	(3.9)
Shear modulus	$\mu$	54.2	GPa	(3.9) (3.10) (3.12)
Burger's vector length <sup>c</sup>	$b$	0.256	nm	(3.9) (3.10) (3.12) (3.17) (3.19)
Interaction coefficient	$a_0$	0.06	–	(3.9) (in $A^{\alpha\xi}$ )
Radius GND evaluation area	$R$	$1.0 \times 10^{-5}$	m	(3.12)
Critical annihilation length <sup>d</sup>	$y_c$	1.6	nm	(3.17)
Initial SSD density	$\rho_{\text{SSD}_0}$	$7.0 \times 10^{12}$	$\text{m}^{-2}$	(3.17)
Material constant	$K$	26	–	(3.18)
Immobilisation coefficient	$h_0$	1.0	–	(3.18) (in $H^{\alpha\xi}$ )

<sup>a</sup>Tabourot et al. (1997)

<sup>b</sup>Ashmawi and Zikry (2000)

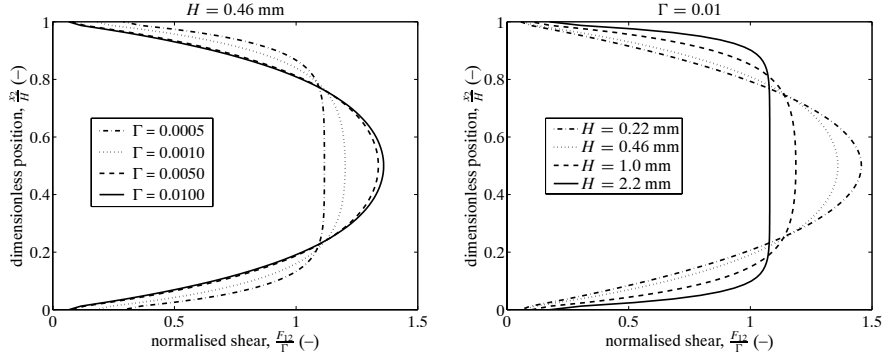
<sup>c</sup>Cuitiño and Ortiz (1992)

<sup>d</sup>Essmann and Mughrabi (1979)

dicted by simulations using the non-local strain gradient crystal plasticity theory of Shu and Fleck (1999), where the shape of the distribution is almost insensitive to the shear level  $\Gamma$  (Shu et al., 2001).

In order to investigate the effect of the strip height, the same normalised shear profile is plotted for various heights at a fixed total shear of  $\Gamma = 0.01$  in Fig. 3.2b. The deformation inhomogeneity becomes more pronounced at decreasing height and, below  $H = 0.46$  mm, the boundary layer develops over the full height of the strip. This corresponds to the notion that the *absolute* boundary layer width remains close to constant. This observation is also in agreement with the findings of Svendsen (2003) and of Shu et al. (2001), as well as with computations using the non-local plasticity theory of Gurtin (2002), which has been evaluated for this specific application by Bittencourt et al. (2003).



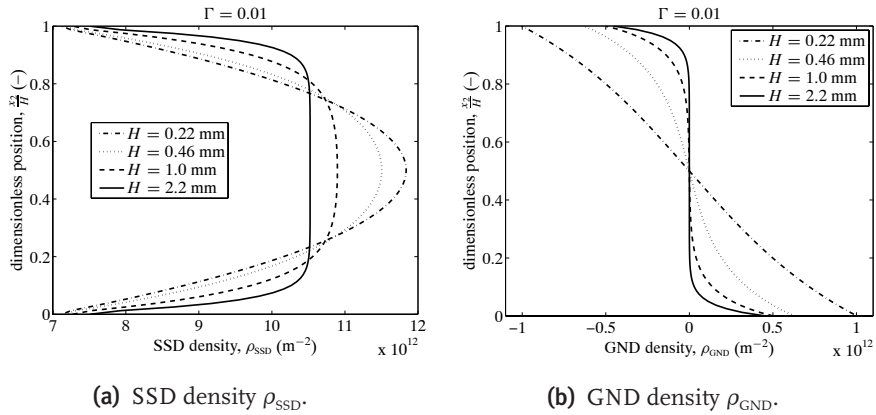


(a) Normalised shear profile for a fixed height of  $H = 0.46$  mm and for increasing deformation  $\Gamma$ .

(b) Normalised shear profile at a constant shear of  $\Gamma = 0.01$  and for various strip heights  $H$ .

**Figure 3.2** / Shear profiles along the dimensionless  $x_2$ -direction; the shear component  $F_{12}$  of the deformation gradient tensor is normalised by the applied macroscopic shear  $\Gamma$ , i.e. the average shear.

When considering the SSD density distributions along the strip height in Fig. 3.3a, an almost similar curve as the corresponding normalised shear profiles for the same heights in Fig. 3.2b can be observed, indicating the strong coupling between the SSD evolution and the crystallographic slip through Eq. (3.17), starting off at the initial value  $\rho_{\text{SSD}_0}$  near the walls, where the slip rates stay negligibly small.



(a) SSD density  $\rho_{\text{SSD}}$ .

(b) GND density  $\rho_{\text{GND}}$ .

**Figure 3.3** / Slip system 1 ( $\phi_1 = 60^\circ$ ) dislocation densities along the dimensionless  $x_2$ -direction at a constant shear of  $\Gamma = 0.01$  for various strip heights  $H$ ; the results for slip system 2 ( $\phi_2 = 120^\circ$ ) do not differ significantly.

On the other hand, the GND density clearly concentrates near the walls in Fig. 3.3b. The boundary layers accommodating these distinct peaks are comparable to the ones in the shear profiles in Fig. 3.2b. This perception has also been found in Shu et al. (2001), where the dislocation density profile –computed from *discrete* dislocations– for only one strip size is highlighted. Moreover, again a strong coupling is evident, not with the slip rates, but with the slip *gradients* through Eq. (3.19). Note that the SSD density saturates at the point where the accumulation and annihilation rates become equal, while the GND density continues to increase with persisting deformation.

The macroscopic shear stress ( $\tau = \sigma_{12}$ ) is normalised with  $\tau_0 = c\mu b\sqrt{h_0\rho_{SSD_0}}$  (cf. Eqs. (3.9) and (3.17)) and plotted against the applied shear ( $\Gamma$ ) in Fig. 3.4a for various heights. After a relatively sharp and constant yield point (since there are no gradient effects in the elastic regime), the normalised stress increases almost linearly with shear, exhibiting a clearly observable size effect, i.e. higher strengths for smaller  $H$ 's.

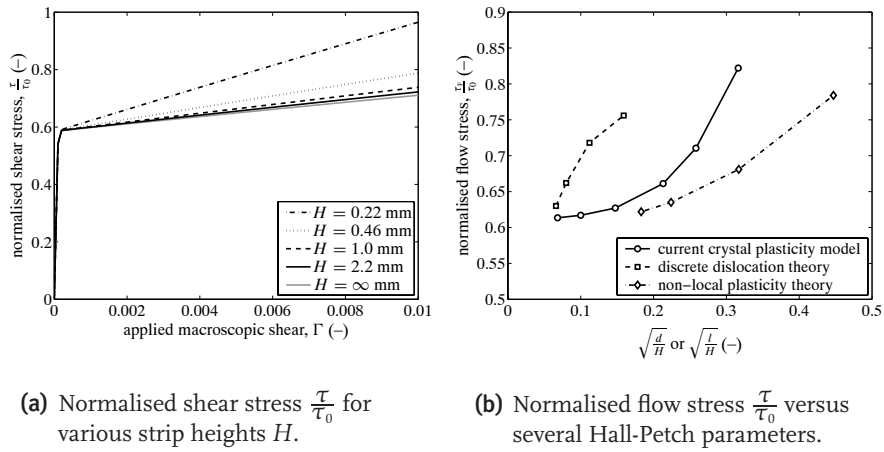


Figure 3.4 / Size dependence of shear stress and flow stress.

In order to gain more insight into this dependence, the normalised flow stress ( $\tau_F$ ) is plotted against the so-called ‘‘Hall-Petch ratio’’ ( $\sqrt{\frac{d}{H}}$  or  $\sqrt{\frac{l}{H}}$ ) in Fig. 3.4b, where  $d$  and  $l$  represent length scales (additional to  $b$  and  $H$ ) specifically related to the model concerned. Here, this length scale is taken to equal the radius of the GND evaluation area,  $l = R$ , indeed having a value substantially larger than the individual dislocation spacing. Following Shu et al. (2001)<sup>2</sup>, the flow stress is defined as the value of the shear stress

<sup>2</sup>In Shu et al. (2001),  $\tau_0$  represents the mean dislocation nucleation strength and the length scale parameter  $d$  is the slip plane spacing.

at a macroscopic shear  $\Gamma = 0.002$ . In the figure, also the predictions using the discrete dislocation theory and the non-local plasticity theory (Shu and Fleck, 1999) have been included, as adopted from Shu et al. (2001). According to the Hall-Petch relation, the slope of the lines is expected to be constant and approximately equal to one. For the current model, the latter is only true in an average sense, because of the progressive increase with decreasing height. This corresponds to a Hall-Petch exponent larger than  $\frac{1}{2}$ . This additional hardening can be explained by the fact that for smaller  $H$  values, together with the increasing slip gradients, the GND densities increase and approach the order of the SSD densities, such that they do not longer have a negligible effect on the slip resistance (cf. Eq. (3.9)), as is the case for larger heights  $H$ .

### 3.5 Conclusions

A crystal plasticity framework has been outlined with a clear distinction between the different evolutions and effects of the statistically-stored and geometrically-necessary dislocation densities. The actual framework incorporates relevant physical aspects necessary for consistently describing the scale dependent behaviour which is not captured using standard crystal plasticity models. Main characteristics and potential further improvements of the presented model can be summarised as follows:

- Short-range effects:  
For this issue, a conventional framework has been selected, depending on the different dislocation (both SSD and GND) interactions, the types of which are based on the orientations of their distinct slip systems. Yet, because it is believed that the resistance due to the short-range obstacles can be overcome by thermal activation, as a future improvement, it would be illustrative to explicitly include the temperature influence in the relations.
- Long-range effects:  
Only GND's were expected to play a significant role, essentially caused by their kinematic hardening contribution. Based on the consideration of a field of individual (edge) dislocations, each with a specific contribution to the resulting shear stress, it was possible to construct a generalised relation for that stress, governed by the *gradients* of the GND density field. A macroscopic back-stress measure has been constructed from the resulting stresses on all slip systems.
- SSD density evolution:  
A classic evolution equation has been adopted, where the description of the dislocation segment length was improved by considering both SSD and GND densities while using a similar formulation as for their interactions. As a possible future

improvement of the physical validity, the distinction between mobile and immobile dislocations, together with evolution equations dependent on generation, interaction, trapping, and recovery (Zikry and Kameda, 1998; Ashmawi and Zikry, 2000) can be included, as well as *screw* SSD densities, together with annihilation terms due to cross slip (Arsenlis and Parks, 2002).

- GND density evolution:  
Based on geometrical considerations, the edge and screw GND densities were directly related to the crystallographic slip gradients in different directions.

The implementation of the entire SSD and GND density based crystal plasticity framework has been established by means of a weak formulation, consistent linearisation and discretisation of the governing equations, i.e. the ordinary stress equilibrium condition completed with the GND evolution expression, resulting in a global system of equations to be solved iteratively. Additional boundary conditions allow the prescription of GND densities or crystallographic slip, of which the latter can be used in future applications to constrain slip in the normal direction of a grain boundary.

The model has been evaluated by comparison to discrete dislocation simulations and non-local crystal plasticity predictions for the constitutive behaviour of a constrained strip of crystalline material under simple shear. A good qualitative agreement has been found for the development of boundary layers and the related size dependent macroscopic stress-strain response.



## CHAPTER FOUR

# Single crystal model application to plane stress tension<sup>1</sup>

---

**Abstract** / The geometrically non-linear scale dependent response of polycrystal FCC metals is modelled by an enhanced crystal plasticity framework based on the evolution of several dislocation density types and their distinct physical influence on the mechanical behaviour. The isotropic hardening contribution follows from the evolution of statistically-stored dislocation (SSD) densities during plastic deformation, where the determination of the slip resistance is based on the mutual *short range* interactions between all dislocation types, i.e. including the geometrically-necessary dislocation (GND) densities. Moreover, the GND's introduce *long range* interactions by means of a back-stress measure, opposite to the slip system resolved shear stress.

The grain size dependent mechanical behaviour of a limited collection of grains under plane stress loading conditions is determined using the finite element method. Each grain is subdivided into finite elements and an additional expression, coupling the GND densities to spatial crystallographic slip gradients, renders the GND densities to be taken as supplemental nodal degrees of freedom. Consequently, these densities can be uncoupled at the grain boundary nodes, allowing for the introduction of grain boundary dislocations (GBD's) based on the lattice mismatch between neighbouring grains and enabling the obstruction of crystallographic slip perpendicular to the grain boundary.

### 4.1 Introduction

The grain size dependent mechanical behaviour of a polycrystal FCC metal has been modelled physically using a crystal plasticity approach for finite deformations. In most conventional single and polycrystal plasticity models, e.g. as published by Bronkhorst et al. (1992) and Kalidindi et al. (1992), the influence of inter- and intragranular inho-

---

<sup>1</sup>This chapter is reproduced from Evers et al. (2003b).

mogeneities is not explicitly incorporated in the constitutive description, whereas it is the basic origin of scale dependent behaviour and the resulting size effects. In general, such inhomogeneities at the microscale can be caused by externally applied macroscopic gradients of plastic deformation, by the presence of grain boundaries locally obstructing the plastic deformation (Becker and Panchanadeeswaran, 1995), or by a combination of both. The best-known macroscopic experimental consequence of these effects is the increased flow stress on decreasing average grain size, which is expressed by the so-called “Hall-Petch relation” (Hall, 1951; Petch, 1953; Armstrong et al., 1962). In particular, the flow stress is nearly proportional to the inverse square root of the average grain diameter (see also Hansen, 1982; Narutani and Takamura, 1991; Evers et al., 2003a).

Several suggestions have been proposed to explain this strengthening effect (Gavriljuk et al., 1999). The “dislocation pile-up models” are based on the perception that dislocations pile-up against grain boundaries and therefore obstruct the crystallographic slip through stress concentrations. On the other hand, “work hardening models” state that the overall concentration of dislocations in a grain increases once the volume in which they reside –which is connected to the grain size– decreases, corresponding to an increased inhomogeneity and a decreased mean free path within the grains. The presented model actually includes both effects, because dislocations concentrate at the grain boundaries and inflict a back-stress to the motion of dislocations carrying the plastic deformation, while at the same time, the strength of those dislocation concentrations depends on the heterogeneity within the grain, which increases with decreasing grain size.

Next to the so-called “geometrically-necessary dislocations” (GND’s), which are directly related to local non-uniform plastic deformations and which are required to preserve the compatibility of the crystallographic lattice in cases of unevenly distributed plastic slip, the second type of dislocations to be distinguished are “statistically-stored dislocations” (SSD’s), a distinction first identified by Ashby (1970). The latter dislocation density accumulates during (uniform as well as non-uniform) plastic deformation as a result of interactions between dislocations mutually, and the motion of SSD’s is actually the mechanism behind crystallographic (plastic) slip on the distinct slip planes of the material. It can be expected that the GND’s are concentrated near the grain boundary regions (Kocks, 1970; Thompson et al., 1973), due to the lattice mismatch with neighbouring grains, whereas the SSD densities mostly evolve in the grain interiors, as a result of the more intensive and less obstructed plastic flow in that region.

The actual difference between SSD’s and GND’s resides in their role only, i.e. in the fact that the latter do not directly participate in the local crystallographic slip, yet they emerge as a (non-local) result of spatial gradients of that slip. A second (resulting) difference between both types of dislocations is the sign and the variation of that sign in space. The SSD’s, due to their statistical nature, have a more or less random sign observed at a length scale associated with the grain structures, as a result of which any

bias cancels out and the SSD's do not contribute to any inhomogeneities. The sign of the GND densities has a profound geometrical impact and therefore a larger periodicity, as it is coupled to specific lattice curvatures and distortions. The actual identification of a certain dislocation as being a statistically-stored one or a geometrically-necessary one, however, remains rather ambiguous (since at the level of a single dislocation there is no physical difference), as well as keeping track of the process of dislocations switching between both types. Nevertheless, when the *densities* of both types are considered, a clear distinction can be made based on their characteristics, i.e. the GND density equals the minimum density (or local surplus of a certain sign) in order to accommodate the local plastic strain gradients, whereas the remaining density is considered to be statistically-stored (Gao and Huang, 2003).

After establishing the occurrence of both dislocation types, the entire framework is furnished to account for their distinct effect on the constitutive behaviour, incorporating any number or type (edge or screw) of dislocations. In general local continuum crystal plasticity models, the presence, motions, and interactions of dislocations are not explicitly distinguished, as only their effects are modelled indirectly by a phenomenological slip law and hardening evolution. The present framework (partly adopted from Evers et al., 2002) still incorporates a phenomenological slip law, however it is enhanced and the slip resistance is entirely based on short-range interactions between all (SSD as well as GND) dislocations intersecting the current slip system (Franciosi and Zaoui, 1982). Now, the accumulation of dislocations –related to the history of crystallographic slip– is the driving force behind the isotropic hardening term. Furthermore, a second extension is introduced to account for the distinct influence of the GND densities on the plastic slip in a long-range sense, i.e. through a back-stress measure, counteracting the local resolved shear stress and related to the heterogeneity of the GND field after removal of external loads. This provides for a physically motivated and consistent incorporation of global as well as local (intragranular) strain gradient effects and hence also of scale dependent effects such as grain size dependent responses.

Next to grain size effects and related size effects under micro-torsion (Fleck et al., 1994), the prediction of particle size effects (Ashby, 1970) and indenter size effects (Nix and Gao, 1998; Gao et al., 1999) is still the objective of ongoing study (e.g. Aifantis, 1987; Fleck and Hutchinson, 1997; Shu and Fleck, 1999), using so-called “strain gradient models”. Such approaches introduce an intrinsic material length scale in an analytical plasticity formulation, relying on the underlying generation and distribution of dislocations. Furthermore, continuum theories of dislocations have been formulated to further enhance those strain gradient models (Dai and Parks, 1997; Steinmann, 1996; Sluys and Estrin, 2000; Acharya, 2001; Bassani, 2001; Gurtin, 2002; Cermelli and Gurtin, 2002) by making use of (global) plastic or elastic incompatibilities, based on the work of Nye (1953). In the present chapter, as a further enhancement, the densities and their influence are solely and explicitly determined on the FCC slip systems, at a scale that includes global



as well as local strain gradients. A comparison of simulations using the actual model to the discrete dislocation predictions of a constrained strip under simple shear for the case of double slip (Shu et al., 2001) can be found in Evers et al. (2003a). Furthermore, Gurtin (2002) and Cermelli and Gurtin (2002) have developed a framework that is based on similar hypotheses as the one presented here, yet based on energetic considerations.

It is emphasized that in the present concept, the grain size does not explicitly enter the constitutive model and the model parameters can be kept constant throughout the entire grain. The grain size effect arises naturally as a result of intragranular heterogeneities affected by incompatibilities and obstructions at the grain boundaries. When the grain size is taken smaller, the inhomogeneities increase. Nevertheless, the primary length parameter entering the presented model is the length of the Burger's vector, which relates the plastic strain gradients to the GND densities at slip system level. Moreover, limiting the GND effect to an increased hardening rate or slip resistance near the grain boundaries (Worthington and Smith, 1964; Gray III et al., 1999) is not satisfactory, as clearly remarked by Mughrabi (2001), stating that a simple superposition of the GND density on the SSD density does not suffice. Microbending tests (Fleck et al., 1994; Stölken and Evans, 1998) suggest that the GND density can be substantially smaller than the SSD density, even though their contribution may be quite significant or even dominant.

In the next section, the entire crystal plasticity framework is presented, which covers the general constitutive formulation including an extended slip law, the determination of the entries in that slip law, i.e. the slip resistance and the back-stress, and finally the evolution equations for the SSD, GND, and "grain boundary dislocation" (GBD) densities. Next, in Section 4.3, the large deformation implementation of the entire model is discussed under the assumption of plane stress. Regarding the finite element formulation, the complete algorithmic framework is addressed, i.e. ranging from the integration point solutions up till the incremental-iterative solution of the global set of nonlinear equations. Finally, in Section 4.4, the response of a polycrystal FCC metal (consisting of 12 grains) under plane stress deformation is simulated, of which the grain size effect on the response and the intragranular variations of several quantities is demonstrated.

## 4.2 Crystal plasticity model

### 4.2.1 Constitutive framework

Point of departure is the classical multiplicative decomposition of the deformation gradient tensor into an elastic and a plastic part according to (Lee, 1969)

$$F = F_e \cdot F_p, \quad (4.1)$$

where the elastic deformation includes small lattice deformations and possibly large rigid body rotations. Next, the second Piola-Kirchhoff stress measure  $\boldsymbol{\tau} \equiv \det(\mathbf{F}_e) \mathbf{F}_e^{-1} \cdot \boldsymbol{\sigma} \cdot \mathbf{F}_e^{-T}$ , with respect to the stress-free intermediate configuration (Mandel, 1974), is taken to be elastically related to its work conjugated elastic Green strain measure  $\mathbf{E}_e$  through

$$\boldsymbol{\tau} = {}^4\mathbf{C} : \mathbf{E}_e, \quad \mathbf{E}_e \equiv \frac{1}{2} (\mathbf{C}_e - \mathbf{I}), \quad \mathbf{C}_e \equiv \mathbf{F}_e^T \cdot \mathbf{F}_e, \quad (4.2)$$

where  $\boldsymbol{\sigma}$  is the Cauchy stress tensor,  $\mathbf{C}_e$  is the elastic right Cauchy-Green deformation tensor and  $\mathbf{I}$  is the second-order unit tensor. The fourth-order isotropic elasticity tensor  ${}^4\mathbf{C}$  is defined by Young's modulus  $E$  and Poisson's ratio  $\nu$ .

Furthermore, the evolution of the plastic deformation is prescribed by the plastic velocity gradient tensor  $\mathbf{L}_p$ , which by definition can be written as the sum of all crystallographic slip rates  $\dot{\gamma}^\alpha$  on the 12  $\{111\}\langle 110\rangle$  slip systems  $\alpha$  of the FCC metal according to (Rice, 1971)

$$\dot{\mathbf{F}}_p = \mathbf{L}_p \cdot \mathbf{F}_p, \quad \mathbf{L}_p = \sum_{\alpha} \dot{\gamma}^\alpha \mathbf{P}_0^\alpha, \quad \mathbf{P}_0^\alpha \equiv \mathbf{m}_0^\alpha \mathbf{n}_0^\alpha, \quad \alpha = 1, 2, \dots, 12. \quad (4.3)$$

Here,  $\mathbf{P}_0^\alpha$  is the non-symmetric Schmid tensor, represented in the reference configuration as the dyadic product of the two orthonormal vectors  $\mathbf{m}_0^\alpha$  and  $\mathbf{n}_0^\alpha$ , the slip direction and slip plane normal, respectively.

The above elastic and plastic parts are coupled through a viscoplastic flow rule (Hutchinson, 1976; Peirce et al., 1982), which is defined for each slip system  $\alpha$  and specifies the rate of plastic shearing  $\dot{\gamma}^\alpha$  as a function of the associated "effective" shear stress  $\tau_{\text{eff}}^\alpha$  and the current slip resistance  $s^\alpha$  (see also Nemat-Nasser et al., 1998; Harder, 1999; Kocks, 2001; Evers et al., 2003a)

$$\dot{\gamma}^\alpha = \dot{\gamma}_0 \left( \frac{|\tau_{\text{eff}}^\alpha|}{s^\alpha} \right)^{\frac{1}{m}} \exp \left\{ -\frac{G_0}{kT} \left( 1 - \frac{|\tau_{\text{eff}}^\alpha|}{s^\alpha} \right) \right\} \text{sign}(\tau_{\text{eff}}^\alpha), \quad (4.4)$$

where  $\dot{\gamma}_0$  and  $m$  are material parameters representing the reference plastic strain rate and the rate sensitivity exponent,  $k$  is Boltzmann's constant,  $T$  is the absolute temperature, and  $G_0$  is the total free energy needed for a moving dislocation to overcome a short-range barrier without the aid of external work. Furthermore, the effective stress  $\tau_{\text{eff}}^\alpha$  is defined as the difference between the resolved shear stress  $\tau^\alpha$  (also known as "Schmid stress") and the resolved back-stress  $\tau_b^\alpha$

$$\tau_{\text{eff}}^\alpha = \tau^\alpha - \tau_b^\alpha, \quad \tau^\alpha \equiv \boldsymbol{\tau} : \mathbf{P}_0^\alpha, \quad \tau_b^\alpha \equiv \boldsymbol{\tau}_b : \mathbf{P}_0^\alpha, \quad (4.5)$$

where both resolved stress measures are projections (Asaro and Rice, 1977; Bronkhorst et al., 1992) of their corresponding stress tensors  $\boldsymbol{\tau}$  and  $\boldsymbol{\tau}_b$  (Harder, 1999) on slip system  $\alpha$ , respectively.

### 4.2.2 Dislocation interactions

The concepts above leave the slip system strengths and the back-stress tensor still to be determined. The back-stress tensor describes the effect of long-range stresses caused by the heterogeneity of the GND field, whereas the slip resistances are a measure for the impeding of dislocation movement by the formation of short-range interactions between both SSD's and GND's residing on coplanar or intersecting slip systems. The type and number of short-range interactions can be quantified through a set of interaction coefficients, stored in the interaction matrix  $A^{\alpha\xi}$  (Franciosi and Zaoui, 1982), after which the slip system strength  $s^\alpha$  is taken proportional to the square root of the effective obstacle density following Ashby (1970)

$$s^\alpha = c\mu b \sqrt{\sum_{\xi} A^{\alpha\xi} |\rho_{\text{SSD}}^{\xi}| + \sum_{\xi} A^{\alpha\xi} |\rho_{\text{GND}}^{\xi}|}. \quad (4.6)$$

In here,  $c$  is a constant ranging from 0.05 to 2.6 for different materials (Lavrentev, 1980),  $\mu$  is the shear modulus and  $b$  is the length of the Burger's vector. Furthermore, when considering FCC metals,  $\rho_{\text{SSD}}^{\xi}$  and  $\rho_{\text{GND}}^{\xi}$  stand for the 12 edge SSD densities ( $\xi = 1, 2, \dots, 12$ ) and the 12 edge and 6 screw GND densities ( $\xi = 1, 2, \dots, 18$ ), respectively (Kubin et al., 1992). A complete listing of the different dislocation densities, including their type, orientation, and corresponding slip system, is specified in Table 4.1.

The global back-stress tensor is defined in the reference configuration and is composed of the resulting long-range shear stress contributions ( $\tau_e^\alpha$  and  $\tau_s^\alpha$  of the particular edge and screw GND density field, respectively) on the respective slip systems  $\alpha$  according to (Harder, 1999)

$$\tau_b = \sum_{\alpha} -(\tau_e^\alpha + \tau_s^\alpha) \left( P_0^\alpha + P_0^{\alpha T} \right), \quad (4.7)$$

where the account for their spatial orientation through  $P_0^\alpha$  (cf. Eq. (4.3)) leads to a secondary resolved back-stress contribution on the other slip systems after employing Eq. (4.5). Note that the minus sign in this equation accounts for the transformation of the resulting long-range shear stress contributions to back-stress contributions in Eq. (4.5).

The determination of the resolved long-range shear stress contributions  $\tau_e^\alpha$  and  $\tau_s^\alpha$  in the undeformed configuration originally stems from the equations for the stress concentration near individual edge and screw dislocations by Cottrell (1961). However, when applying those equations to determine the resulting long-range stress state in a certain origin as caused by a uniform field of GND's, it completely cancels out. This is caused by the fact that each individual dislocation has a counterpart with an exact opposite contribution to the resulting long-range stress. Therefore, not the GND density field itself, but its spatial variations cause resulting long-range stresses.

In order to quantify that effect, the resulting long-range stress at slip system  $\alpha$  for the edge and screw GND densities is computed by an analytical integration procedure of the

**Table 4.1** / List of indices and vectors for dislocation densities and slip systems used in the simulation of FCC metals; the Schmid and Boas notation is discussed in Franciosi and Zaoui (1982);  $b$  is the length of the Burger's vector  $\mathbf{b}$ .

Dislocation density $\xi$	Slip sys- type	Slip sys- tem $\alpha$	$m$ or $\frac{\mathbf{b}}{b}$	$\mathbf{n}$	Schmid & Boas
1	edge	1	$\frac{1}{\sqrt{2}}[\bar{1}10]$	$\frac{1}{\sqrt{3}}(111)$	B5
2	edge	2	$\frac{1}{\sqrt{2}}[10\bar{1}]$	$\frac{1}{\sqrt{3}}(111)$	-B4
3	edge	3	$\frac{1}{\sqrt{2}}[0\bar{1}1]$	$\frac{1}{\sqrt{3}}(111)$	B2
4	edge	4	$\frac{1}{\sqrt{2}}[\bar{1}\bar{1}0]$	$\frac{1}{\sqrt{3}}(1\bar{1}\bar{1})$	A6
5	edge	5	$\frac{1}{\sqrt{2}}[101]$	$\frac{1}{\sqrt{3}}(1\bar{1}\bar{1})$	-A3
6	edge	6	$\frac{1}{\sqrt{2}}[01\bar{1}]$	$\frac{1}{\sqrt{3}}(1\bar{1}\bar{1})$	A2
7	edge	7	$\frac{1}{\sqrt{2}}[110]$	$\frac{1}{\sqrt{3}}(\bar{1}\bar{1}\bar{1})$	-D6
8	edge	8	$\frac{1}{\sqrt{2}}[\bar{1}01]$	$\frac{1}{\sqrt{3}}(\bar{1}\bar{1}\bar{1})$	-D4
9	edge	9	$\frac{1}{\sqrt{2}}[0\bar{1}\bar{1}]$	$\frac{1}{\sqrt{3}}(\bar{1}\bar{1}\bar{1})$	D1
10	edge	10	$\frac{1}{\sqrt{2}}[1\bar{1}0]$	$\frac{1}{\sqrt{3}}(\bar{1}\bar{1}\bar{1})$	-C5
11	edge	11	$\frac{1}{\sqrt{2}}[\bar{1}0\bar{1}]$	$\frac{1}{\sqrt{3}}(\bar{1}\bar{1}\bar{1})$	-C3
12	edge	12	$\frac{1}{\sqrt{2}}[011]$	$\frac{1}{\sqrt{3}}(\bar{1}\bar{1}\bar{1})$	C1
13	screw	-	$\frac{1}{\sqrt{2}}[110]$	$\frac{1}{\sqrt{3}}(1\bar{1}\bar{1})$ or $\frac{1}{\sqrt{3}}(\bar{1}\bar{1}\bar{1})$	-A6 or -D6
14	screw	-	$\frac{1}{\sqrt{2}}[101]$	$\frac{1}{\sqrt{3}}(1\bar{1}\bar{1})$ or $\frac{1}{\sqrt{3}}(\bar{1}\bar{1}\bar{1})$	-A3 or C3
15	screw	-	$\frac{1}{\sqrt{2}}[011]$	$\frac{1}{\sqrt{3}}(1\bar{1}\bar{1})$ or $\frac{1}{\sqrt{3}}(\bar{1}\bar{1}\bar{1})$	-D1 or C1
16	screw	-	$\frac{1}{\sqrt{2}}[\bar{1}10]$	$\frac{1}{\sqrt{3}}(111)$ or $\frac{1}{\sqrt{3}}(\bar{1}\bar{1}\bar{1})$	B5 or C5
17	screw	-	$\frac{1}{\sqrt{2}}[10\bar{1}]$	$\frac{1}{\sqrt{3}}(111)$ or $\frac{1}{\sqrt{3}}(\bar{1}\bar{1}\bar{1})$	-B4 or D4
18	screw	-	$\frac{1}{\sqrt{2}}[0\bar{1}\bar{1}]$	$\frac{1}{\sqrt{3}}(111)$ or $\frac{1}{\sqrt{3}}(1\bar{1}\bar{1})$	B2 or -A2

equations for individual dislocations (Cottrell, 1961) over a circular domain with radius  $R$  around the origin, while the GND densities are assumed to vary linearly in space.

$$\tau_e^\alpha = -\frac{\mu b R^2}{8(1-\nu)} \sum_{\xi} d_e^{\alpha\xi} \left( \nabla_0 \rho_{\text{GND}}^\xi \cdot \mathbf{m}_0^\alpha \right) \quad (4.8)$$

$$\tau_s^\alpha = \frac{\mu b R^2}{4} \sum_{\xi} d_s^{\alpha\xi} \left( \nabla_0 \rho_{\text{GND}}^\xi \cdot \mathbf{p}_0^\alpha \right), \quad \mathbf{p}_0^\alpha = \mathbf{m}_0^\alpha \times \mathbf{n}_0^\alpha. \quad (4.9)$$

Here, the multipliers  $d_e^{\alpha\xi}$  and  $d_s^{\alpha\xi}$  equal  $-1$ ,  $0$ , or  $1$ , according to the way the dislocation type  $\xi$  spatially relates to the slip system  $\alpha$  (cf. Table 4.1)

$$d_e^{\alpha\xi} = \begin{cases} 1 & \text{for } \alpha = \xi = 1, 2, \dots, 12 \\ 0 & \text{for all other cases} \end{cases} \quad (4.10)$$

$$d_s^{\alpha\xi} = \begin{cases} -1 & \text{for } d_s^{(4,13)}, d_s^{(6,18)}, d_s^{(8,17)}, d_s^{(9,15)}, d_s^{(10,16)}, d_s^{(11,14)} \\ 1 & \text{for } d_s^{(1,16)}, d_s^{(2,17)}, d_s^{(3,18)}, d_s^{(5,14)}, d_s^{(7,13)}, d_s^{(12,15)} \\ 0 & \text{for all other cases.} \end{cases} \quad (4.11)$$

### 4.2.3 Dislocation densities

In the remainder of this section, the determination of the SSD, GND and GBD densities is discussed. First, the evolution of the 12 edge SSD densities of the FCC metal, as required in Eq. (4.6), is based on the balance between the accumulation and annihilation rates, expressed by

$$\dot{\rho}_{\text{SSD}}^{\xi} = \frac{1}{b} \left( \frac{1}{d_e^{\alpha\xi} L^{\alpha}} - 2y_c \rho_{\text{SSD}}^{\xi} \right) d_e^{\alpha\xi} |\dot{\gamma}^{\alpha}|, \quad \rho_{\text{SSD}}^{\xi}(t=0) = \rho_{\text{SSD}_0}^{\xi}, \quad (4.12)$$

which is a generalisation of the relation originally proposed by Essmann and Mughrabi (1979). The accumulation rate (first term in the right-hand side of Eq. 4.12) is linked to the average dislocation segment length of mobile dislocations (SSD's) on system  $\alpha$ ,  $L^{\alpha}$ , which is strongly related to the current dislocation state through (Tabourot et al., 1997; Arsenlis and Parks, 2002)

$$L^{\alpha} = \frac{K}{\sqrt{\sum_{\xi} H^{\alpha\xi} |\rho_{\text{SSD}}^{\xi}| + \sum_{\xi} H^{\alpha\xi} |\rho_{\text{GND}}^{\xi}|}}. \quad (4.13)$$

Here,  $K$  is a constant and the coefficients  $H^{\alpha\xi}$  indicate the mutual immobilisation between dislocations of different slip systems, following the same convention as  $A^{\alpha\xi}$  in Eq. (4.6), yet having different values. Furthermore, the annihilation rate (second contribution in the right-hand side of Eq. 4.12) is assumed to be controlled by the critical annihilation length  $y_c$ , a material parameter characterising the average distance between two dislocations of opposite sign which triggers spontaneous neutralization.

Next, the GND density is determined from the gradients of the crystallographic slip in the undeformed situation from geometrical compatibility (Nye, 1953; Kröner, 1962; Ashby, 1970; Arsenlis and Parks, 2002)

$$\rho_{\text{GND}}^{\xi} = \rho_{\text{GND}_0}^{\xi} - \frac{1}{b} \sum_{\alpha} d_e^{\alpha\xi} (\nabla_0 \gamma^{\alpha} \cdot m_0^{\alpha}) + \frac{1}{b} \sum_{\alpha} d_s^{\alpha\xi} (\nabla_0 \gamma^{\alpha} \cdot p_0^{\alpha}). \quad (4.14)$$

For FCC metals, in contrast to the 12 positive SSD densities, the 12 edge and 6 screw GND densities have a certain polarity which is crucial to ascertain the direction of the slip system resolved back-stress. As can be clearly seen from Eq. (4.14), the sign of the GND densities is directly related to the sign of the corresponding crystallographic slip gradients. Each of the 6 screw dislocation densities is determined by addition of the appropriate slip gradients on *both* the glide planes in which they can reside, as they are assumed to be free to cross slip while their corresponding slip plane remains an ambiguous choice. This is consistent with the fact that in Eq. (4.11), each (screw) dislocation

density ( $\xi$ ) has two contributing slip systems ( $\alpha$ ), whose orientations can be found in Table 4.1. Furthermore, the initial GND density  $\rho_{\text{GND}_0}^\xi$  can be identified with the initial grain boundary dislocation density field, present before the onset of plastic deformation. The GBD densities are introduced to account for lattice incompatibilities across grain boundaries. Because of their geometrical nature, the GBD densities have similar constitutive influences as the GND densities. Therefore, as a part of  $\rho_{\text{GND}_0}^\xi$ , the 12 edge GND densities are taken equal to the initial grain boundary dislocation (GBD) densities

$$\rho_{\text{GND}_0}^\xi \equiv d_e^{\alpha\xi} \rho_{\text{GBD}}^\alpha. \quad (4.15)$$

This contribution is emphasized to be of qualitative nature, as the exact determination of the GBD densities, including the screw dislocations, is evidently more complicated than captured by the trends using the present simplified formulation, visualised in Fig. 4.1.

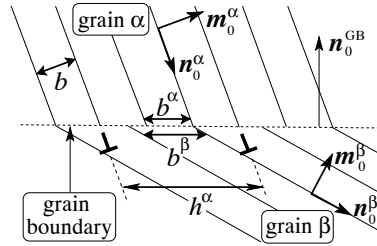


**Figure 4.1** / A grain boundary lattice mismatch gives rise to additional (GBD) dislocations; the GBD density is determined from the lengths of the grain boundary resolved Burger's vector ( $b^\alpha$  and  $b^\beta$ ) and the direction of the grain boundary unit normal  $n_0^{\text{GB}}$ .

To determine the GBD density, first, the slip system orientations of two adjacent grains  $\alpha$  and  $\beta$  are evaluated. In order to account for the symmetries of the FCC lattice, the slip systems of grain  $\alpha$  are related to the particular slip system configuration of grain  $\beta$ , as indicated in Table 4.2, that provides the best overall correspondence between all slip systems on either side, i.e. resulting in the smallest amount of GBD densities. Next, the GBD density is related to the misfit length  $h^\alpha$  between the slip system under consideration of grain  $\alpha$  and its associate slip system of grain  $\beta$ , where  $h^\alpha$  follows by comparing the lengths of their grain boundary resolved Burger's vectors,  $b^\alpha$  and  $b^\beta$ , respectively, according to

$$|\rho_{\text{GBD}}^\alpha| \equiv \frac{1}{h^\alpha} = \left( \frac{1}{b^\alpha} - \frac{1}{b^\beta} \right)^2. \quad (4.16)$$

**Table 4.2** / The slip systems of grain  $\alpha$  in the first row correspond to one of the slip system configurations of grain  $\beta$  in the consecutive rows, in accordance with the best geometrical match, depending on mutual orientation differences.

grain $\alpha$	1	2	3	4	5	6	7	8	9	10	11	12
related	1	2	3	4	5	6	7	8	9	10	11	12
slip sys-	2	3	1	11	12	10	5	6	4	8	9	7
tems of	3	1	2	9	7	8	12	10	11	6	4	5
grain $\beta$	4	5	6	1	2	3	10	11	12	7	8	9
	5	6	4	8	9	7	2	3	1	11	12	10
	6	4	5	12	10	11	9	7	8	3	1	2
	7	8	9	10	11	12	1	2	3	4	5	6
	8	9	7	5	6	4	11	12	10	2	3	1
	9	7	8	3	1	2	6	4	5	12	10	11
	10	11	12	7	8	9	4	5	6	1	2	3
	11	12	10	2	3	1	8	9	7	5	6	4
	12	10	11	6	4	5	3	1	2	9	7	8

When considering the grain boundary unit normal  $\mathbf{n}_0^{\text{GB}}$  to be pointed from the grain having the largest grain boundary resolved Burger's vector to the grain having the smallest one, the sign and magnitude of the GBD density can be expressed by

$$\rho_{\text{GBD}}^{\alpha} = \text{sign}(\mathbf{n}_0^{\alpha} \cdot \mathbf{n}_0^{\text{GB}}) \frac{\left( |\mathbf{n}_0^{\alpha} \cdot \mathbf{n}_0^{\text{GB}}| - |\mathbf{n}_0^{\beta} \cdot \mathbf{n}_0^{\text{GB}}| \right)^2}{b^2}. \quad (4.17)$$

Note that when the two neighbouring grains have the same crystallographic orientation, the GBD density turns out to be zero.

An overview displaying the dependences of the entire framework presented in this chapter can be found in Fig. A.1 of Appendix A.

## 4.3 Numerical implementation

### 4.3.1 Variational formulation

In order to implement the previously discussed crystal plasticity framework in a finite element framework, first, the governing equations must be identified. From Eq. (4.14), one can conclude that for the determination of the GND density field, the crystallographic slip fields for all slip systems are required. On the other hand, in order to determine the evolution of the crystallographic slip fields through Eq. (4.4), one needs the current back-stress, which again depends on the GND density field by means of Eqs. (4.8) and (4.9).

Once those densities are known, all relevant quantities can be determined. The GND densities are therefore chosen to be additional nodal degrees of freedom, accompanied by just as many additional evolution equations. Accordingly, the entire set of governing equations is given by the conventional stress equilibrium condition, evaluated in the undeformed configuration, and Eq. (4.14), here written in an abbreviated format

$$\nabla_0 \cdot \mathbf{T}^T = \mathbf{0}, \quad \mathbf{T} \equiv \det(\mathbf{F}) \boldsymbol{\sigma} \cdot \mathbf{F}^{-T} \quad (4.18)$$

$$\rho_{\text{GND}}^\xi = \rho_{\text{GND}_0}^\xi + \mathbf{d}_0^{\xi\alpha} \cdot \nabla_0 \gamma^\alpha \quad \forall \xi, \quad (4.19)$$

where  $\mathbf{T}$  is the first Piola-Kirchhoff stress tensor and where the multipliers  $d_e^{\alpha\xi}$  and  $d_s^{\alpha\xi}$ , the vectors  $\mathbf{m}_0^\alpha$  and  $\mathbf{p}_0^\alpha$ , the factor  $\frac{1}{b}$ , and the corresponding signs are all properly stored in the vectors  $\mathbf{d}_0^{\xi\alpha}$ , using Einstein's summation convention.

The continuity requirements on the displacements as well as the GND densities have to be relaxed over the element boundaries in order to be able to use standard  $C^0$ -continuous finite elements. This is accomplished by first multiplying the stress equilibrium and GND density evolution conditions by weighting functions  $w_u$  and  $w_\rho^\xi$ , respectively. After integrating both expressions over the volume  $V_0$  of the body in its reference (undeformed) configuration, the divergence theorem is applied and a Newton-Raphson iterative procedure is introduced, which provides the iterative corrections ( $\delta\mathbf{T}$ ,  $\delta\rho_{\text{GND}}^\xi$ , and  $\delta\gamma^\alpha$ ) to be expressed by linearised functions of the solution estimates ( $\mathbf{T}_*$ ,  $\rho_{\text{GND}_*}^\xi$ , and  $\gamma_*^\alpha$ ) obtained in the previous iteration

$$\int_{V_0} (\nabla_0 w_u)^T : \delta\mathbf{T}^T dV_0 = \int_{S_0} w_u \cdot \mathbf{t}_* dS_0 - \int_{V_0} (\nabla_0 w_u)^T : \mathbf{T}_*^T dV_0 \quad (4.20)$$

$$\int_{V_0} \left[ w_\rho^\xi \delta\rho_{\text{GND}}^\xi + (\nabla_0 w_\rho^\xi) \cdot \mathbf{d}_0^{\xi\alpha} \delta\gamma^\alpha \right] dV_0 = \int_{S_0} w_\rho^\xi \Gamma_{n_*}^\xi dS_0 - \dots \quad (4.21)$$

$$\int_{V_0} \left[ w_\rho^\xi (\rho_{\text{GND}_*}^\xi - \rho_{\text{GND}_0}^\xi) + (\nabla_0 w_\rho^\xi) \cdot \mathbf{d}_0^{\xi\alpha} \gamma_*^\alpha \right] dV_0 \quad \forall \xi,$$

where at the surface  $S_0$ ,  $\mathbf{t}_*$  is the (first Piola-Kirchhoff) surface traction and  $\Gamma_{n_*}^\xi$  is a measure for the crystallographic slip in the outward normal direction. In this weak formulation, the equations for the iterative corrections ( $\mathbf{T}_*$  and  $\gamma_*^\alpha$ ) and the iterative updates ( $\delta\mathbf{T}$  and  $\delta\gamma^\alpha$ ) are to be expressed and solved as a function of the so-called ‘‘independent variables’’, i.e. the variables which will be selected as the finite element nodal degrees of freedom and their spatial variations. This process is discussed in the next subsection.

### 4.3.2 Iterative updates and tangents

The elaborations (at the integration point level) in this subsection are presented under the assumption of plane stress loading conditions. Therefore, the total deformation gradient tensor is written as the additive decomposition

$$\mathbf{F} = \bar{\mathbf{F}} + \hat{\mathbf{F}}, \quad (4.22)$$



where  $\bar{F}$  only contains the four in-plane components of  $F$  and where  $\hat{F}$  contains the three non-zero components energetically associated to the stress components which are enforced to equal zero

$$T \cdot e_0^3 = 0. \quad (4.23)$$

Here, the initial unit base vector  $e_0^3$  is oriented in the out-of-plane direction. Next to the three degrees of freedom in  $\hat{F}$ , and next to  $\bar{F}$ , the remaining two components of the deformation gradient tensor equal zero. Now, three sets of variables are distinguished. First, the components of  $\hat{F}$  constitute, along with all slip rates  $\dot{\gamma}^\alpha$ , the entire set of dependent variables. This set is a priori unknown, yet it can be solved as a function of the independent variables  $\bar{F}$ ,  $\rho_{\text{GND}}^\xi$ , and  $r_0^\xi \equiv \nabla_0 \rho_{\text{GND}}^\xi$ , which are straightforwardly determined from the intentional nodal degrees of freedom. Together, both sets represent the entire set of state variables, a set which enables the consistent determination of all remaining relevant quantities.

In order to determine the dependent variables at the integration point level, accordingly, the following conditions must be satisfied

$$f(\bar{F}, \rho_{\text{GND}}^\xi, r_0^\xi, \hat{F}, \dot{\gamma}^\alpha) = 0 \quad (4.24)$$

$$g^\alpha(\bar{F}, \rho_{\text{GND}}^\xi, r_0^\xi, \hat{F}, \dot{\gamma}^\alpha) = 0 \quad \forall \alpha, \quad (4.25)$$

where Eq. (4.24) is actually a formal representation of Eq. (4.23), taking into account that the stress  $T$  is a priori unknown and is therefore considered to be related to all state variables. Furthermore, Eq. (4.25) is a representation of the slip laws in Eq. (4.4), where Eq. (4.5) is substituted for the effective stress, again depending on the second Piola-Kirchhoff stress through Eqs. (4.2), (4.1), and (4.3) and depending on the back-stress tensor via Eqs. (4.7), (4.8), and (4.9), and where Eq. (4.6) is substituted for the slip system strength, again depending on Eqs. (4.12) and (4.13). Fig. A.1 in Appendix A gives an overview of the aforementioned mutual dependences.

The system of strongly non-linear equations above –Eqs. (4.24) and (4.25)– requires an iterative solution procedure at the material point level. Resultingly, the dependent variables are unambiguously determined from the independent variables, which can formally be written as

$$\hat{F} = \hat{F}(\bar{F}, \rho_{\text{GND}}^\xi, r_0^\xi) \quad (4.26)$$

$$\dot{\gamma}^\alpha = \dot{\gamma}^\alpha(\bar{F}, \rho_{\text{GND}}^\xi, r_0^\xi). \quad (4.27)$$

The macroscopic iterative updates  $T_*$  and  $\dot{\gamma}_*^\alpha$ , as required in Eqs. (4.20) and (4.21), are solved accordingly by the same iteration process at the material point level. Similar to  $\hat{F}$  and  $\dot{\gamma}^\alpha$ ,  $T_*$  and  $\dot{\gamma}_*^\alpha$  also *primarily* dependent on the independent variables.

Now, after consistent linearisation of the crystal plasticity framework and the accompanying plane stress condition, the iterative corrections  $\delta T$  and  $\delta \gamma^\alpha$  at the macroscopic level (cf. Eqs. (4.20) and (4.21)) can be written as a function of the iterative variations of all independent variables

$$\delta T = \frac{\partial T}{\partial \bar{F}} \Big|_{\rho_{\text{GND}}^\xi, r_0^\xi} : \delta \bar{F} + \frac{\partial T}{\partial \rho_{\text{GND}}^\xi} \Big|_{\bar{F}, r_0^\xi} \delta \rho_{\text{GND}}^\xi + \frac{\partial T}{\partial r_0^\xi} \Big|_{\bar{F}, \rho_{\text{GND}}^\xi} \cdot \delta r_0^\xi \quad (4.28)$$

$$\delta \gamma^\alpha = \frac{\partial \gamma^\alpha}{\partial \bar{F}} \Big|_{\rho_{\text{GND}}^\xi, r_0^\xi} : \delta \bar{F} + \frac{\partial \gamma^\alpha}{\partial \rho_{\text{GND}}^\xi} \Big|_{\bar{F}, r_0^\xi} \delta \rho_{\text{GND}}^\xi + \frac{\partial \gamma^\alpha}{\partial r_0^\xi} \Big|_{\bar{F}, \rho_{\text{GND}}^\xi} \cdot \delta r_0^\xi, \quad (4.29)$$

where the subscripts next to the vertical bars indicate that the specified variables are kept constant. Here, it is acknowledged that the constitutive formulations of the quantities  $T$  and  $\gamma^\alpha$  primarily depend on the chosen independent variables  $\bar{F}$ ,  $\rho_{\text{GND}}^\xi$ , and  $r_0^\xi$ , yet secondarily also on the (a priori unknown) dependent variables  $\hat{F}$  and  $\hat{\gamma}^\alpha$ . However, this secondary dependence does not involve explicit formulations that can be extracted (as already pointed out, Eqs. (4.26) and (4.27) imply the iterative solution of Eqs. (4.24) and (4.25)). Therefore, in order to explicitly determine the partial derivatives in Eqs. (4.28) and (4.29), those secondary dependences have to be taken into account.

First, with the purpose of abbreviating the formulations exploiting the secondary dependences, consider the following definitions

$$\underline{\Pi} = \begin{bmatrix} T \\ \gamma^\alpha \end{bmatrix}, \quad \underline{\Xi} = \begin{bmatrix} \bar{F} \\ \rho_{\text{GND}}^\xi \\ r_0^\xi \end{bmatrix}, \quad \underline{\Psi} = \begin{bmatrix} \hat{F} \\ \hat{\gamma}^\alpha \end{bmatrix}, \quad \underline{\Phi} = \begin{bmatrix} f \\ g^\alpha \end{bmatrix}, \quad (4.30)$$

where all components of the tensor and vector quantities, and the complete set of the slip system and dislocation density related quantities, are properly stored in the columns, incorporating the primary unknowns ( $\underline{\Pi}$ ), the independent variables ( $\underline{\Xi}$ ), the dependent variables ( $\underline{\Psi}$ ), and the constitutive conditions ( $\underline{\Phi}$ ). Eqs. (4.28–4.29) can now be summarised by

$$\delta \underline{\Pi} = \frac{d\underline{\Pi}}{d\underline{\Xi}} \delta \underline{\Xi}, \quad (4.31)$$

where the matrix  $\frac{d\underline{\Pi}}{d\underline{\Xi}}$  contains all relevant partial derivatives. Next, the components of this matrix are elaborated by making a clear distinction between the independent variables and the dependent variables

$$\frac{d\underline{\Pi}}{d\underline{\Xi}} = \frac{\partial \underline{\Pi}}{\partial \underline{\Xi}} \Big|_{\underline{\Psi}} + \frac{\partial \underline{\Pi}}{\partial \underline{\Psi}} \Big|_{\underline{\Xi}} \frac{d\underline{\Psi}}{d\underline{\Xi}}, \quad (4.32)$$

an exercise which allows for the explicit determination of the entries in  $\frac{\partial \underline{\Pi}}{\partial \underline{\Xi}} \Big|_{\underline{\Psi}}$  and  $\frac{\partial \underline{\Pi}}{\partial \underline{\Psi}} \Big|_{\underline{\Xi}}$ .

The total derivative  $\frac{d\Psi}{d\underline{\Xi}}$  of the dependent variables with respect to the independent variables in Eq. (4.32) can not be determined explicitly. Instead, this derivative follows from the consideration that the requirements in Eqs. (4.24) and (4.25) must be satisfied

$$\delta\Phi = \frac{d\Phi}{d\underline{\Xi}}\delta\underline{\Xi} = 0, \quad (4.33)$$

that is, for all variations of the independent variables

$$\frac{d\Phi}{d\underline{\Xi}} = \frac{\partial\Phi}{\partial\underline{\Xi}}\Big|_{\underline{\Psi}} + \frac{\partial\Phi}{\partial\underline{\Psi}}\Big|_{\underline{\Xi}} \frac{d\underline{\Psi}}{d\underline{\Xi}} = 0, \quad (4.34)$$

where the partial derivatives in  $\frac{\partial\Phi}{\partial\underline{\Xi}}\Big|_{\underline{\Psi}}$  and  $\frac{\partial\Phi}{\partial\underline{\Psi}}\Big|_{\underline{\Xi}}$  can again be derived explicitly, which were actually already required for the material point Newton Raphson iteration procedure for the solution of Eqs. (4.24) and (4.25). The remaining derivatives can now be extracted according to

$$\frac{d\underline{\Psi}}{d\underline{\Xi}} = - \left( \frac{\partial\Phi}{\partial\underline{\Psi}}\Big|_{\underline{\Xi}} \right)^{-1} \frac{\partial\Phi}{\partial\underline{\Xi}}\Big|_{\underline{\Psi}}. \quad (4.35)$$

Finally, the solution estimates and iterative corrections of the primary unknowns, i.e.  $T_*$ ,  $\gamma_*^\alpha$ ,  $\delta T$ , and  $\delta\gamma^\alpha$  in Eqs. (4.20) and (4.21), are determined as a function of the nodal degrees of freedom and their spatial variations through Eq. (4.31).

The presented equations are formulated schematically, yet their elaboration only requires the determination of the partial derivatives in  $\frac{\partial\Pi}{\partial\underline{\Xi}}\Big|_{\underline{\Psi}}$ ,  $\frac{\partial\Pi}{\partial\underline{\Psi}}\Big|_{\underline{\Xi}}$ ,  $\frac{\partial\Phi}{\partial\underline{\Xi}}\Big|_{\underline{\Psi}}$ , and  $\frac{\partial\Phi}{\partial\underline{\Psi}}\Big|_{\underline{\Xi}}$ , which would be too comprehensive to include here. It is remarked that the time integration schemes required to compute  $\gamma^\alpha$  from Eq. (4.4) and  $\rho_{SSD}^\alpha$  from Eq. (4.12) can be chosen arbitrarily between fully explicit and fully implicit.

### 4.3.3 Finite element formulation

In order to systematically compute an approximate solution of the Eqs. (4.20–4.21), for arbitrary geometries and boundary conditions, the volume  $V_0$  of the configuration is subdivided in finite elements, whose contributions are subsequently added in a standard manner. Within each element  $e$  (having volume  $V_0^e$  and boundary surface  $S_0^e$ ), the unknown fields of the nodal variables and weighting functions, as well as their spatial variations, are approximated by their (global) nodal values (stored in  $\underline{u}$  and  $\underline{\rho}_{GND}$ ), multiplied by their corresponding interpolation functions (stored in  $\underline{N}_u^e$  and  $\underline{N}_\rho^e$ ) or the spatial derivatives thereof (stored in  $\underline{B}_u^e$  and  $\underline{B}_\rho^e$ ). Furthermore, the components and indices of  $\underline{d}_0^{\xi\alpha}$  are stored per element in  $\underline{D}^e$ , and following the procedures from Section 4.3.2, the iterative

estimations of the first Piola-Kirchhoff stress tensor and the crystallographic slips (stored in  $\underline{T}_*^e$  and  $\underline{\gamma}_{\text{GND}_*}^e$ ) can be computed in each material point, based on the nodal degrees of freedom, as well as their iterative corrections (stored in  $\delta \underline{T}_*^e$  and  $\delta \underline{\gamma}^e$ )

$$\delta \underline{T}_*^e = \underline{C}_1^e \underline{B}_u^e \delta \underline{u} + (\underline{C}_2^e \underline{N}_\rho^e + \underline{C}_3^e \underline{B}_\rho^e) \delta \rho_{\text{GND}} \quad (4.36)$$

$$\delta \underline{\gamma}^e = \underline{C}_4^e \underline{B}_u^e \delta \underline{u} + (\underline{C}_5^e \underline{N}_\rho^e + \underline{C}_6^e \underline{B}_\rho^e) \delta \rho_{\text{GND}}, \quad (4.37)$$

where  $\delta \underline{u}$  and  $\delta \rho_{\text{GND}}$  are the iterative corrections for the nodal displacement and GND density values, and where the matrices  $\underline{C}_1^e$ ,  $\underline{C}_2^e$ ,  $\underline{C}_3^e$ ,  $\underline{C}_4^e$ ,  $\underline{C}_5^e$ , and  $\underline{C}_6^e$ , represent the derivatives as specified in Eqs. (4.28–4.29) or equivalently Eq. (4.31), evaluated separately for each element.

After following the standard Galerkin approach and taking into account that both Eqs. (4.20–4.21) must be satisfied for any admissible weighting function, the following system of equations is established, comprising the discrete force balance and discretised GND density evolution conditions.

$$\begin{bmatrix} \underline{K}_{uu} & \underline{K}_{u\rho} \\ \underline{K}_{\rho u} & \underline{K}_{\rho\rho} \end{bmatrix} \begin{bmatrix} \delta \underline{u} \\ \delta \rho_{\text{GND}} \end{bmatrix} = \begin{bmatrix} \underline{r}_u \\ \underline{r}_\rho \end{bmatrix}, \quad (4.38)$$

where

$$\underline{K}_{uu} = \sum_e \int_{V_0^e} \underline{B}_u^{eT} \underline{C}_1^e \underline{B}_u^e dV_0^e \quad (4.39)$$

$$\underline{K}_{u\rho} = \sum_e \int_{V_0^e} \underline{B}_u^{eT} (\underline{C}_2^e \underline{N}_\rho^e + \underline{C}_3^e \underline{B}_\rho^e) dV_0^e \quad (4.40)$$

$$\underline{K}_{\rho u} = \sum_e \int_{V_0^e} \underline{B}_\rho^{eT} \underline{D}^e \underline{C}_4^e \underline{B}_u^e dV_0^e \quad (4.41)$$

$$\underline{K}_{\rho\rho} = \sum_e \int_{V_0^e} [\underline{N}_\rho^{eT} \underline{N}_\rho^e + \underline{B}_\rho^{eT} \underline{D}^e (\underline{C}_5^e \underline{N}_\rho^e + \underline{C}_6^e \underline{B}_\rho^e)] dV_0^e \quad (4.42)$$

$$\underline{r}_u = \sum_e \int_{S_0^e} \underline{N}_u^{eT} \underline{t}_*^e dS_0^e - \sum_e \int_{V_0^e} \underline{B}_u^{eT} \underline{T}_*^e dV_0^e \quad (4.43)$$

$$\underline{r}_\rho = \sum_e \int_{S_0^e} \underline{N}_\rho^{eT} \underline{\Gamma}_{n_*}^e dS_0^e \dots \quad (4.44)$$

$$- \sum_e \int_{V_0^e} [\underline{N}_\rho^{eT} \underline{N}_\rho^e (\rho_{\text{GND}_*}^e - \rho_{\text{GND}_0}^e) + \underline{B}_\rho^{eT} \underline{D}^e \underline{\gamma}_*^e] dV_0^e, \quad (4.45)$$

where the boundary terms  $\underline{t}_*^e$  and  $\underline{\Gamma}_{n_*}^e$  only have to be specified on element boundaries ( $S_0^e$ ) coinciding with the outer boundary of the body ( $S_0$ ). This system is solved by iteratively updating the nodal estimations  $\underline{u}_*$  and  $\rho_{\text{GND}_*}^e$  with corrections  $\delta \underline{u}$  and  $\delta \rho_{\text{GND}}$ , a process which is repeated until an appropriate convergence criterion is satisfied, i.e. until the right-hand side becomes sufficiently small.

Additionally, the grain boundaries can be regarded to be a part of that outer boundary. To accomplish this, the local finite elements must be uncoupled by means of placing double nodes at the grain boundaries, of which the displacements are again tied by specifying dependences in order to maintain the polycrystal sample consistent. That leaves the GND densities or the herewith associated forces to be specified, corresponding to Dirichlet (essential) or Neumann (natural) boundary conditions, respectively.

As the initial GND densities –here representing the GBD densities– can be determined from the crystallographic lattice mismatch (cf. Section 4.2.3), these can subsequently be prescribed at the nodes on *both* sides of the grain boundaries (i.e. Dirichlet boundary conditions). In order not to disturb the GND density evolution during deformation, the associated initial GND density field is determined by a separate finite element computation on beforehand. During that separate computation, the displacements at the outer boundaries are fixed to zero and at the grain boundary nodes, the GND densities are prescribed to evolve gradually (i.e. linearly, in 15 steps) until the desired value is attained. The resulting GND density field (integration point values) is adopted to serve as the initial GND density field in the actual deformation process simulations.

The total amount of *individual* GBD's necessary to account for lattice incompatibility across the grain boundaries is determined by the initial configuration, and is therefore solely dependent on the initial lattice mismatch. However, during the initial separate finite element computation, the GBD *densities* –as being nodal variables– are inherently spread over a certain area near the grain boundaries. Given the fact that the amount of individual GND's should not change, and the numerical observation that the *relative* GBD density variation between the grain boundary and core is size independent, the dislocation density to be prescribed at the grain boundary nodes ( $\rho_{\text{node}_0}^\xi$ ) should follow a relation like (cf. Eqs. (4.15) and (4.17))

$$\rho_{\text{node}_0}^\xi = \frac{\kappa}{d} \sqrt{\rho_{\text{GND}_0}^\xi}, \quad (4.46)$$

where  $\kappa$  is a dimensionless material constant and  $d$  is the grain diameter.

Next, during the finite element simulations of the deformation process, the plastic shear in the grain boundary normal directions is enforced to equal zero (i.e. Neumann boundary conditions), which actually corresponds to the obstruction of crystallographic slip across the grain boundaries. Finally, free boundaries are modelled by enforcing the GND density to vanish locally. Both boundary conditions are quite realistic and constitute a physically based description of crystallographic boundaries.

## 4.4 Simulations

The computational implementation of the model under plane stress conditions as discussed in Section 4.3 has been applied to simulate the size dependent constitutive behaviour of the polycrystal sample which is depicted in Fig. 4.2. The sample, consisting of 12 grains, is subdivided into 265 linear finite elements, with 379 nodes (4 nodes per element) and 20 degrees of freedom per node (2 displacements and 18 GND densities) resulting in a total number of 7580 degrees of freedom. In addition, the incorporation of double nodes at the grain boundaries requires the account for 176 displacement dependencies in order to kinematically couple the individual grains. Moreover, the entire system of equations is solved using full numerical integration, i.e. 4 integration points per element.

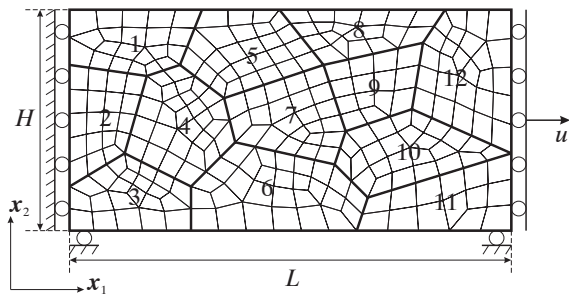


**Figure 4.2** / Geometry and classical displacement boundary conditions with respect to the simulations of the FCC polycrystal sample with length  $L$  and height  $H$  in tension; the remaining boundary conditions and dependences are explained in the text.

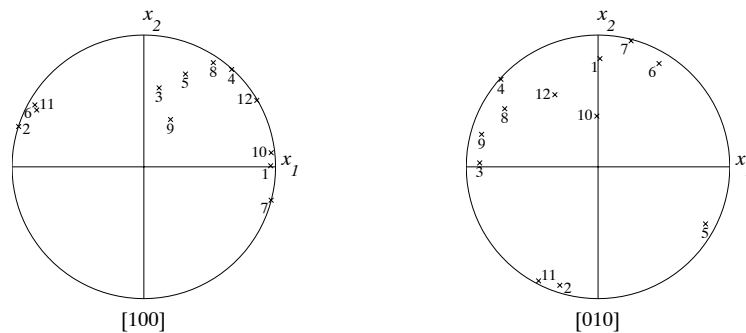


**Figure 4.3** / Equal area projection pole figures with the basic crystallographic lattice directions.

For all simulations, the random crystallographic orientations of the 12 grains are kept equal for all simulated sample sizes and are visualised in Fig. 4.3. The displacement boundary conditions are presented in Fig. 4.2, where  $u_1$  is prescribed such that the associated macroscopic strain rate remains fixed at  $0.001 \text{ s}^{-1}$  (up to a total strain of 0.01 in 175 increments). The remaining boundary conditions, related to the additional degrees of freedom, i.e. the nodal GND densities or alternatively, the corresponding plastic shear components in the direction perpendicular to the grain boundaries or free surfaces, are attributed as already explained at the end of Section 4.3. Furthermore, an initial GND density field is supposed to represent the GBD densities, related to the specific grain boundary lattice mismatches, a procedure which is also discussed in Section 4.3. The sample lengths  $L$  are taken to equal  $10^{-3} \text{ m}$ ,  $10^{-\frac{8}{3}} \text{ m}$ ,  $10^{-\frac{7}{3}} \text{ m}$  and  $10^{-2} \text{ m}$  (equivalent to 1.0 mm, 2.2 mm, 4.6 mm and 10 mm, respectively). Once the sample size decreases, the intragranular (plastic) inhomogeneities are expected to increase, along with the GND densities, which then play a significant role in strengthening the specimen through short- and long-range interactions. Finally, the temperature (in Eq. (4.4)) is taken 300 K and the material constants of FCC copper (12 slip systems and SSD types, 18 GND types) are specified in Table 4.3.

In the following, the results for the specimen lengths 1 mm and 10 mm are compared in order to achieve a clear insight into the various size effects. First, a scalar measure for the dislocation densities is evaluated, which is taken to equal the Euclidean norm of all SSD or GND density contributions. Note that the dislocation sign of the GND densities is not considered in this respect, as such would be too comprehensive for 18 different types. The distribution of the density measure for the SSD's is presented in Fig. 4.4, from which it can be concluded that the difference in order of magnitude between both length scales remains rather small.

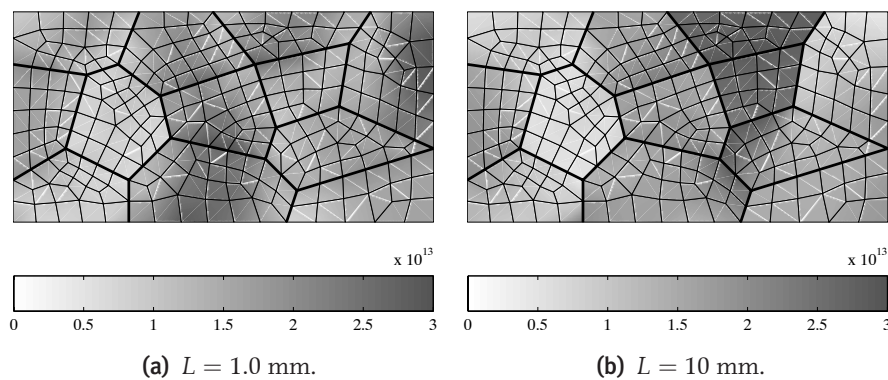


**Figure 4.4** / Distribution of the SSD density measure for two sample lengths at an equivalent strain of  $\varepsilon = 0.01$ .

**Table 4.3** / Constitutive parameters for FCC copper; partly adopted from (Evers et al., 2002) or fitted on the data in that work, and partly taken from elsewhere (cf. the footed references); the coefficients  $a_0$ ,  $a_1$ ,  $a_2$  and  $a_3$  are entries in the dislocation interaction matrix  $A^{\alpha\xi}$ , which is documented by Franciosi and Zaoui (1982) and quantified for copper by Cuitiño and Ortiz (1992); the coefficients  $h_0$ ,  $h_1$ ,  $h_2$  and  $h_3$  are entries in  $H^{\alpha\xi}$ , whose values for copper are adopted from Tabourot et al. (1997).

Parameter		Magnitude	Used in Eq.
Young's modulus	$E$	144	GPa (4.2)
Poisson's ratio	$\nu$	0.33	– (4.2) (4.8)
Reference plastic strain rate	$\dot{\gamma}_0$	0.001	$s^{-1}$ (4.4)
Rate sensitivity exponent <sup>a</sup>	$m$	0.05	– (4.4)
Boltzmann's constant	$k$	$1.38 \times 10^{-23}$	J K <sup>-1</sup> (4.4)
Reference activation energy <sup>b</sup>	$G_0$	$4.54 \times 10^{-20}$	J (4.4)
Strength parameter	$c$	0.3	– (4.6)
Shear modulus	$\mu$	54.2	GPa (4.6) (4.8) (4.9)
Burger's vector length <sup>c</sup>	$b$	0.256	nm (4.6) (4.8) (4.9) (4.12) (4.14) (4.17)
Interaction coefficient	$a_0$	0.06	– (4.6) (in $A^{\alpha\xi}$ )
Interaction coefficient	$a_1/a_0$	5.7	– (4.6) (in $A^{\alpha\xi}$ )
Interaction coefficient	$a_2/a_0$	10.2	– (4.6) (in $A^{\alpha\xi}$ )
Interaction coefficient	$a_3/a_0$	16.6	– (4.6) (in $A^{\alpha\xi}$ )
Radius GND evaluation area	$R$	$3.16 \times 10^{-6}$	m (4.8) (4.9)
Critical annihilation length <sup>d</sup>	$y_c$	1.6	nm (4.12)
Initial SSD density <sup>e</sup>	$\rho_{SSD_0}$	$1.0 \times 10^{12}$	$m^{-2}$ (4.12)
Material constant <sup>f</sup>	$K$	10	– (4.13)
Immobilisation coefficient	$h_0$	0.2	– (4.13) (in $H^{\alpha\xi}$ )
Immobilisation coefficient	$h_1$	0.3	– (4.13) (in $H^{\alpha\xi}$ )
Immobilisation coefficient	$h_2$	0.4	– (4.13) (in $H^{\alpha\xi}$ )
Immobilisation coefficient	$h_3$	1.0	– (4.13) (in $H^{\alpha\xi}$ )
GBD parameter	$\kappa$	0.1	– (4.46)

<sup>a</sup>Tabourot et al. (1997)

<sup>b</sup>Ashmawi and Zikry (2000)

<sup>c</sup>Cuitiño and Ortiz (1992)

<sup>d</sup>Essmann and Mughrabi (1979)

<sup>e</sup>Cuitiño and Ortiz (1992)

<sup>f</sup>Sabar et al. (2002)



When regarding the distribution of that same measure, however now evaluated for the GND densities in Fig. 4.5, a clear distinction between both scales can be observed. In the case of the small sample, the order of magnitude of the GND densities is roughly 5 times less than the SSD counterpart, whereas the GND densities of the large sample are almost negligible. The first explanation for this is the fact that, as a result of Eq. (4.46), the total amount of GBD dislocations necessary to account for lattice incompatibility across the grain boundaries is automatically spread over a larger area in Fig. 4.5b, resulting in an initial difference between both GND density distributions. The second explanation for the larger GND density magnitude in Fig. 4.5a is the fact that, during deformation, the plastic inhomogeneity between the grain core and the boundaries –where the slip is obstructed– has to be overcome within a much smaller distance (factor 10) in the  $L = 1$  mm case. According to Eq. (4.14), the GND densities automatically increase when the plastic slip gradients increase, which does not only result in an increased slip resistance through Eq. (4.6), but also in an increased back-stress contribution via Eqs. (4.8–4.9) and (4.7).

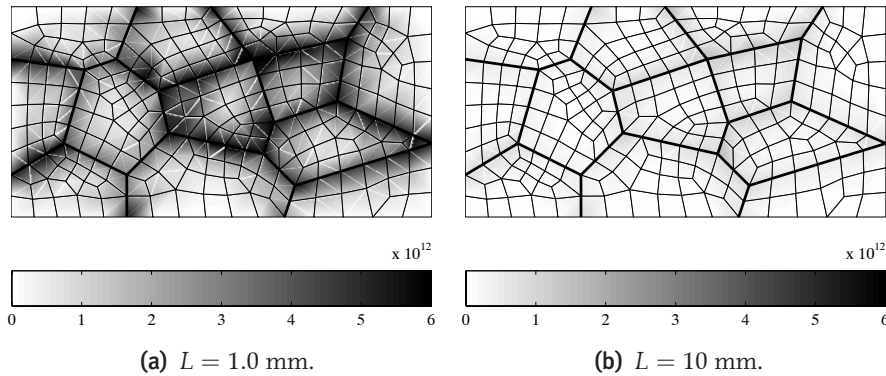


**Figure 4.5** / Distribution of the GND density measure for two sample lengths at an equivalent strain of  $\varepsilon = 0.01$ .

In order to examine the development of the dislocation density measures during the course of the deformation and to recover their actual value, they are evaluated along a cross section at half the sample height for various equivalent logarithmic strain values  $\varepsilon = \sqrt{\frac{2}{3}} \varepsilon : \varepsilon$ , where  $\varepsilon = \ln(\mathbf{U})$  and  $\mathbf{U}$  is the right stretch tensor. Herewith, 5 grain boundaries are intersected, of which the positions are graphically represented by the dashed vertical lines. In Figs. 4.6a and 4.6b, it can be clearly observed that the SSD densities evolve slightly more in the core regions of the grains than in the grain boundary regions. This can be attributed to the SSD density evolution in Eq. (4.12), which is higher in regions where the crystallographic slip is less impeded. As already emphasized above, no significant differences arise between both length scales.

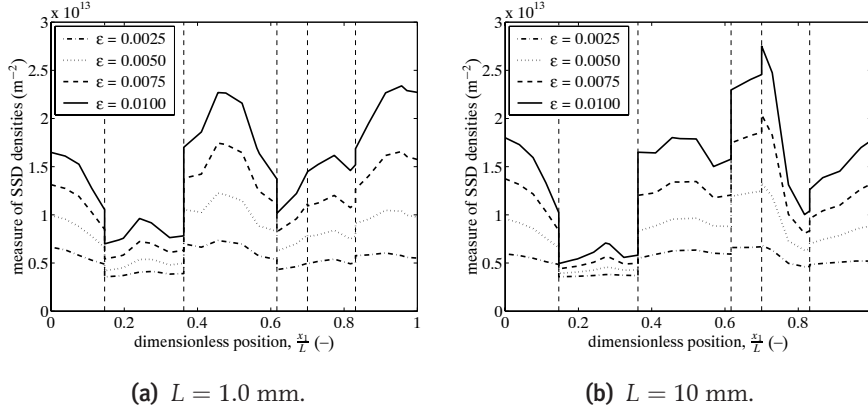


**Figure 4.6** / Profile of the measure for the SSD densities along the  $x_1$ -direction for increasing deformation  $\varepsilon$ , evaluated at half the sample height; the vertical dashed lines indicate the  $x_1$ -positions of the grain boundary intersections.

The GND density profiles along the intersection for both length scales are shown in Figs. 4.7a and 4.7b. Here indeed a huge difference is observed, where the GND densities of the large sample are approximately 7 times smaller than those of the small sample. In contrast to the SSD profiles, the GND densities increase near the grain boundary and decrease toward the grain cores and toward the GND-free outer surface, entirely in agreement with the expectations. Moreover, the relative *evolution* of the GND densities during deformation is considerably smaller than the evolution of the SSD densities, which triggers the question whether such GND profiles would also arise in absence of any initial GND densities. As a verification of this, the same simulations have been performed, yet without the grain boundary dislocation densities. The accompanying profiles of the GND density measure are shown in Figs. 4.8a and 4.8b. In the right part of the sample, the GND density measure quickly increases to similar levels, while the densities on the left remain a little smaller. However, the tendency of the GND densities to increase toward the grain boundaries remains intact, which can therefore be attributed to the additional boundary conditions that obstruct plastic slip in the direction perpendicular to those boundaries.

Finally, the stress-strain responses for the various sample sizes under consideration are evaluated. For bulk grains, it is expected that the flow stress will follow the Hall-Petch relation (Hall, 1951; Petch, 1953; Armstrong et al., 1962)

$$\sigma(\varepsilon) = \sigma_0(\varepsilon) + k(\varepsilon)d^{-n}, \quad (4.47)$$

where  $\varepsilon$  is the equivalent logarithmic strain measure defined previously and  $\sigma$  is the equivalent von Mises stress according to

$$\sigma = \sqrt{\frac{3}{2}\sigma_d : \sigma_d}, \quad \sigma_d = \sigma - \frac{1}{3}\text{tr}(\sigma)I \quad (4.48)$$

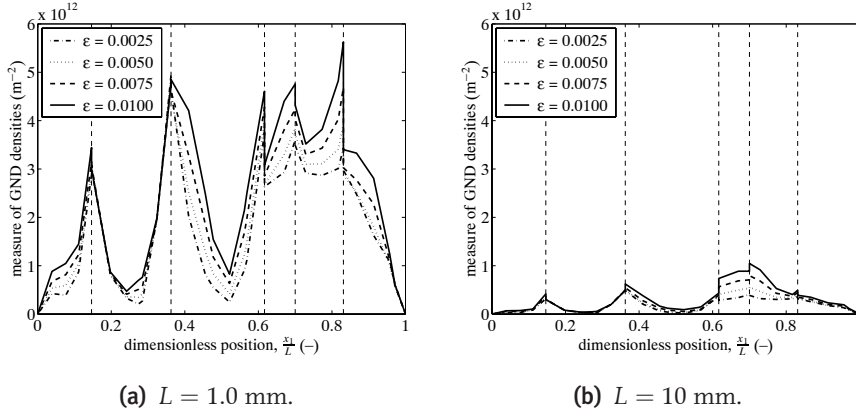


**Figure 4.7** / Profile of the measure for the GND densities along the dimensionless  $x_1$ -direction for increasing deformation  $\varepsilon$ , evaluated at half the sample height; the vertical dashed lines indicate the  $x_1$ -positions of the grain boundary intersections.

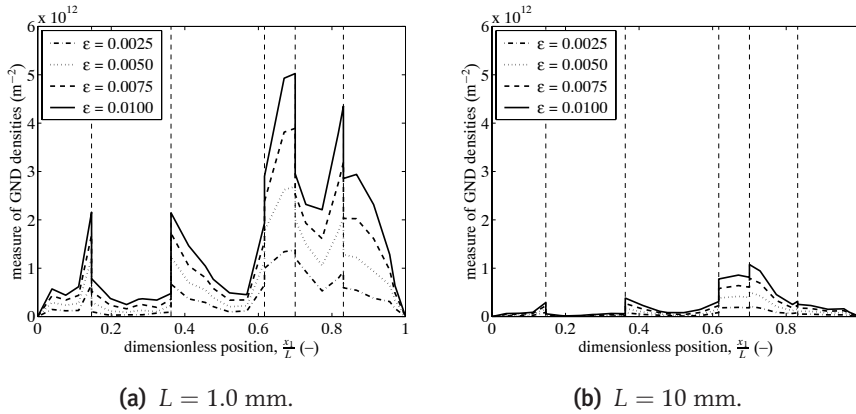


**Figure 4.8** / Profile of the measure for the GND densities along the dimensionless  $x_1$ -direction for increasing deformation  $\varepsilon$ , evaluated at half the sample height; in contrast to Figs. 4.4, 4.5, 4.6 and 4.7, here, the GBD densities have been omitted; the vertical dashed lines indicate the  $x_1$ -positions of the grain boundary intersections.

while  $\sigma_0$  is the flow stress in the absence of any size effects, i.e. corresponding to the imaginary situation of an infinitely large sample (in this case realized by enforcing all nodal GND densities to equal zero). Furthermore,  $k$  and  $n$  are the Hall-Petch slope and exponent, respectively.

The response results are presented in Figs. 4.9a and 4.9b, for both the cases with and without an initial GND density field, respectively. An obvious size effect can be distinguished, not only during plastic deformation, but moreover also at the onset of yielding.

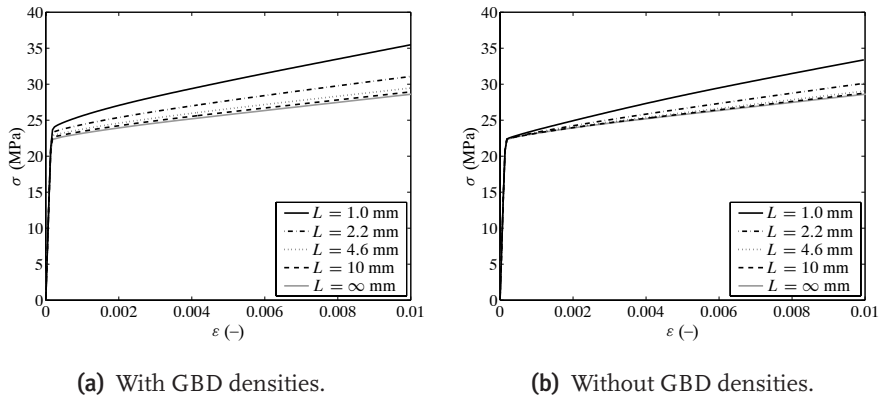


**Figure 4.9** / Stress-strain curves for various sample lengths  $L$ ; Hall-Petch exponent  $n = 1.50$ .

This latter effect is clearly the result of the presence of the GBD densities and is often observed in reality (e.g. Carreker and Hibbard, 1953). In order to quantify this grain size effect, the Hall-Petch relation in Eq. (4.47) is considered. However, it is noted that the particular polycrystal specimen in Fig. 4.2 deals with a much higher free surface fraction (with respect to the amount of grain boundaries) than the bulk polycrystals for which the Hall-Petch relation is actually intended. Besides, due to the limited number of grains, the specific crystallographic orientations may influence the results.

In order to find the Hall-Petch parameters, i.e. the Hall-Petch slope  $k$  and the exponent  $n$ , the value of  $\sigma_0(\varepsilon)$  is taken according to the stress-strain profile as simulated for the sample of (imaginary) infinitely large dimensions. Next, the parameters are determined in such a way that the total accumulated difference between the simulated stress-strain curves and the curves following from the Hall-Petch relation is minimized in a least squares sense, following Evers et al. (2002). For this procedure, it is assumed that  $n$  is a constant and that  $k$  may vary as a function of the equivalent logarithmic strain  $\varepsilon$ . The best fit of the Hall-Petch relation on *both* the data of Figs. 4.9a and 4.9b is achieved using a Hall-Petch exponent of  $n = 1.50$ . Both figures reveal the same Hall-Petch exponent because of the fact that the influence of the GBD density field is merely a superposition, which does not significantly disturb the dislocation density evolutions as such. The value for  $n$  achieved is larger than the values mostly reported in the literature, i.e.  $0.3 \leq n \leq 1.0$ , but it is remarked again, this might be caused by the enlarged free surface effect. In order to circumvent this effect, additional simulations have been performed, which consider the free surfaces to be artificial grain boundaries, i.e. by obstructing the crystallographic slip contribution in their outward normal direction. The resulting stress-strain response is presented in Fig. 4.10 and results in a Hall-Petch exponent of  $n = 1.19$ .

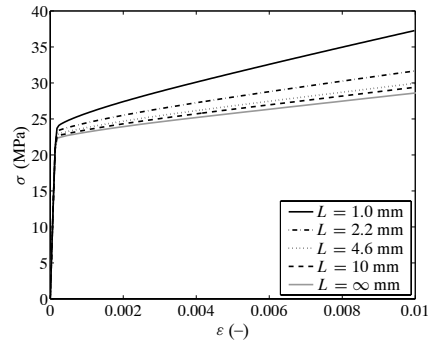


**Figure 4.10** / Stress-strain curves for various sample lengths  $L$ , taking into account GBD densities and obstructing plastic deformation near the outer surfaces; Hall-Petch exponent  $n = 1.19$ .

## 4.5 Conclusions

A non-local crystal plasticity framework has been developed, which incorporates the distinct interactions of various types of dislocation densities. This has been accomplished by including a phenomenological flow rule at the slip system level, which depends on an effective resolved shear stress and a slip resistance term. The first one is composed of the ordinary Schmid stress, yet in this case “corrected” by a newly developed back-stress measure, which represents the long-range interactions that are characteristic of GND density fields, because of their specific dislocation sign and relatively large range of influence. Moreover, it brings about a kinematic hardening contribution and includes dependences between various slip systems based on their spatial orientation. The second term –the slip resistance– depends on the short-range interactions between all dislocations present in the material (and therefore capable of obstructing the ongoing plastic deformation). This term comprises various interactions between SSD’s and GND’s on different slip systems, i.e. based on their spatial orientation. Whereas the SSD densities are controlled by a “generation-annihilation” evolution equation adopted from literature, the GND densities follow directly from the spatial gradients of crystallographic slip. Finally, a simplified formulation has been presented for the determination of grain boundary dislocation densities, based on the crystallographic lattice mismatch at the grain boundaries. These densities are used as a qualitative measure for an initial GND density field.

The implementation of the entire framework in a finite element environment incorporates the consideration of two governing equations, i.e. the ordinary stress equilibrium condition and the GND–plastic slip coupling. Next to formulating their variational expression, linearising them and discretising the governing quantities within a finite element context, the solution procedure for solving the strongly non-linear set of equations at the integration point level has been presented, along with a pragmatic approach for determining the consistent tangential relations which are necessary to solve the global system of equations iteratively. The extra nodal degrees of freedom –the GND densities– allow for the specification of various additional boundary conditions which closely approach reality, i.e. dislocation free outer surfaces, strongly obstructed plastic deformation between grains, and an initial GND density field near the grain boundaries.

The mechanical response of a polycrystal sample under plane stress conditions has been simulated for various sample sizes, where the grain configuration and crystallographic orientations remain unaltered. The SSD density field appears to be nearly size independent, where the largest SSD densities are found in the crystal core, related to the unhindered crystallographic slip in that region. Furthermore, the GND field is strongly size dependent, as the plastic inhomogeneities between the grain boundaries and the cores have to be accommodated by the GND field within a varying distance for the different sample sizes. This strengthening effect manifests itself in a size dependent flow stress, in addition to which the initial GND density field causes the (initial) yield stress to be size dependent.



## CHAPTER FIVE

# Discussion and conclusions

---

**Abstract** / First, the originally formulated hypothesis is repeated, reconsidered and complemented. Next, the single crystal based polycrystal sample simulations of Chapter 4 are used to verify an assumption that was made in Chapter 2, after which the applicability of both the polycrystal and the single crystal model is evaluated.

In the introduction of this thesis, it was contended that

*Predicting the scale dependent behaviour in a physically realistic manner can be accomplished by taking into account the GND densities and their constitutive influence in the crystal plasticity framework, along with the introduction of several appropriate physical length scales.*

With respect to this hypothesis, after consideration of both the developed polycrystal and single crystal model, it is clear that one of the physical length scales mentioned must be strongly related to the grain or specimen size. However, the size effects connected to those length scales are only sufficiently triggered if a representative (grain) boundary influence is included in some way. In Chapter 2 this is accomplished by considering bicrystals with internal macroscopical constraints and in the Chapters 3 and 4 by imposing micromechanically constrained boundary conditions at the grain boundaries. Once these constraints cause sufficient deformation heterogeneity within the grain or the specimen, according to the hypothesis, the GND densities are adopted as a physically-interpretable intermediate to couple these deformation gradients to differences in the mechanical response. On one hand, the actual determination of the GND densities inherently introduces a second physical length scale, i.e. the Burger's vector. If, on the other hand, the GND influence on the material strengthening involves –next to short range interactions– also long range influences (as is the case for the single crystal model), a third length scale reveals, equal to the radius of the GND evaluation area.



Considered more thoroughly, the polycrystal model requires the quantification of the width of the intercrystal dislocation dominated transition zone, represented by the length parameter  $l$  in Eq. (2.34). For that purpose, it was assumed in Eq. (2.35) that all grains, irrespective of their size, have a certain volume fraction to be attributed to their core, whereas the remaining volume fraction is assigned to the bi-crystal boundaries. Now, consider again the GND density distribution along the cross section of the polycrystal sample in Chapter 4. When focusing on the qualitative instead of the quantitative differences in Figs. 5.1a and 5.1b, by adapting the scales of Fig. 5.1b, it can be concluded that the assumption proposed in Chapter 2 is plausible. That is to say, the absolute “boundary layer” size in the grains of the large specimen is substantially larger, and relatively considered, the boundary layer sizes in both specimens are quite equal.

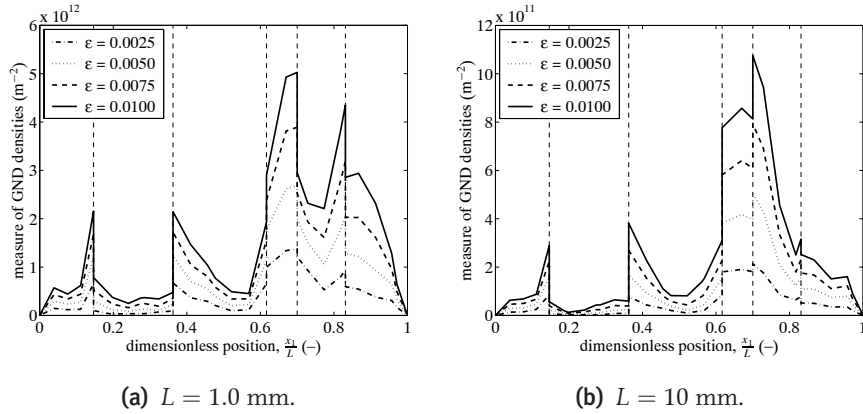


**Figure 5.1** / Profile of the measure for the GND densities along the dimensionless  $x_1$ -direction for increasing deformation  $\varepsilon$ , evaluated at half the sample height; no presence of GBD densities; the vertical dashed lines indicate the  $x_1$ -positions of the grain boundary intersections.

Alltogether, it has been shown that both models are capable of predicting a proper size dependent constitutive behaviour, where the polycrystal approach has been applied to accurately predict experimentally determined tensile curves for several average grain sizes. Also, the simulations of the constrained single crystal strip show good qualitative agreements when compared to results found in literature. Moreover, the experimentally found dependence of the (initial) yield stress on the grain size can also be predicted using the single crystal approach in combination with a decent field of grain boundary dislocation densities.

## Overview single crystal model

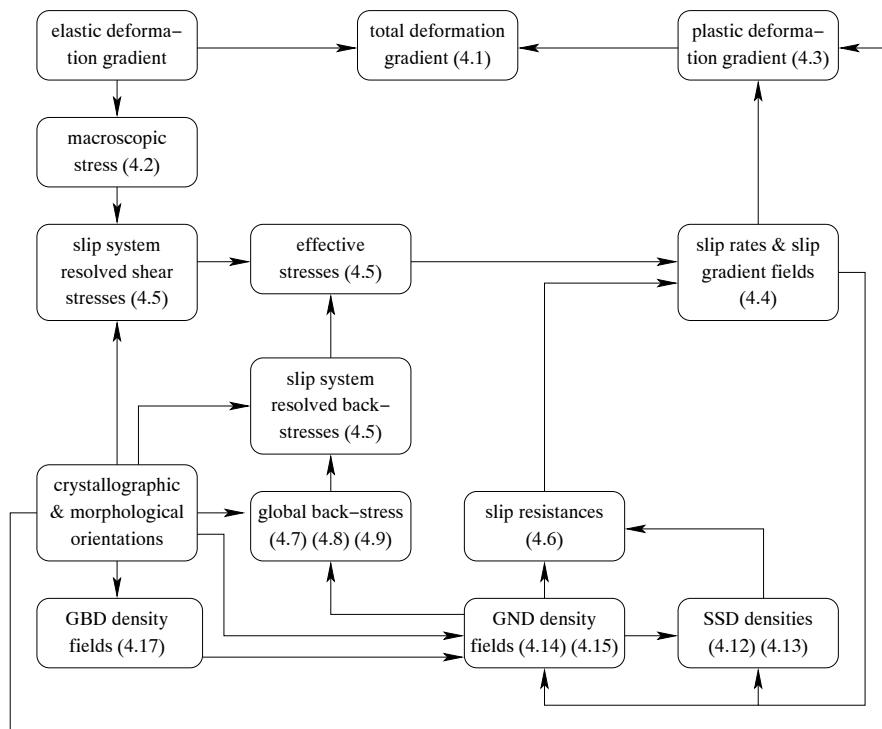


**Figure A.1** / Flow chart of the entire dislocation density based crystal plasticity framework as presented in Chapter 4 (and partially in Chapter 3); the accompanying equation numbers are also included.



## Bibliography

---

- ACHARYA, A. (2001). A model of crystal plasticity based on the theory of continuously distributed dislocations. *Journal of the Mechanics and Physics of Solids*, **49**, 761–784.
- ACHARYA, A. and BEAUDOIN, A. J. (2000). Grain-size effect in viscoplastic polycrystals at moderate strains. *Journal of the Mechanics and Physics of Solids*, **48**, 2213–2230.
- AHZI, S., PARKS, D. M., and ARGON, A. S. (1990). Modeling of plastic deformation evolution of anisotropy in semi-crystalline polymers. In B. SINGH (ed.), *Computer Modeling and Simulation of Manufacturing Processes*, ASME, MD-20, 287–292.
- AIFANTIS, E. C. (1987). The physics of plastic deformation. *International Journal of Plasticity*, **3**, 211–247.
- ARMSTRONG, R., CODD, I, DOUTHWAITE, R. M., and PETCH, N. J. (1962). The plastic deformation of polycrystalline aggregates. *The Philosophical Magazine*, **8**, 45–58.
- ARSENIS, A. and PARKS, D. M. (1999). Crystallographic aspects of geometrically-necessary and statistically stored dislocation density. *Acta Materialia*, **47**, 1597–1611.
- ARSENIS, A. and PARKS, D. M. (2000). Application of a three-dimensional model for plastic strain gradient crystal plasticity to grain-size dependent mechanical behavior of polycrystals. Private communication.
- ARSENIS, A. and PARKS, D. M. (2002). Modeling the evolution of crystallographic dislocation density in crystal plasticity. *Journal of the Mechanics and Physics of Solids*, **50**, 1979–2009.
- ASARO, R. J. (1983). Micromechanics of crystals and polycrystals. In J. W. HUTCHINSON and T. Y. WU (eds.), *Advances in Applied Mechanics*, 1–155.
- ASARO, R. J. and NEEDLEMAN, A. (1985). Texture development and strain hardening in rate dependent polycrystals. *Acta Metallurgica*, **33**, 923–953.
- ASARO, R. J. and RICE, J. R. (1977). Strain localization in ductile single crystals. *Journal of the Mechanics and Physics of Solids*, **25**, 309–338.
- ASHBY, M. F. (1970). The deformation of plastically non-homogeneous materials. *Philosophical Magazine*, **21**, 399–424.
- ASHMAWI, W. M. and ZIKRY, M. A. (2000). Effects of grain boundaries and dislocation density evolution on large strain deformation modes in fcc crystalline materials. *Journal of Computer-Aided Materials Design*, **7**, 55–62.
- BASSANI, J. L. (2001). Incompatibility and a simple gradient theory of plasticity. *Journal of the Mechanics and Physics of Solids*, **49**, 1983–1996.
- BASSANI, J. L., NEEDLEMAN, A., and VAN DER GIESSEN, E. (2001). Plastic flow in a composite: a comparison of nonlocal continuum and discrete dislocation predictions. *International Journal of Solids and Structures*, **38**, 833–853.
- BECKER, R. and PANCHANADEESWARAN, S. (1995). Effects of grain interactions of deformation and local texture. *Acta Metallurgica et Materialia*, **43**, 2107–2119.

- BITTENCOURT, E., NEEDLEMAN, A., GURTIN, M. E., and VAN DER GIESSEN, E. (2003). A comparison of nonlocal continuum and discrete dislocation plasticity predictions. *Journal of the Mechanics and Physics of Solids*, **51**, 281–310.
- BOAS, W. (1950). On the inhomogeneity of plastic deformation in metals. *Helvetica Physica Acta*, **23**, 159–166.
- BRONKHORST, C. A., KALIDINDI, S. R., and ANAND, L. (1992). Polycrystalline plasticity and the evolution of crystallographic texture in FCC metals. *Philosophical Transactions of the Royal Society of London A*, **341**, 443–477.
- BROWN, S. B., KIM, K. H., and ANAND, L. (1989). An internal variable constitutive model for hot working of metals. *International Journal of Plasticity*, **5**, 95–130.
- CARREKER, R. P. and HIBBARD, W. R. (1953). Tensile deformation of high-purity copper as a function of temperature, strain rate, and grain size. *Acta Metallurgica*, **1**, 654–663.
- CERMELLI, P. and GURTIN, M. E. (2002). Geometrically necessary dislocations in viscoplastic single crystals and bicrystals undergoing small deformations. *International Journal of Solids and Structures*, **39**, 6281–6309.
- CONRAD, H. (1963). Effect of grain size on the lower yield and flow stress of iron and steel. *Acta Metallurgica*, **11**, 75–77.
- COTTRELL, A. H. (1958). Theory of brittle fracture in steel and similar materials. *Transactions of the American Institute of Mining Engineers*, **212**, 192–203.
- COTTRELL, A. H. (1961). *Dislocations and plastic flow in crystals*. Oxford University Press, London.
- CUITIÑO, A. M. and ORTIZ, M. (1992). Computational modelling of single crystals. *Modelling and simulation in materials science and engineering*, **1**, 225–263.
- DAI, H. (1997). *Geometrically-necessary dislocation density in continuum plasticity theory, FEM implementation and applications*. Ph.D. thesis, Massachusetts Institute of Technology, Department of Mechanical Engineering.
- DAI, H. and PARKS, D. M. (1997). Geometrically-necessary dislocation density and scale-dependent crystal plasticity. In A. S. KHAN (ed.), *Proceedings of Plasticity '97: The Fifth International Symposium on Plasticity and its Current Applications*, 17–18, Juneau, Alaska. Neat Press.
- DELANNAY, L., HOUTTE, P. VAN, and SAMAJDAR, I. (1999). Modelling of the microscopic strain heterogeneity during cold rolling of steel sheets. Prediction of the deformation texture. *Journal de Physique IV*, **9**, 43–52.
- VAN DOMMELEN, J. A. W., PARKS, D. M., BOYCE, M. C., BREKELMANS, W. A. M., and BAAIJENS, F. P. T. (2003). Micromechanical modeling of the elasto-viscoplastic behavior of semi-crystalline polymers. *Journal of the Mechanics and Physics of Solids*, **51**, 519–541.
- ESSMANN, U. and MUGHRABI, H. (1979). Annihilation of dislocations during tensile and cyclic deformation and limits of dislocation densities. *Philosophical Magazine A*, **40**, 731–756.
- EVERS, L. P., PARKS, D. M., BREKELMANS, W. A. M., and BAAIJENS, F. P. T. (2000). Intermediate modeling of the elasto-viscoplastic behavior of polycrystal FCC metals. In E. OÑATE, G. BUGEDA, and B. SUÁREZ (eds.), *Proceedings of the European Congress on Computational Methods in Applied Sciences and Engineering*, on CD-ROM, Barcelona, Spain.
- EVERS, L. P., PARKS, D. M., BREKELMANS, W. A. M., and GEERS, M. G. D. (2001). Enhanced modeling of hardening in crystal plasticity for FCC metals. *Journal de Physique IV*, **11**, 179–186.
- EVERS, L. P., PARKS, D. M., BREKELMANS, W. A. M., and GEERS, M. G. D. (2002). Crystal plasticity model with enhanced hardening by geometrically necessary dislocation accumulation. *Journal of the Mechanics and Physics of Solids*, **50**, 2403–2424.
- EVERS, L. P., BREKELMANS, W. A. M., and GEERS, M. G. D. (2003a). Non-local crystal plasticity model with intrinsic SSD and GND effects. *Journal of the Mechanics and Physics of Solids*, (submitted).
- EVERS, L. P., BREKELMANS, W. A. M., and GEERS, M. G. D. (2003b). Scale dependent crystal plasticity framework with dislocation density and grain boundary effects. *International Journal of Solids and Structures*, (submitted).

- FLECK, N. A. and HUTCHINSON, J. W. (1997). Strain gradient plasticity. *Advances in Applied Mechanics*, **33**, 295–361.
- FLECK, N. A., MULLER, G. M., ASHBY, M. F., and HUTCHINSON, J. W. (1994). Strain gradient plasticity: theory and experiment. *Acta metallurgica et Materialia*, **42**, 475–487.
- FRANCIOSI, P. and ZAOU, A. (1982). Multislip in F.C.C. crystals; a theoretical approach compared with experimental data. *Acta Metallurgica*, **30**, 1627–1637.
- FU, H.-H., BENSON, D. J., and MEYERS, M. A. (2001). Analytical and computational description of effect of grain size on yield stress of metals. *Acta Materialia*, **49**, 2567–2582.
- GAO, H. and HUANG, Y. (2003). Geometrically necessary dislocation and size-dependent plasticity. *Scripta Materialia*, **48**, 113–118.
- GAO, H., HUANG, Y., NIX, W. D., and HUTCHINSON, J. W. (1999). Mechanism-based strain gradient plasticity—I. Theory. *Journal of the Mechanics and Physics of Solids*, **47**, 1239–1263.
- GAVRILJUK, V. G., BERNS, H., ESCHER, C., GLAVATSKAYA, N. I., SOZINOV, A., and PETROV, Y. N. (1999). Grain boundary strengthening in austenitic nitrogen steels. *Materials Science and Engineering*, **A271**, 14–21.
- VAN DER GIESSEN, E. and NEEDLEMAN, A. (2003). GNDs in nonlocal plasticity theories: lessons from discrete dislocation simulations. *Scripta Materialia*, **48**, 127–132.
- GRAY III, G. T., CHEN, S. R., and VECCHIO, K. S. (1999). Influence of grain size on the constitutive response and substructure evolution of MONEL 400. *Metallurgical and Materials Transactions A*, **30**, 1235–1247.
- GROMA, I. (1997). Link between the microscopic and mesoscopic length-scale description of the collective behavior of dislocations. *Physical Review B*, **56**, 5807–5813.
- GURTIN, M. E. (2002). A gradient theory of single-crystal viscoplasticity that accounts for geometrically necessary dislocations. *Journal of the Mechanics and Physics of Solids*, **50**, 5–32.
- HALL, E. O. (1951). The deformation and aging of mild steel: iii. discussion of results. *Proceedings of the Physical Society of London*, **B64**, 747–753.
- HANSEN, N. (1979). The effect of grain size and strain on the tensile flow stress of copper at room temperature. In P. HAASEN, V. GEROLD, and G. KOSTORZ (eds.), *Proceedings of the 5th International Conference on the Strength of Metals and Alloys*, **2**, 849–854, Oxford. Pergamon Press.
- HANSEN, N. (1982). Flow stress and grain size dependence of non-ferrous metals and alloys. In T. N. BAKER (ed.), *Yield, flow and fracture of polycrystals*, **XI**, 311–350, London. Applied Science Publishers.
- HARDER, J. (1999). A crystallographic model for the study of local deformation processes in polycrystals. *International Journal of Plasticity*, **15**, 605–624.
- HILL, R. and RICE, J. R. (1972). Constitutive analysis of elastic-plastic crystals at arbitrary strain. *Journal of the Mechanics and Physics of Solids*, **20**, 401–413.
- HIRTH, J. P. (1972). The influence of grain boundaries on mechanical properties. *Metallurgical Transactions*, **3**, 3047–3067.
- HUANG, Y., GAO, H., NIX, W. D., and HUTCHINSON, J. W. (2000). Mechanism-based strain gradient plasticity—II. Analysis. *Journal of the Mechanics and Physics of Solids*, **48**, 99–128.
- HUTCHINSON, J. W. (1976). Bounds and self-consistent estimates for creep of polycrystalline materials. *Proceedings of the Royal Society of London A*, **348**, 101–127.
- KALIDINDI, S. R., BRONKHORST, C. A., and ANAND, L. (1992). Crystallographic texture evolution in bulk deformation processing of fcc metals. *Journal of the Mechanics and Physics of Solids*, **40**, 537–569.
- KAZMI, B. and MURR, L. E. (1979). Anomalous residual shock hardening in nickel and stainless steel at a short pulse duration. *Scripta Metallurgica*, **13**, 993–997.
- KOCHENDORFER, A. (1941). *Plastische Eigenschaften von Kristallen und Metallischen Werkstoffen*. Springer Verlag, Berlin.
- KOCKS, U. F. (1970). The relation between polycrystal deformation and single crystal deformation. *Metallurgical Transactions*, **1**, 1121–1144.

- KOCKS, U. F. (2001). Realistic constitutive relations for metal plasticity. *Materials Science and Engineering*, **A317**, 181–187.
- KOCKS, U. F., ARGON, A. S., and ASHBY, M. F. (1975). Thermodynamics and kinetics of slip. In B. CHALMERS, J. W. CHRISTIAN, and T. B. MASSALSKI (eds.), *Progress in Materials Science*, **19**, 1–289, Oxford. Pergamon Press Ltd.
- KRÖNER, E. (1962). Dislocations and continuum mechanics. *Applied Mechanics Review*, **15**, 599–606.
- KUBIN, L. P., CANOVA, G., CONDAT, M., DEVINCRE, B., PONTIKIS, V., and BRECHET, Y. (1992). Dislocation microstructures and plastic flow: a 3D simulation. *Solid State Phenomena*, **23&24**, 455–472.
- LAVRENTEV, F. F. (1980). The type of dislocation interaction as the factor determining work hardening. *Materials Science and Engineering*, **46**, 191–208.
- LEE, B. J., AHZI, S., and PARKS, D. M. (1999). Intermediate modeling of polycrystal plasticity. In A. S. KHAN (ed.), *Proceedings of plasticity '99: The Seventh International Symposium on Plasticity and its Current Applications*, 377–380, Cancun, Mexico. Neat Press.
- LEE, E. H. (1969). Elastic-plastic deformation at finite strains. *Journal of Applied Mechanics*, **36**, 1–6.
- LI, J. C. M. and CHOU, Y. T. (1970). The role of dislocations in the flow stress-grain size relationships. *Metallurgical Transactions*, **1**, 1145–1159.
- MANDEL, J. (1974). Thermodynamics and plasticity. In J. J. DELGADO DOMINGOS, M. N. R. NINA, and J. H. WHITELOW (eds.), *Proceedings of the International Symposium on Foundations of Continuum Thermodynamics*, 283–311, Bussaco, Portugal.
- MEYERS, M. A. and ASHWORTH, E. (1982). A model for the effect of grain size on the yield stress of metals. *Philosophical Magazine*, **46**, 737–759.
- MOLINARI, A., AHZI, S., and KOUDANE, R. (1997). On the self-consistent modeling of elastic-plastic behavior of polycrystals. *Mechanics of Materials*, **26**, 43–62.
- MUGHRABI, H. (2001). On the role of strain gradients and long-range internal stresses in the composite model of crystal plasticity. *Materials Science and Engineering*, **A317**, 171–180.
- MURA, T. (1987). *Micromechanics of defects in solids*. Kluwer Academic Publishers, Boston.
- NABARRO, F. R. N. (1950). Influence of grain boundaries on the plastic properties of metals. In V. G. W. HARRISON (ed.), *Some Recent Developments in Rheology*, 38–52, London. United Trade Press.
- NAKANISHI, K. and SUZUKI, H. (1974). Analysis of the grain size dependence of the yield stress in Cu-Al and Cu-Ni alloys. *Transactions of the Japan Institute of Metals*, **15**, 435–440.
- NARUTANI, T. and TAKAMURA, J. (1991). Grain-size strengthening in terms of dislocation density measured by resistivity. *Acta Metallurgica et Materialia*, **39**, 2037–2049.
- NEEDLEMAN, A. and GIL SEVILLANO, J. (2003). Preface to the viewpoint set on: geometrically necessary dislocations and size dependent plasticity. *Scripta Materialia*, **48**, 109–111.
- NEMAT-NASSER, S., LUQUN, N., and OKINAKA, T. (1998). A constitutive model for fcc crystals with application to polycrystalline OFHC copper. *Mechanics of Materials*, **30**, 325–341.
- NIX, W. D. and GAO, H. (1998). Indentation size effects in crystalline materials: A law for strain gradient plasticity. *Journal of the Mechanics and Physics of Solids*, **46**, 411–425.
- NYE, J. F. (1953). Some geometrical relations in dislocated crystals. *Acta Metallurgica*, **1**, 153–162.
- OROWAN, E. (1934). Zur Kristallplastizität III: Über die Mechanismus des Gleitvorganges. *Zeitschrift für Physik*, **89**, 634–659.
- PEIRCE, D., ASARO, R. J., and NEEDLEMAN, A. (1982). An analysis of non-uniform and localized deformation in ductile single crystals. *Acta Metallurgica*, **30**, 1087–1119.
- PETCH, N. J. (1953). The cleavage strength of polycrystals. *Journal of the Iron and Steel Institute*, **174**, 25–28.
- RICE, J. R. (1971). Inelastic constitutive relations for solids: an internal variable theory and its application to metal plasticity. *Journal of the Mechanics and Physics of Solids*, **19**, 433–455.
- SABAR, H., BERVEILLER, M., FAVIER, V., and BERBENNI, S. (2002). A new class of micro-macro models for elastic-viscoplastic heterogeneous materials. *International Journal of Solids and Structures*, **39**, 3257–3276.

- SHI, M. X., HUANG, Y., and HWANG, K. C. (2000). Plastic flow localization in mechanism-based strain gradient plasticity. *International Journal of Mechanical Sciences*, **42**, 2115–2131.
- SHU, J. Y. and FLECK, N. A. (1999). Strain gradient crystal plasticity: size-dependent deformation of bicrystals. *Journal of the Mechanics and Physics of Solids*, **47**, 297–324.
- SHU, J. Y., FLECK, N. A., VAN DER GIESSEN, E., and NEEDLEMAN, A. (2001). Boundary layers in constrained plastic flow: comparison of nonlocal and discrete dislocation plasticity. *Journal of the Mechanics and Physics of Solids*, **49**, 1361–1395.
- SLUYS, L. J. and ESTRIN, Y. (2000). The analysis of shear banding with a dislocation based gradient plasticity model. *International Journal of Solids and Structures*, **37**, 7127–7142.
- STEINMANN, P. (1996). Views on multiplicative elastoplasticity and the continuum theory of dislocations. *International Journal of Engineering Science*, **34**, 1717–1735.
- STÖLKEN, J. S. and EVANS, A. G. (1998). A microbend test method for measuring the plasticity length scale. *Acta Metallurgica et Materialia*, **46**, 5109–5115.
- SUN, S., ADAMS, B. L., and KING, W. (2000). Observations of lattice curvature near the interface of a deformed aluminium bicrystal. *Philosophical Magazine A*, **80**, 9–25.
- SUZUKI, H. and NAKANISHI, K. (1975). A theory of the grain size dependence of the yield stress in face-centered cubic alloys. *Transactions of the Japan Institute of Metals*, **16**, 17–27.
- SVENDSEN, B. (2003). Continuum thermodynamic modeling and simulation of additional hardening due to deformation incompatibility. In C. MIEHE (ed.), *Solid Mechanics and its Applications*, **108**, 496, Dordrecht. Kluwer Academic Publishers.
- TABOUROT, L., FIVEL, M., and RAUCH, E. (1997). Generalised constitutive laws for f.c.c. single crystals. *Materials Science and Engineering*, **A234–236**, 639–642.
- TAYLOR, G. I. (1938). Plastic strain in metals. *The Journal of the Institute of Metals*, **62**, 307–324.
- THOMPSON, A. W., BASKES, M. I., and FLANAGAN, W. F. (1973). The dependence of polycrystal work hardening on grain size. *Acta Metallurgica*, **21**, 1017–1032.
- WORTHINGTON, P. J. and SMITH, E. (1964). The formation of slip bands in polycrystalline 3% silicon iron in the pre-yield microstrain region. *Acta Metallurgica*, **12**, 1277–1281.
- ZIKRY, M. A. and KAMEDA, T. (1998). Inelastic three dimensional high strain-rate dislocation density based analysis of grain-boundary effects and failure modes in ordered intermetallics. *Mechanics of Materials*, **28**, 93–102.





## Samenvatting

---

De identificatie van het mechanisch gedrag van metalen is doorgaans gebaseerd op vooronderstelde homogene deformatie- en spanningsvelden, terwijl eventueel beschikbare informatie met betrekking tot de feitelijke heterogene deformatie op de schaal van de microstructuur nauwelijks gebruikt wordt. Dit legt strenge beperkingen op aan de mogelijkheden om het constitutief gedrag te voorspellen in gevallen waarbij de productafmetingen van dezelfde orde van grootte zijn als de lengteschaal van de microstructuur, dat wil zeggen de grootte van de korrels. Daarmee samenhangend kunnen schaalafhankelijke verschijnselen, zoals het effect van de korrelgrootte, of het materiaalgedrag onder invloed van een opgelegde heterogene belasting op globaal niveau, enkel begrepen, gemodelleerd en voorspeld worden als de microstructuur beschouwd wordt, terwijl het gedrag inherent rekgradiënt-afhankelijk wordt. Het doel van dit onderzoek is daarom het ontwikkelen van een kristalplasticiteitsformulering die deze eigenschappen in rekening brengt. Hierbij is de koppeling van de microstructuur en de rekgradiënten aan het mechanisch gedrag het gevolg van geometrisch-noodzakelijke dislocaties (GND's), die ontstaan als gevolg van microstructurele heterogeniteiten en die korte- en lange-afstandseffecten veroorzaken op het constitutief gedrag.

Op de polykristallijne schaal is een kristalplasticiteitsmodel ontwikkeld, dat elke korrel beschouwt als een kern bestaande uit een éénkristal, omgeven door een verzameling van bikristallen die de korrelgrenzen symboliseren. Hierbij zijn de roosteroriëntaties van de naburige kristallen in de buitenste gedeeltes van de bikristallen ondergebracht. De overgang van het gedrag van alle individuele kristallen (zoals beschouwd in het betreffende materiële punt) op de microschaal naar een macroscopische responsie wordt bewerkstelligd door een gemodificeerde Taylor middelingsprocedure. Bij het afdwingen van deformatiecompatibiliteit en spanningsevenwicht op de grensvlakken in de bikristallen, wordt de deformatie binnen de korrel heterogeen (de kern en de binnenste gedeeltes van de bikristallen zullen verschillend deformeren), in een mate die bepaald wordt door de grootte van de korrel. Deze heterogeniteit geeft aanleiding tot het ontstaan van GND's om de compatibiliteit van het kristalrooster te waarborgen. Deze GND's fungeren als hindernissen voor de beweging van de glijdende dislocaties die behoren bij de plas-

tische deformatie, ook wel statistisch-opgeslagen dislocaties (SSD's) genoemd. Dit extra versterkingseffect wordt in rekening gebracht door een toenemende slipweerstand. Het verkleinen van de kristal grootte leidt dienovereenkomstig tot een verhoging van de vloeispanning, een verschijnsel dat ook experimenteel wordt geconstateerd en dat bekend staat als het Hall-Petch effect. Eénassige simulaties op een verzameling kristallen met een instelbare kristal grootte resulteren in de numerieke voorspelling van gemeten kristal grootte-afhankelijke trek-rek-krommes.

Met betrekking tot het hierboven beschreven model zijn er enkele beperkingen geïntroduceerd, waarvan sommige ondervangen kunnen worden op de polykristallijne schaal, maar andere de beschouwing van heterogeniteiten binnen de korrels op een enkelvoudig kristal niveau behoeven. Binnen een eindige-elementenmethode-uitwerking betekent dit, dat elke korrel in voldoende eindige elementen wordt onderverdeeld en waarbij aan een aantal aspecten ruimere aandacht wordt gegeven. Allereerst waren in de polykristallijne aanpak de GND-dichtheden uitsluitend op een indirecte manier aan de heterogeniteiten in de deformatie gekoppeld, terwijl in de enkelvoudige kristalaanpak een directe geometrische relatie tussen verschillende kristallografische slipgradiënten en de daarmee samenhangende rand- en schroef- GND-dichtheden wordt gelegd. Daar de bepaling van alle (rand-) SSD-dichtheden expliciet volgt uit een geschikte evolutievergelijking, hoeft de niet-eenduidige keuze met betrekking tot het samenvoegen van de SSD- en GND-sterktes of hun effectieve dichtheden niet meer gemaakt te worden. Bovendien beïnvloeden de GND's niet alleen het mechanisch gedrag op een korte-afstandsmanier, dat wil zeggen via de locale slipweerstand, maar worden ook de geometrische effecten van de GND's op een grotere lengteschaal geïncorporeerd, door hun dislocatieteken en de GND-dichtheidsgradiënten te verdisconteren. Deze lange-afstandsbeïnvloeding wordt gerealiseerd door het beschouwen van een GND-gerelateerde tegenwerkende spanningsbijdrage, tegenovergesteld aan de op een slipvlak werkende schuifspanning. Daarnaast kunnen er ter plaatse van de korrelgrenzen geschiktere micromechanische beperkingen worden afgedwongen dan voorheen konden worden voorgeschreven op de grensvlakken van de bikristallen, terwijl de bijkomende verwerking van korrelgrensdislocatie- (GBD-) dichtheden, welke de aanvankelijke roosteroriëntatieverschillen voor hun rekening nemen, zorgt voor een korrelgrootte-afhankelijk vloeipunt, beide in overeenstemming met experimentele observaties. Tot slot kan een tweede niet-eenduidige keuze, met betrekking tot de volumefractie van de bikristallen ten opzichte van de kernen, bij gebruik van deze enkelvoudige kristalaanpak worden omzeild. Deze laatstgenoemde aanpak geeft zelfs de mogelijkheid om in te schatten hoe die volumefractie geschikt gekozen zou kunnen worden.

Het ontwikkelde kristalplasticiteitsmodel is gebruikt om het afschuivingsgedrag van een denkbeeldig éénkristal met twee slipsystemen onder vlakke-rekcondities te simuleren. Daarbij wordt de kristallijne slip in de normaalrichting verhinderd bij de grensvlakken, waardoor een deformatieheterogeniteit wordt veroorzaakt die gerelateerd is aan de strip-

grootte. Dientengevolge wordt er een afmetingsafhankelijke vloeispanning geconstateerd die, net zoals de slip- en GND-dichtheidsprofielen over de stripdoorsnede, in kwalitatieve overeenstemming is met resultaten uit de literatuur. Het model is eveneens toegepast om het constitutieve gedrag van een polykristal (bestaande uit een beperkt aantal korrels), dat op trek wordt belast onder vlak-spanningscondities, te simuleren. Hierbij is tevens de proefstukgrootte gevarieerd, al met al resulterend in andere heterogeniteiten binnen de korrels. Naast de vloeispanning blijkt ook het initiële vloeipunt af te hangen van de kristalgrootte.



## Dankwoord / Acknowledgements

---

Graag wil ik iedereen bedanken die gedurende mijn promotiewerkzaamheden op directe of indirecte wijze heeft bijgedragen tot het uiteindelijke resultaat. Op de eerste plaats ben ik het Netherlands Institute for Metals Research erkentelijk voor de onmisbare steun aan dit onderzoek. Een bijzonder woord van dank gaat verder uit naar Marcel Brekelmans en Marc Geers, waarmee ik de nodige uurtjes rond de discussietafel heb gezeten, uurtjes die ik immer als plezierig heb ervaren. Hierbij is hun inspiratie en kritische instelling van grote waarde geweest voor de totstandkoming van het uiteindelijke model, alsmede de numerieke implementatie en de documentatie ervan. Daarnaast wil ik Frank Baaijens bedanken voor het initiëren van dit hele gebeuren en voor het bieden van de gelegenheid om een half jaar belangrijke ervaring op te doen aan het Massachusetts Institute of Technology (MIT).

During my research period at the MIT, David Parks has been so kind to guide me through the field of crystal plasticity and to initialise the model as presented in the second chapter of this thesis. His enthusiasm and support have always been a great motivation, for which I owe him many thanks.

Ook wil ik hierbij graag Ron Peerlings bedanken voor zijn steun door middel van zowel praktisch als inhoudelijk nuttige tips en discussies, en natuurlijk voor de licentie inzake het gebruik van zijn eindige elementen programma “Artemis”. Daarnaast hebben Leo Wouters en Patrick van Brakel mij voorzien van de nodige digitale ondersteuning, waarvoor dank.

Mijn collega's van het NIMR en de overige leden van de “Metals Forming”-groep wil ik bedanken voor de prettige samenwerking, maar ook voor de gezellige sfeer tijdens cursussen, congressen en andere trips. Met name mijn twee mede-musketiers en tevens kamergenoten, Hans van Dommelen en Roy Engelen, hebben de afgelopen vier jaar tot een hele belevenis gemaakt. Met Hans heb ik in Amerika alle extreme weersomstandigheden en menig andere gebeurtenis doorstaan, waarnaast hij mij eveneens van de nodige grafische en numerieke ondersteuning heeft voorzien. Met Roy als mijn carpoolchauffeur hebben we alle wegen in en rondom Eindhoven ontdekt in onze weerloze strijd

tegen de files. Naast hen wil ik ook Olaf van der Sluis bedanken. Onze –soms zinnige, maar meestal onzinnige– discussies waren altijd een leuke afwisseling. Ook mijn andere kamergenote, Ruchi Rastogi, wil ik op deze plaats bedanken.

Alle “inspanningen” buiten werktijd hebben de afgelopen jaren voor de nodige en zeer welkome ontspanning gezorgd, met alle plezier en gezelligheid van dien. Hiervoor wil ik mijn vrienden, oftewel de hele survival-groep, hartelijk bedanken. Tot slot wil ik een speciaal woord van dank aan mijn ouders en naaste (schoon)familie richten, voor alle vormen van steun, vertrouwen en interesse. Ik weet niet hoe ik al mijn dank aan Nicole het best kan omschrijven, haar steun, inbreng en opofferingen waren in ieder geval van onschatbare waarde voor mij...

Rens Evers,  
Eindhoven, augustus 2003.

## Curriculum Vitae

---

Rens Evers was born on November 5, 1976 in St. Odiliënberg, The Netherlands. In 1994, he finished his secondary education at the Bisschoppelijk College Schöndeln in Roermond. From 1994 until 1999 he studied Mechanical Engineering at the Eindhoven University of Technology. During his study, he did a traineeship at Philips CFT in Eindhoven, and became interested in the field of micromechanics of materials. He received his master's degree in 1999 on the subject of computational crystal plasticity for metals. In that year he started his Ph.D. research on strain gradient crystal plasticity, as a project of the Netherlands Institute for Metals Research (NIMR) program, in the Materials Technology group of the Eindhoven University of Technology. Part of this research was performed at the Department of Mechanical Engineering of the Massachusetts Institute of Technology (MIT) in Cambridge, USA.



